
UNIVERSIDADE FEDERAL DE PERNAMBUCO
DEPARTAMENTO DE FÍSICA – CCEN
PROGRAMA DE PÓS-GRADUAÇÃO EM FÍSICA

BRUNO NOGUEIRA DE SOUZA MEDEIROS

# COLLECTIVE PHENOMENA IN NETWORKS OF ELECTRONIC NEURONS

Recife
2015

**BRUNO NOGUEIRA DE SOUZA MEDEIROS**

# COLLECTIVE PHENOMENA IN NETWORKS OF ELECTRONIC NEURONS

Tese apresentada ao Programa de Pós-Graduação em Física da Universidade Federal de Pernambuco, como requisito parcial para a obtenção do título de Doutor em Física.

Orientador:
Prof. Dr. Mauro Copelli Lopes da Silva
Universidade Federal de Pernambuco

Recife
2015

Catalogação na fonte
Bibliotecária Joana D'Arc Leão Salvador CRB4-532

M488c Medeiros, Bruno Nogueira de Souza.
Collective phenomena in networks of electronic neurons / Bruno Nogueira de Souza Medeiros. – Recife: O Autor, 2015.
116 f.: fig; tab.

Orientador: Mauro Copelli.
Tese (Doutorado) – Universidade Federal de Pernambuco. CCEN. Física, 2015.
Inclui referências e apêndices.

1. Neurociências. 2. Circuitos eletrônicos. I. Copelli, Mauro (Orientador). II. Titulo.

003.85 CDD (22. ed.) UFPE-FQ 2015-08

BRUNO NOGUEIRA DE SOUZA MEDEIROS

**COLLECTIVE PHENOMENA IN NETWORKS OF ELECTRONIC NEURONS**

Tese apresentada ao Programa de Pós-Graduação em Física da Universidade Federal de Pernambuco, como requisito parcial para a obtenção do título de Doutor em Física.

Aprovada em: 26/02/2015.

**BANCA EXAMINADORA**

_____

Prof. Dr. Mauro Copelli Lopes da Silva
Orientador
Universidade Federal de Pernambuco

_____

Prof. Dr. José Roberto Rios Leite
Examinador Interno
Universidade Federal de Pernambuco

_____

Prof. Dr. Pedro Valadão Carelli
Examinador Interno
Universidade Federal de Pernambuco

_____

Prof. Dr. Antonio Carlos Roque da Silva Filho
Examinador Externo
Universidade de São Paulo

_____

Prof. Dr. Marcos César Santos Oriá
Examinador Externo
Universidade Federal da Paraíba

*To all those who believed.*

# Acknowledgements

The conclusion of this work was possible thanks to the providential help of many people. Among them are Professor José Rios Leite, whose continuous support during last years shed light on many problems we faced and Marcos Aurélio do Nascimento, whose technical support allowed us to move forward much faster then we would have by ourselves. Special thanks to my advisor Mauro Copelli for his dedication, support and patience.

Thanks to CNPq, FACEPE, Pronex and Pronem for the funding that allowed this research to happen.

Thanks to professors José Roberto Rios Leite, Pedro Valadão Carelli, Marcos César Santos Oriá and Antonio Carlos Roque da Siva for accepting the invitation to join the Thesis Defense Committee.

Thanks to my parents, Ladjane Nogueira Lins and Fernando Antônio de Souza Medeiros for the support since the very beginning. Thanks also to my sister, Fernanda Nogueira de Souza Medeiros and my niece Melissa Nogueira Torres Vieira for lightening up my days.

Thanks to my longtime friends, who were there for the good and not-so-good moments: Raony, Géssica, Ivannoska, Ney, João Marcílio (J), Victor (Redman), Diego (Klaus), Virgínia, Kirlian, Leticia, Christian (BurnedWater), Anderson (Brow), Hercílio (Spell), Fábio, Denise, Sérgio e Alan. Special thanks to Fernanda Selingardi Matias for continuous encouragement throughout my whole academic life.

Lastly, very special thanks to Andreza Ribeiro Tavares, who makes everything so much easier.

*Men of learning suspect it little, and ignore it mostly.*
—H.P. LOVECRAFT (Hypnos)

# Abstract

Biological sensory system are usually composed of complex networks of thousands of neurons capable of differentiating stimuli ranging many orders of magnitude, which translates to a large dynamic range. Recent works suggest that large dynamic ranges arise as a collective phenomenon of many excitable elements of low dynamic range connected together. This effect has possible practical applications in the construction of biologically inspired sensors with high sensibility and dynamic range. With such motivation, this thesis proposes the use of electronic circuits of extreme simplicity in the construction of excitable elements networks.

An excitable electronic circuit, inspired in the dynamics of the FitzHugh-Nagumo model for neuronal excitability, is the building block in the construction of networks. To connect such circuits, another electronic circuit mimicking the behavior of chemical synapses is employed. Due to their simplicity, both circuits allow for straightforward mathematical modeling and reproduction in large scale. Despite that, important dynamic parameters such as time scales and coupling strengths can be controlled.

The use of those electronic circuits, along with other complementary circuits like noise generators, allows for the investigation of many collective phenomena where excitable elements are the main agents. In this work we focus our efforts in the study of synaptic symmetry effects that lead to coherence or incoherence resonance and in the phenomenon of dynamic range increase.

**Keywords:** Electronic circuits. Excitable elements. Neurons. Synapses. Coherence resonance. Dynamic range.

# Resumo

Sistemas sensoriais biológicos usualmente são formados por redes complexas de milhares de neurônios capazes de discernir estímulos cujas intensidades podem cobrir várias ordens de magnitude, o que se traduz em uma grande faixa dinâmica. Estudos recentes sugerem que grandes faixas dinâmicas emergem como um fenômeno coletivo de vários elementos excitáveis de pequena faixa dinâmica conectados entre si. Este efeito tem possíveis aplicações práticas na construção de sensores biologicamente inspirados de alta sensibilidade e grande faixa dinâmica. Motivado por este fato, esta tese propõe o uso de circuitos eletrônicos de extrema simplicidade para a construção de redes de elementos excitáveis.

Um circuto eletrônico excitável, inspirado na dinâmica do modelo de FitzHugh-Nagumo para excitabilidade neuronal, serve como elemento básico na construção de redes. Para conectar tais circuitos, um outro circuito eletrônico que simula o comportamento de sinapses químicas é utilizado. Devido à sua simplicidade, ambos os circuitos permitem fácil modelagem matemática, além de poderem ser reproduzidos em larga escala. Ainda assim, os circuitos dão liberdade para controle de parâmetros importante da dinâmica, como escalas temporais e intensidades de acoplamento.

O uso destes circuitos eletrônicos, juntamente com circuitos complementares, como geradores de ruído, permitem a investigação diversos fenômenos coletivos envolvendo elementos excitáveis. Neste trabalho focamos nossos esforços no estudo de efeitos de simetria sináptica, que levem à ressonâcia de coerência ou incoerência e no fenômeno de alargamento de faixa dinâmica.

**Palavras-chave:** Circuitos eletrônicos. Elementos excitáveis. Neurônios. Sinapses. Ressonância de coerência. Faixa dinâmica.

# List of Figures

LIST OF FIGURES

# List of Tables

# Contents

CHAPTER 1

# Introduction

Neurons are known to produce many different complex behaviors despite their relatively simple individual working mechanisms. Such complexity arises from the collective interactions between neurons in networks of the nervous system. Nonetheless, individual neurons can also behave unexpectedly under specific conditions, e.g. under special types of stimulation, and although far from the behavioral complexity that can be presented by networks of tens of thousands of neurons, low dimensionality networks (even a pair of neurons) can provide response patterns that are much more interesting that those of a single neuron. In this thesis we aim to show the complexity presented by very small neuron networks, ranging from one to twenty neurons, focusing on two main non-trivial phenomena: Coherence resonance in noise driven neuron systems and the increase of dynamic range in neuron networks as a result of increased system connectivity.

For most of this work, the results are obtained experimentally by activity measurement on systems of electronic neurons that can be modeled by a set of differential equations. The model used is unique in the sense that it has a simple mathematical description that allows an easy numerical implementation for comparison purposes. It also requires few and very simple electronic components which allows for scalability, e.g. the electronic neurons can be largely reproduced, making each unit a building block for the creation of any type of neuron network.

The use of electronic neuronal models presents a few advantages over purely computational neuron models. First of all, an electronic system is an actual physical system "in the real world" instead of just a computer representation. The electronic neuron model allows for real time parameter scanning, for it is possible to observe the change in behavior on an oscilloscope as the parameters, such as the value of a resistance, are changed. Another advantage is the naturally noisy environment provided by the electronic components in the model, a characteristic expected from real biological systems. Finally, as electronic components of the same type are only equal within a 5% tolerance, a system with many electronic neurons has a built-in test for the robustness of the observed results.

We connect such electronic neurons with electronic synapses inspired in biological chemical synapses. The electronic synapses share the same properties of the electronic neurons: easy mathematical description, built with simple electronic components and scalability. The electronic synapses are also flexible in the sense that they can be made either excitatory or inhibitory with a simple modification in the circuit.

To complement the results of this thesis we also employ numerical simulations of our electronic models for neurons and synapses and also of well known models in the literature such as the FitzHugh-Nagumo model.

In the following chapters we provide an extensive discussion of the electronic neuron and

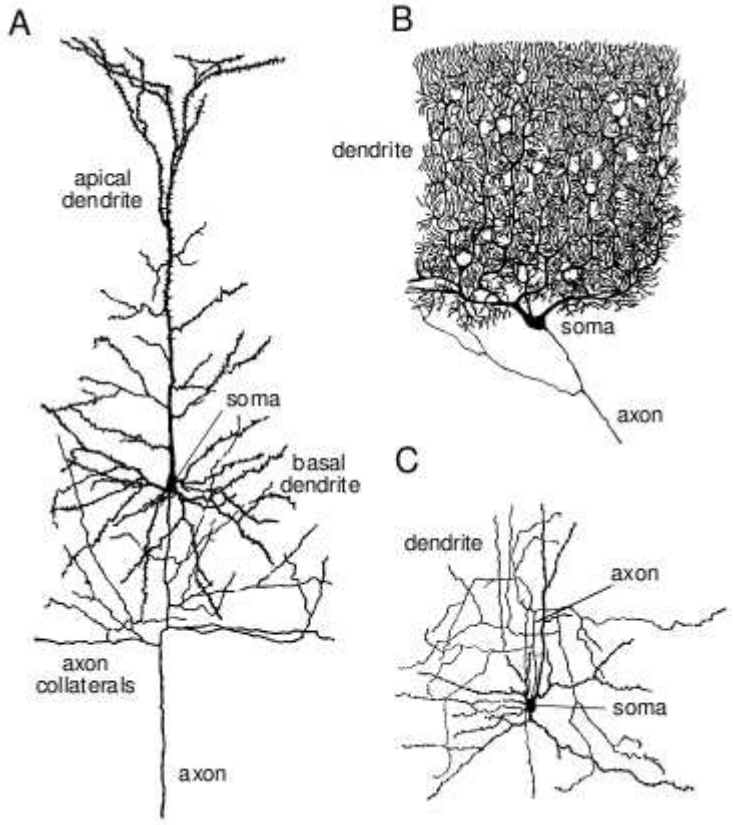


**Figure 1.1** Diagrams for three types of neuron. A) Cortical pyramidal cell. These are the primary excitatory neuron cells in the brain cortex of mammals. The axon of pyramidal cells bifurcates locally, creating connections (synapses) with close neurons as well as reaching farther parts of the brain and nervous system due to its long projection. B) Cerebellum Purkinje cell. The axon from these cells transmit signals from the cerebellum cortex. C) Brain cortex stellate cell. These cells belong to large class of cells responsible for sending inhibitory signals for neurons in the brain cortex. The diagrams sizes are about 150 times greater than the corresponding neurons (a typical cellular body (soma) has diameter of order 15 $\mu$m.) (Extracted from Peter Dayan and L.F. Abbott (2001) [1]).

electronic synapse model, and the phenomena that arise from a single neuron as well connected neuron networks.

## 1.1 Review of basic neuron physiology

Neurons are remarkable among other cells due to their ability to quickly transmit long range signals. Although they appear in a great variety of shapes and sizes, a typical neuron can be divided in the basic structures: cellular body (also known as soma), dendrites and axon. Dendrites are branched projections of the cellular body, that together originate the dendritic tree of the neuron. Along with the soma, the dendrites are typically responsible to receive signals from synapses of other neurons. The axon is a special projection of the cellular body, usually

| Ion | Cytoplasm concentration (mM) | Extra cellular medium concentration (mM) | Equilibrium potential (mV) |
|---|---|---|---|
| $K^+$ | 400 | 20 | -75 |
| $Na^+$ | 50 | 440 | +55 |
| $Cl^-$ | 52 | 560 | -60 |
| $A^-$ | 385 | - | - |

**Table 1.1** Concentration of the main ions across a resting cellular membrane of the squid giant axon. $A^-$ stands for organic molecules with net negative charge. (Data from E.R. Kandel (2000) [2]).

much longer than the dendrites, that originates at region called axon hillock and is responsible for sending signal to other neurons across great distances. The soma can generate multiple dendrite branches, but usually no more than one axon, although the axon can branch itself many times along its path. Figure 1.1 shows how the dendrites and the axon are arranged in different types of neuron.

Neurons produce electric signals when the cellular membrane is submitted to potential difference between intra and extracellular media. The cellular membrane is composed of a phospholipid bilayer that serves as an electric insulator due to its hydrophobic property. In a resting state, neurons tend to accumulate potassium ions in their interior, while the extracellular medium has an excess of negative ions. Since the outside medium is usually defined to have zero electric potential, common neurons have negative resting potentials, with values between $-60$ mV and $-70$ mV. Table 1.1 shows the concentrations of the most common ions across the membrane of the squid giant axon, whose blood has ion concentrations similar to those of ocean water.

The membrane also has embedded proteins with various functions. Among those, the ionic channels allow the flux of ions through the membrane. The passive ionic channels are responsible for the maintenance of the membrane's rest potential and are always open allowing the diffusion of ions. The net flux through the passive channels is limited by the equilibrium potential (shown in Table 1.1) where the diffusion forces are balanced by electric force in the opposite direction, resulting in no net flow of the ion through the membrane. The value of the equilibrium potential $E_X$ for an ion $X$ can be obtained from the Nernst equation, which can be derived from thermodynamics:

$$E_X = \frac{RT}{zF} \ln\left(\frac{[X_o]}{[X_i]}\right), \tag{1.1}$$

where $R$ is the gas constant, $T$ is the temperature in kelvins, $z$ is the ion valence, $F$ is the Faraday constant and $[X_0]$ and $[X_i]$ are the concentrations of the ion outside and inside the cell, respectively. The resting potential $V_{rest}$ of the membrane can be determined in a similar fashion by the Goldamn equation, which takes into account the contribution of each ion in terms of its permeability $P$ and concentration:

$$V_{rest} = \frac{RT}{F} ln\left(\frac{P_K[K_o^+] + P_{NA}[Na_o^+] + P_{Cl}[Cl_i^-]}{P_K[K_i^+] + P_{NA}[Na_i^+] + P_{Cl}[Cl_o^-]}\right). \tag{1.2}$$

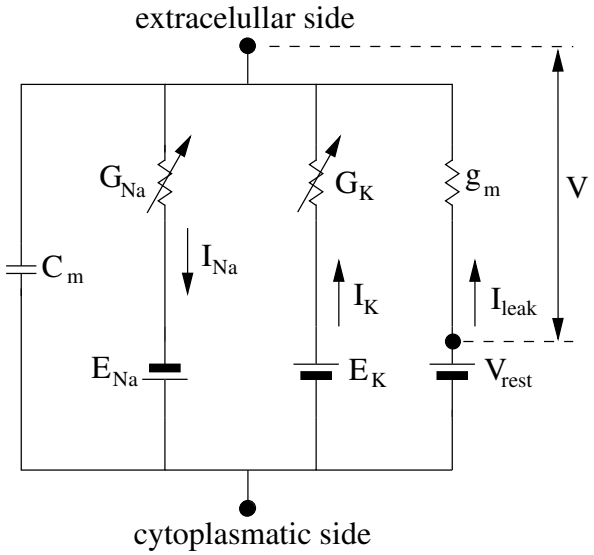


**Figure 1.2** Equivalent circuit for the Hodgkin-Huxley model. The conductances $G_{Na}$ e $G_K$ correspond to the sodium and potassium voltage dependent ion channels respectively. $g_m$ is the conductance of the combined passive ion channels. The potential $V$ is measured relative to the membrane resting potential $V_{rest}$.

Another kind of ionic channels opens or closes only in response to changes in the membrane potential. They are called active ionic channels or voltage dependent channels and are the main factor in the creation of the electric signals, called spikes or action potentials, that are transmitted through the axon.

The properties of the cellular membrane of a neuron can be put together in a circuit equivalent model which can be used to determine its response to external stimuli, like currents coming to the soma from the dendritic tree. In this model ion channels are represented by conductances coupled with batteries with electromotive force corresponding to the equilibrium potential of each ion. The neuron bilayer membrane acts as a capacitor with typical capacitance values around $1\mu$F/cm$^2$. For active ion channels the conductances are dependent on the current membrane voltage. In Fig. 1.2 we show the circuit equivalent model for the membrane mechanism for generating action potential of the squid giant axon, which is described mathematically by the Hodgkin and Huxley equations (see below).

More details concerning neuronal physiology can be found in E.R. Kandel (2000) [2], from which this section was based on.

Before moving to mathematical models of neuronal excitability, we now focus on the subject of excitable elements in general, which neurons are a part of.

## 1.2 Excitable elements and excitable media

Excitability is a common phenomena in nature, occurring, for example, in forest fires, chemical reactions, lasers, neuronal systems, heart tissue, climate dynamics and many others.

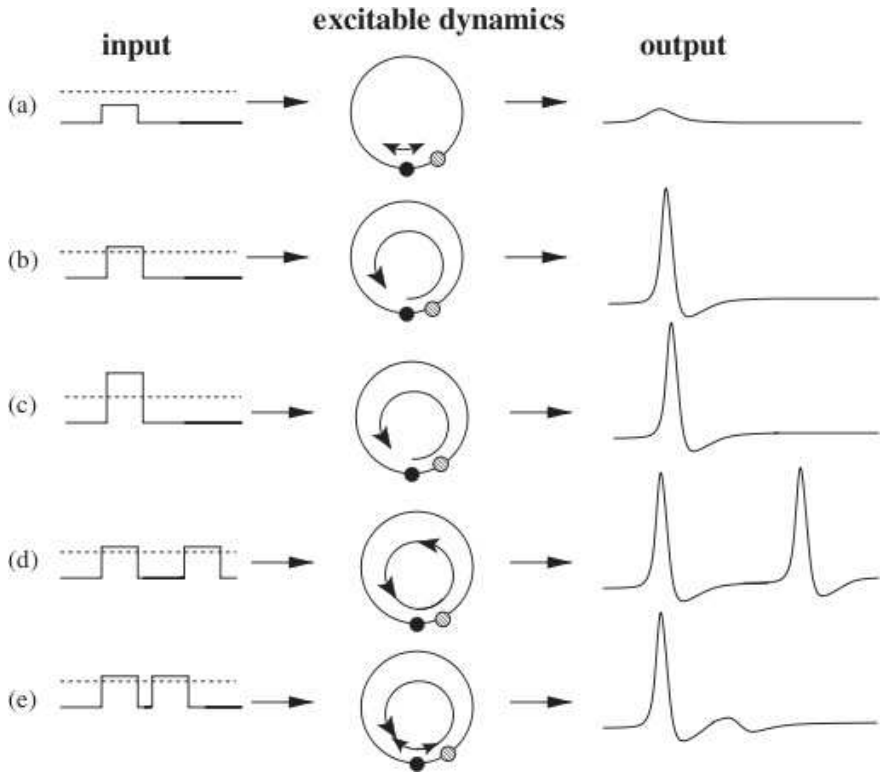


**Figure 1.3** Excitable elements dynamics: different kinds of stimuli (left-hand column) produce different kinds of response (right-hand column), each corresponding to type of system dynamic (middle column). a) A low intensity stimulus (below threshold) induces a small amplitude response and the system remains around the rest state (full circle in the middle column). b) Above threshold stimulation takes the system away from the rest state, crossing an unstable fixed point or a quasi-separatrix (empty circle in the middle column), resulting in big amplitude response, i.e. a spike. c) Further increase in the stimulus intensity does not significantly alter the shape of the spike response. d) Two stimuli with long time separations induce two spikes. In the other hand, closely timed stimuli only induce one spike corresponding the first stimulus. In this case, due to the refractory state, there is no second spike. (Extracted from B. Lindner *et al.* (2004) [3])

A common property to all excitable elements is the existence of a rest state, an excited state and a refractory state. Figure 1.3 shows the general types of behavior presented by excitable elements when subjected to different forms of stimuli. If there is no stimulation the excitable element stays at its rest state. In the other hand, if there is an external stimulus, the excitable element can assume two distinct responses: for low intensity stimulus a small amplitude response is produced (Fig. 1.3a); if the stimulus reaches or surpasses a certain threshold, the element leaves the rest state, going through the excited state followed by the refractory state. The response to above-threshold stimuli is highly non-linear and correspond to a great "walk" of the system dynamical variables across the phase space. In this case, it is said that a spike has occurred (Fig. 1.3b). The response of the excitable element to stimuli is "all or nothing", i.e. the shape of the spike is approximately independent of the intensity of the stimulus if it is above the threshold (Fig. 1.3c). After the spike the excitable element reaches the refractory

state, and for its duration new stimuli (even those above the excitation threshold) do not induce new spikes (Fig. 1.3e). After the refractory state, the excitable element returns to the rest state and is able to produce new spikes (fire) again (Fig. 1.3d).

In general, excitable elements rarely present themselves in nature in a isolated way. They usually are part of complex networks where interesting collective phenomena arise. A network of excitable elements is usually called an excitable medium. One of its main characteristics is the ability to propagate signals actively, with no loss of amplitude. For example, a forest fire travels across the forest like a wave from its origin point and regenerates itself at every new tree the fire encounters. Active propagation of signal differs from passive propagation, where a steady loss of signal amplitude is caused by the damping properties of the medium. Sound waves are an example of passive signal propagation.

In the following sections, we will discuss, with the help of mathematical models how neurons relate to excitable elements and in particular, we will show how the mentioned behaviors and states (rest, excited and refractory) emerge from the equations.

## 1.3 Neurons as dynamical systems

Non-linear dynamics can be used to describe a great variety of phenomena that occur in nature, from population growth to firefly synchronization [4]. In the realm of neuroscience many dynamic models describe neuronal behavior, but here we will focus on two of them: the very important work of Alan Hodgkin and Andrew Huxley [5, 6, 7, 8] which describes the squid giant axon and a simplified version of this model by Richard FitzHugh [9] and J. Nagumo [10]. We begin by giving a very brief introduction to non-linear dynamics concepts.

An $n$-dimensional dynamical system can be described as:

$$\dot{\vec{x}} = \vec{f}(\vec{x}), \tag{1.3}$$

where $\vec{x} = (x_1, \ldots, x_n)$ is the set of dynamical variables, $\vec{f} = (f_1, \ldots, f_n)$ is the set of functions, usually non-linear, that define the system and the dot ($\dot{}$) corresponds to a time derivative. The space of the variable $\vec{x}$ is called phase space of the system and the time evolution of the system corresponds to a trajectory of a point in phase space. The equation

$$\dot{\vec{x}} = 0 \tag{1.4}$$

defines $n$ curves in phase space, which are called nullclines. On top of each nullcline there is no flux (null rate of change) in one of the directions of the phase space. If there is a point in phase space where all the nullclines meet, this point is called a fixed point. A system that starts on a fixed point will stay on it if kept unperturbed since the rate of change in all directions on fixed point is zero. The fixed point is said to be stable if trajectories arbitrarily close to the fixed point converge to it, and unstable if they diverge from it. To determine the stability of the fixed point it is useful to linearize the equations that define the system in the vicinity of the fixed point.

Let $\vec{x}^*$ be a fixed point of the system. The Equation (1.3) can be written as Taylor series up to first order around $\vec{x}^*$ in the following way:

$$\dot{\vec{x}} = \vec{f}(\vec{x}^*) + \sum_i^n \frac{\partial \vec{f}}{\partial x_i}\Big|_{\vec{x}^*} (x_i - x_i^*) + \ldots \tag{1.5}$$

By definition, $\vec{f}(\vec{x}^*) = 0$. Defining $x_i - x_i^* = y_i$ as the new system variable, which is equivalent to a perturbation around the equilibrium point $\vec{x}^*$, we note that $\dot{x}_i = \dot{y}_i$. Furthermore $\frac{\partial}{\partial x_i} = \frac{\partial}{\partial y_i}$, which, ignoring terms of order $O(y_i^2)$, leads to:

$$\dot{\vec{y}} \cong \sum_i^n \frac{\partial \vec{f}}{\partial y_i}\Big|_{\vec{x}^*} y_i. \tag{1.6}$$

Equation (1.6) is the linearized form of the original system in Eq. (1.3) and it describes how a perturbation $\vec{y} = (y_1, \ldots, y_n)$ evolve in the close to the fixed point. Equation (1.6) can also be written in matrix form $\dot{\vec{y}} = A\vec{y}$ where $A$ is the jacobian matrix of the system:

$$A_{ij} = \frac{\partial f_i}{\partial y_j}\Big|_{\vec{x}^*}. \tag{1.7}$$

Let $\vec{v}_\alpha$ and $\lambda_\alpha$ be, respectively, the eigenvectors and eigenvalues of the matrix $A$. Therefore:

$$A\vec{v}_\alpha = \lambda_\alpha \vec{v}_\alpha. \tag{1.8}$$

This implies that the general solution to Eq. (1.6) is:

$$\vec{y}(t) = \sum_\alpha c_\alpha \vec{v}_\alpha e^{\lambda_\alpha t}. \tag{1.9}$$

The stability of the fixed point $\vec{x}^*$ depends on the sign of the real part of the eigenvalues. If some eigenvalues have positive real part most perturbations will grow exponentially and the trajectories will leave the neighborhood of the fixed point. In this case the fixed point is a unstable node. If all eigenvalues have negative real part the perturbations will decay exponentially and the trajectories will get closer to the fixed point. In this case the fixed point is a stable node. If only some of the eigenvalues have positive real part and rest of them has negative real part, the fixed point is said to be a saddle.

If the imaginary part of the eigenvalues is different from zero, the trajectories will oscillate around the fixed point. In this case a stable (unstable) node becomes a stable (unstable) spiral.

If, in a dynamical system with 2 variables, the variation of a control parameter changes the signal of both eigenvalues while the imaginary parts are different from zero, the system is said to undergo a Hopf bifurcation (see Fig. 1.20).

Stability analysis of the fixed points will be important for the following description of the FitzHugh-Nagumo model and for the model of our electronic neuron.

## 1.4 Neuronal models of excitability

### 1.4.1 The Hodgkin-Huxley model

Figure 1.4 shows different kinds of action potentials (spikes) in vertebrate and invertebrate animals. They all have in common the relative independence of the spike shape with the receiving stimulus and the existence of a threshold for triggering the spikes. In particular, Fig. 1.4A shows the spike in the squid giant axon.

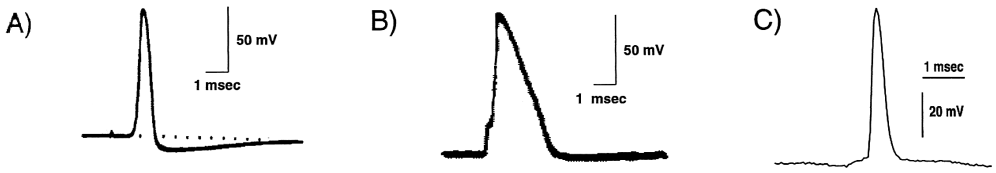


**Figure 1.4** Action potentials (spikes) in different kinds of vertebrate and invertebrate preparations. A) Squid giant axon at 16ºC. B) Axon spike of Ranvier node in a myelinated nerve fiber of a frog at 22ºC. C) Cat visual cortex at 37ºC. (Adapted from Christof Koch (1999) [11])

The mechanisms responsible for the production of action potentials in nervous tissue have been elucidated by various authors through the study of the squid giant axon. Among them, the most notable are Alan Hodgkin and Andrew Huxley who described the ionic mechanisms in a series of papers [5, 6, 7, 8] and, along with Eccles, shared the Physiology Nobel prize in 1963.

The squid giant axon has a diameter of about half millimeter, which is a thousand times bigger than the diameter of the usual axon. To avoid spacial distribution complexities, Hodgkin and Huxley used a technique known as space clamp: a thin highly conductor wire was introduced along the axon interior, rendering its membrane potential equal in all its extension. With the help of other techniques such as voltage clamp and the use of substances capable of blocking specific ionic channels, they were able to separate the membrane current $I_m$ in its two components: the ionic and the capacitive currents:

$$I_m(t) = I_{\text{ionic}}(t) + C_m \frac{dV}{dt}. \tag{1.10}$$

Hodgkin and Huxley detected that spike generation in the squid giant axon is related to sodium ($Na^+$) and potassium ($K^+$) voltage dependent ionic channels. These channels and all the currents across the axon membrane are represented in Fig. 1.2 in a equivalent circuit diagram. In this diagram, the passive ionic channels, which also contribute to the ionic current flowing though the membrane with a current $I_{leak}$, are put together in a single conductance $g_m$ coupled with battery of electromotive force equal to the rest potential $V_{rest}$ of the membrane. Therefore, the total ionic current through the membrane is given by:

$$I_{\text{ionic}} = I_{Na} + I_K + I_{leak}. \tag{1.11}$$

The ionic currents for each ion "i" are related to the membrane potential by the Ohm's law:

$$I_i = G_i(V(t),t)(V(t) - E_i), \tag{1.12}$$

where the potential $V(t)$ is measured relative to the membrane rest potential and $E_i$ refers to the equilibrium potential of the ion "i" (given by Eq. (1.1)), also measured relative to the membrane rest potential.

In their empirical model, Hodgkin and Huxley [8] proposed that the potassium ion current in the voltage dependent channels are as follows:

$$I_K = \overline{G}_K n^4 (V - E_K), \tag{1.13}$$

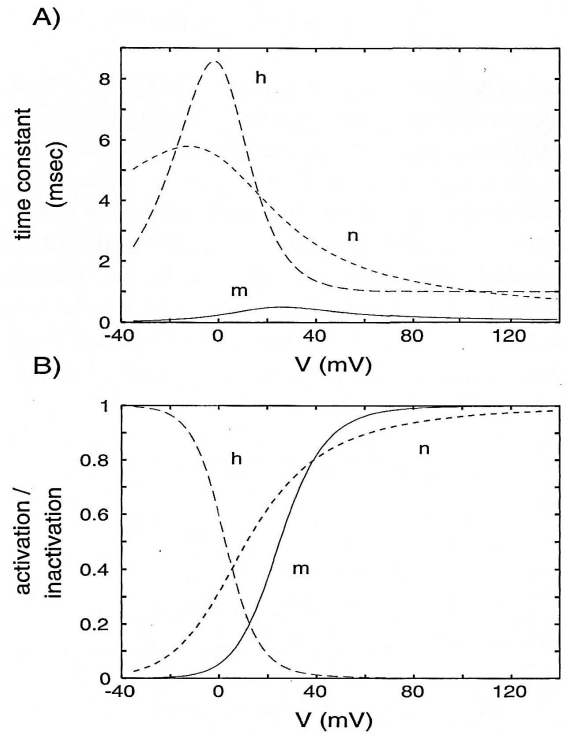


**Figure 1.5** Time constants (A) and rest states (B) as functions of the membrane potential $V$ for the sodium activation particle $m$ (solid line) and inactivation particle $h$ (long dashed line) and for the potassium activation particle $n$ (short dashed line). (Extracted from Christof Koch (1999) [11])

where $\overline{G}_K$ is the maximum value of the conductance $G_K$ (36 mS/cm$^2$) and $E_K = -12$mV is the potassium equilibrium potential relative to the membrane rest potential. The variable $n$ describes the state of fictional activation particle with values ranging from 0 to 1. The activation particles can exist in two states only: open or closed. For a voltage dependent channel to be open, it is required that all activation particles are open at the same time. In the case of the potassium ion there are four activation particles. In this context $n$ corresponds to the probability of one the activation particle is in a open state. Consequently it is in a closed state with probability $1-n$. The activation particles can move between the two states through a first order reaction:

$$n \underset{\alpha_n}{\overset{\beta_n}{\rightleftharpoons}} 1-n, \tag{1.14}$$

where $\alpha_n$ is the transition rate between the close and open state and $\beta_n$ is the transition rate in the reverse order. Both rates depend on the membrane potential $V$ and the corresponding reactions can be described as a differential equation:

$$\frac{dn}{dt} = \alpha_n(V)(1-n) - \beta_n(V)n, \tag{1.15}$$

which is equivalent to the equation

$$\frac{dn}{dt} = \frac{n_\infty - n}{\tau_n}, \tag{1.16}$$

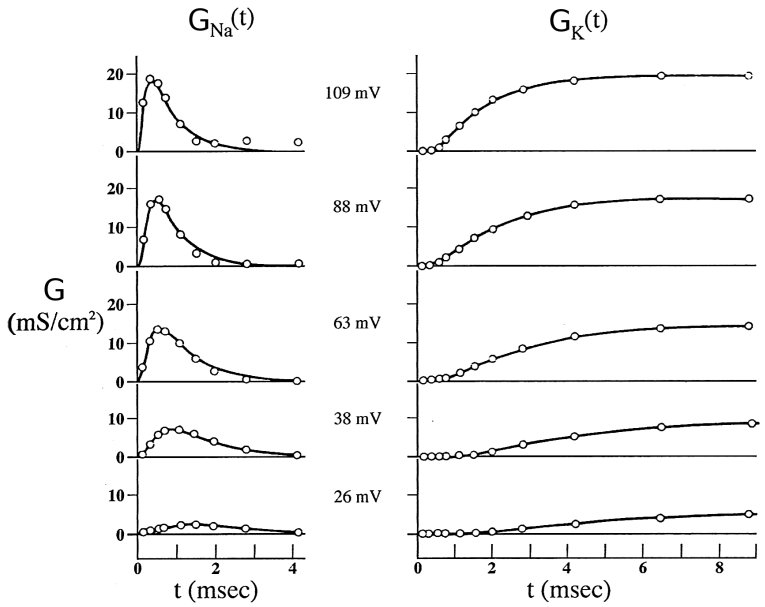


**Figure 1.6** Changes in the conductances of ions $K^+$ and $Na^+$ during the injection of a depolarizing external voltage to the squid giant axon membrane at 6.3ºC temperature (circles represent experimental data and lines for the model prediction). For more intense external voltage $G_{Na}$ grows faster before falling down to zero (due the inactivation) while $G_K$ remains active. (Extracted from Christof Koch (1999) [11])

where

$$\tau_n = \frac{1}{\alpha_n + \beta_n} \tag{1.17}$$

and

$$n_\infty = \frac{\alpha_n}{\alpha_n + \beta_n}. \tag{1.18}$$

In Eq. (1.16), $n_\infty$ is the value of the rest state of the particle $n$ (as $t \to \infty$) and $\tau_n$ is a time constant dependent of the membrane potential.

The dependency of $n_\infty$ and $\tau_n$ with the membrane potential $V$ proposed by Hodgkin and Huxley based on their biological measurements of the squid giant axon is showed in Fig. 1.5. While $\tau_n$ reaches a maximum and then falls down, $n_\infty$ is a monotonically growing function of $V$. The conductance of the voltage dependent potassium ion channels is showed in Fig. 1.6 when the membrane is submitted to a constant external depolarizing voltage (voltage clamp) and it is observed that membrane depolarization leads to a $K^+$ conductance increase.

The conductance dynamics for the $Na^+$ ion is different from that of the $K^+$ ion as is showed on Fig. 1.6. To incorporate this behavior to their model, Hodgkin e Huxley proposed the existence of one inactivation particle $h$ and three activation particles $m$:

$$I_{Na} = \overline{G}_{Na} m^3 h (V - E_{Na}), \tag{1.19}$$

where $\overline{G}_{Na}$ is the maximum value of the sodium conductance ($\overline{G}_{Na} = 120$ mS/cm$^2$) and $E_{Na}$ is the sodium equilibrium potential relative to the membrane rest potential ($E_{Na} = 115$mV).

$m$ e $h$, like $n$, range from 0 to 1 and they are assumed to be independent, therefore following independent transition reactions:

$$\frac{dm}{dt} = \frac{m_\infty - m}{\tau_m} \tag{1.20a}$$

$$\frac{dh}{dt} = \frac{h_\infty - h}{\tau_h}. \tag{1.20b}$$

Equations (1.20) were obtained in the same way used to write Eq. (1.16). Note that $h$ corresponds to the probability that the inactivation particle is not in its closed state. For the sodium voltage dependent ion channels to be open it is required that the three activation particles are in their open state and the inactivation particle is not in its closed state. Figure 1.5 shows the time constants and rest states of the variables $m$ and $h$. Both $\tau_m$ and $\tau_h$ reach a maximum as $V$ increases, but $\tau_h$ is about ten times greater than $\tau_m$. While $m_\infty$ increases monotonically as $V$ increases, $h_\infty$ decreases.

At the membrane rest state ($V = 0$), the fraction of open sodium voltage dependent ion channels corresponds to less the 1% of the maximum conductance. For $V$ values below or close to the rest potential the activation variable $m$ is close to 0, while the inactivation variable $h$ is close to 0 for positive values of $V$ (depolarized membrane) (Fig. 1.5). Therefore the sodium ionic current $\overline{G}_{Na} m_\infty^3 h_\infty (V - E_{Na})$ during the membrane rest state always has a low intensity. To induce high intensity current values in the sodium voltage dependents ion channels a rapid membrane depolarization is necessary: the time constant $\tau_m$ is much smaller than $\tau_h$ and for this reason $m$ quickly reaches the value 1 (about 1 ms) increasing the sodium conductance, while $h$ falls down slowly to zero (about 5 ms) resulting in a slow conductance reduction. Figure 1.6 shows the rapid growing of the $Na^+$ conductance, followed by a slow decay in response to a depolarizing voltage.

The final equation of the model puts together all the currents flowing through the membrane of the axon:

$$C_m \frac{dV}{dt} = \overline{G}_{Na} m^3 h (E_{Na} - V) + \overline{G}_k n^4 (E_K - V) - g_m V + I_{inj}, \tag{1.21}$$

where $I_{inj}$ is the external current injected in the membrane, e.g. through an intracellular electrode or through a synapse. This last equation and Equations (1.16) and (1.20) which describe the time evolution of the variables $n$, $m$ and $h$ determine a 4-dimensional non-linear dynamical system from which the generation of action potentials can be explained.

Consider a short current pulse being injected inside the membrane (Fig. 1.7). For a low intensity pulse, the little depolarization would lead to a small increase in the variables $n$ and $m$ and a small decrease in $h$. This would cause an increase in the sodium and potassium conductances, but, as the potassium current is greater that the sodium current, the membrane potential would return to its rest potential after a brief hyperpolarization period. If the current pulse intensity is increased above an excitation threshold, the resulting depolarization would cause sodium current to surpass the potassium current triggering a positive feedback process: the current $I_{Na}$ depolarizes the membrane, increasing the activation variable $m$, leading to increase in the sodium conductance $G_{Na}$, which in turn further increases $I_{Na}$. This process happens in short spam of time due to the small value of the time constant $\tau_m$ (0.1 to 0.2 ms) and, as a result, the membrane potential reaches positive values (depolarizes). After a while, the sodium

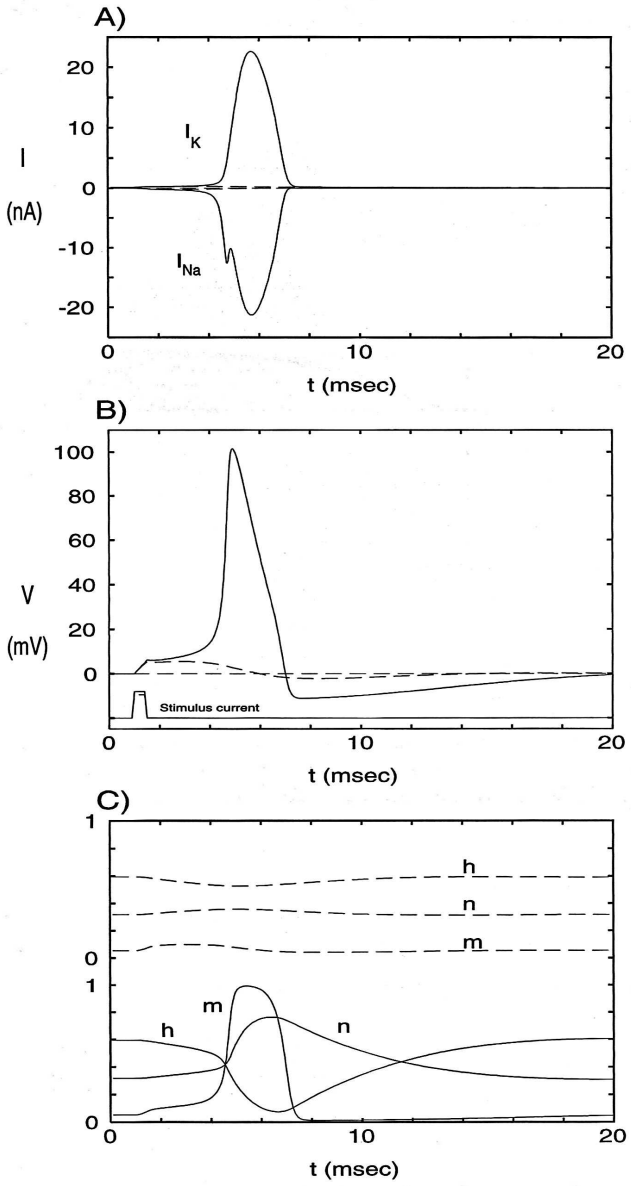


**Figure 1.7** Action potential in the Hodgkin-Huxley model produced as a response to a current pulse of duration 0.5 ms and in intensity 0.4 mA (solid line) in comparison to the response to a equally long pulse but with intensity 0.36 mA below the excitation threshold (dashed line). A) Sodium and potassium ionic currents $I_{Na}$ and $I_K$. B) Membrane potential response to stimuli either above or below excitation threshold. The injected current charges the membrane capacitance, making the current $I_{Na}$ greater than the $I_K$. The less intense current pulse does not induce an action potential, but induces a small depolarization followed by membrane hyperpolarization due to the activation of potassium channels. C) Dynamics of the activation and inactivation variables. $m$ changes much faster than $h$ or $n$. The slow recovery of $h$ and $n$ explain why the membrane hyperpolarizes after the initial potential peak and goes through a refractory state. (Extracted from Christof Koch (1999) [11])

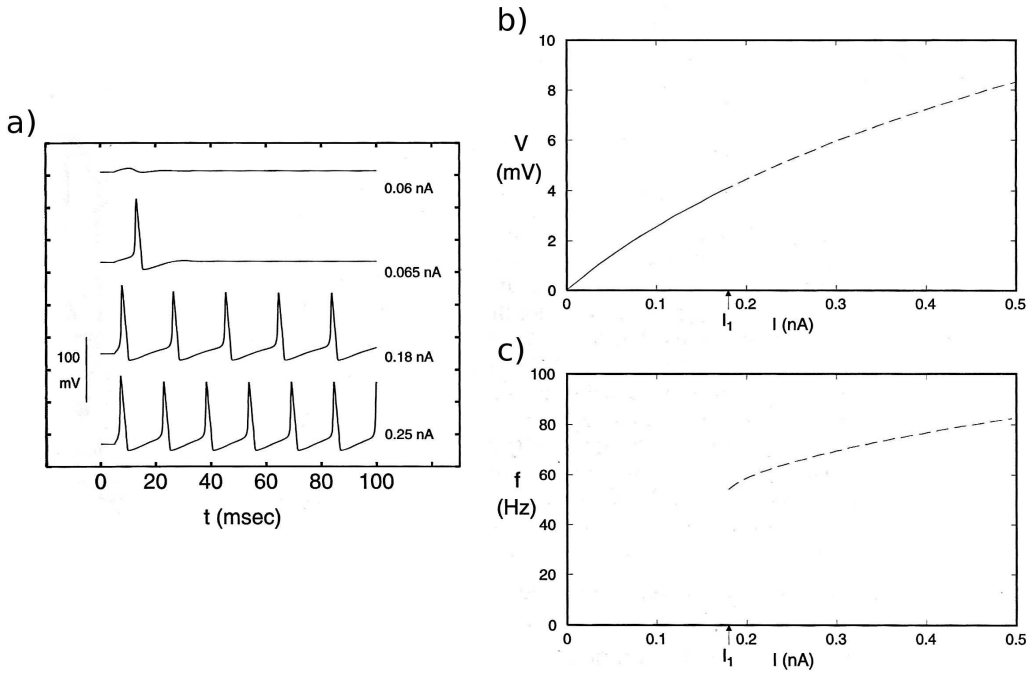


**Figure 1.8** A) Membrane potential response to the injection of constant currents. The membrane generates a spike if the current intensity reaches the excitation threshold. Increasing the current to greater values induces a spike train response. B) Membrane potential in its rest state as a function of the inject current. C) Firing frequency as a function of the current intensity. Up until the intensity $I_1$ the membrane responds with a constant depolarization (solid line). After this point the system loses its stability and begins to oscillate in a limit cycle (dashed line). (Adapted from Christof Koch (1999) [11])

inactivation $h$ is reduced to values near zero, counteracting the positive feedback increase of the sodium conductance. Potassium activation $n$ also kicks into action delayed relative to the variable $m$, causing a further decrease of the total current flowing in the membrane. As the sodium current reaches zero due to its inactivation $h$ in approximately 1 ms and the potassium current lasting a while longer, the membrane potential becomes negative (hyperpolarization), which corresponds to the refractory state. In these low potentials, the potassium activation "turns off" and the membrane finally reaches its rest potential again.

An interesting property of the Hodgkin-Huxley model can be observed when the membrane is submitted to a constant depolarizing current injection $I_{inj}$. If the current intensity is below an excitation threshold, the membrane changes its rest potential to slightly depolarized value without generating spikes. For a slightly above threshold current intensity, the membrane fires one spike and returns to a new rest state with potential above its previous rest state. A further increase int the current intensity leads the membrane to generate a spike train (equally spaced action potentials) that lasts while the current is active. The system is said to have lost its stability and is now moving through the phase space in a limit cycle. Spike trains and the dependency of the firing frequency with the intensity of the injected current are shown in Fig. 1.8.

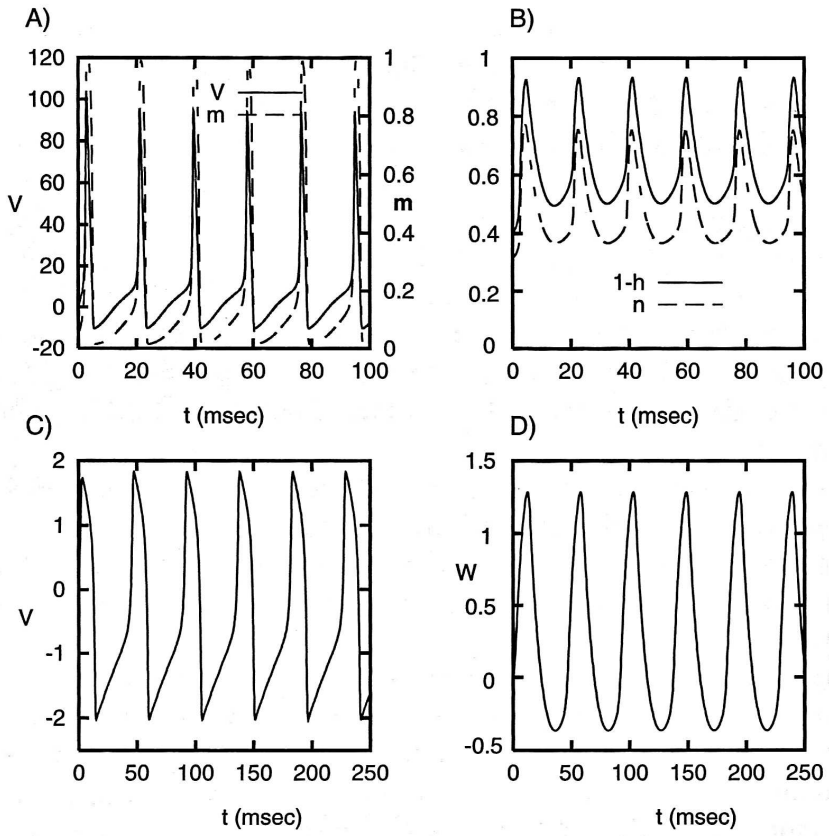


**Figure 1.9** Comparison between the time scales of the FitzHugh-Nagumo and Hodgkin-Huxley models. A) Membrane potential $V$ and the sodium activation variable $m$. B) Sodium inactivation variable $1-h$ and the potassium activation variable $n$. C) Excitation variable $V$ for the FitzHugh-Nagumo model. D) Recovery variable $W$ also for the FitzHugh-Nagumo model. (Extracted from Christof Koch (1999) [11])

### 1.4.2 The FitzHugh-Nagumo Model

The great quantitative precision of the Hodgkin-Huxley model in describing various membrane properties of the squid giant axon comes at the cost of detailed knowledge of ionic currents dynamics. Quantitative models of neuronal excitability that retain key features of membrane dynamics but with reduced complexity are good alternatives to the need for detailed neuronal structure knowledge. These simplified models can be employed in numerical simulations or electronic implementations, for example.

The FitzHugh-Nagumo model is a simplified version of the Hodgkin-Huxley model, justified by the fact that in this model, both the membrane potential $V(t)$ and the sodium activation variable $m$ have similar time scales. In the same fashion, the sodium inactivation variable $h$ and the potassium activation variable $n$ have comparable time scales, slower than the previous two. This becomes clear if $V$ and $m$ are plotted together with normalized coordinates (Fig. 1.9A), representing the system excitability. This similarity between the two variables allows them

to be grouped in a single activation variable $V$ (Fig. 1.9C). This is also valid for the variable $n$ and $1-h$ (Fig. 1.9B), leading to a single recovery variable $W$ (Fig. 1.9D). Qualitatively, the behavior of this bidimensional system is equivalent to the behavior of the 4-dimensional Hodgkin-Huxley system.

FitzHugh [9] and, independently, Nagumo, Arimoto and Yoshizawa [10], obtained the following set of equations that describes qualitatively the behavior of a excitable neuron:

$$\dot{V} = V - \frac{V^3}{3} - W - I \tag{1.22a}$$

$$\dot{W} = \phi(V + a - bW), \tag{1.22b}$$

where the parameters

$$a = 0.7,\ b = 0.8,\ \phi = 0.08, \tag{1.23}$$

are dimensionless, as well as the variables $V$ and $W$. The amplitude of the constant $\phi$, the equivalent of an inverse time constant, sets how fast the variable $V$ changes relative to $W$. For the chosen value $\phi = 0.08$, $V$ changes much faster the $W$ for $\dot{V}$ is typically $1/0.08 = 12.5$ times greater than $\dot{W}$. Therefore, the system dynamics consists of fast branches where $V$ changes so fast that $W$ can be taken as a constant, and slow branches where $W$ changes are more notable.

Due to the non-linearity of the Eqs. (1.22), finding analytic solutions is a hard task. However, the linear stability analysis can be used to discover qualitative features of the system. Firstly, we focus on the system nullclines. According to Eq. (1.4), the nullclines are obtained by making $\dot{V} = 0$ and $\dot{W} = 0$ in the Eqs. (1.22):

$$\dot{V} = 0 \Rightarrow W = V - \frac{V^3}{3} + I \tag{1.24a}$$

$$\dot{W} = 0 \Rightarrow W = (V + a)/b. \tag{1.24b}$$

The phase space of the FitzHugh-Nagumo model along with its nullclines is shown in Fig. 1.10. If the system current state (a point in the phase space) is on the $\dot{V} = 0$ nullcline, its trajectory will be vertical in the up (if $\dot{W} > 0$) or down (if $\dot{W} < 0$) direction. Furthermore, for all point above (below) the nullcline $\dot{V} = 0$, $\dot{V} < 0$ ($\dot{V} > 0$). In a similar way, if the system is on the $\dot{W} = 0$ nullcline, its trajectory is horizontal and for points to the left (right) of this nullcline $\dot{W} < 0$ ($\dot{W} > 0$).

The choice of parameters, particularly $b < 1$, leaves the system with only one possible fixed point $(V^*, W^*)$ and, if $I = 0$, $(V^*, W^*) = (-1.2, -0.625)$. Linearization of the Eqs. (1.22) around this fixed point leads to:

$$\begin{aligned} \dot{V}' &= (1 - (V^*)^2)V' - W' \\ \dot{W}' &= \phi(V' - bW'), \end{aligned} \tag{1.25}$$

where $V - V^* = V'$ e $W - W^* = W'$. The system in Eq. (1.25) can be written in matrix form $\dot{\vec{r}} = A\vec{r}$, where:

$$\vec{r} = \begin{pmatrix} V' \\ W' \end{pmatrix} \tag{1.26}$$

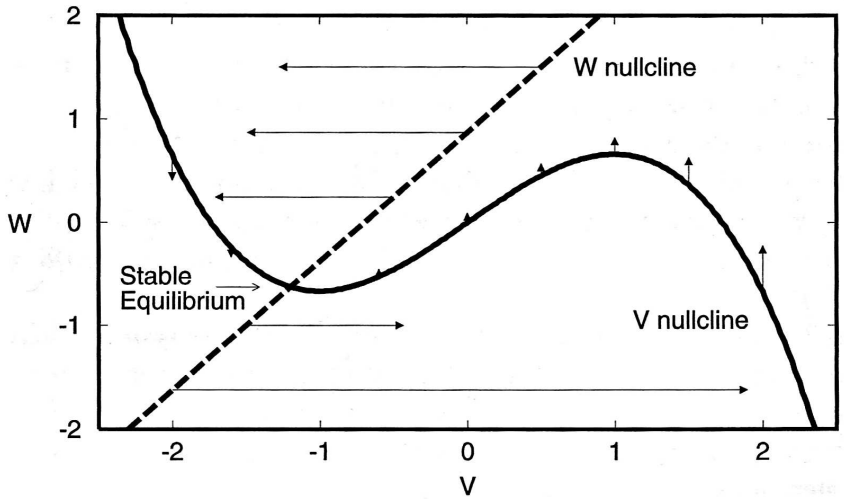


**Figure 1.10** Phase space and nullclines of the FitzHugh-Nagumo model for $I = 0$. The length of arrows are proportional to $(\dot{V}, \dot{W})$, the rate of change of the dynamical variables. Typically $V$ changes much faster than $W$. (Extracted from Christof Koch (1999) [11]).

and $A$ is the jacobian matrix of the system:

$$A = \begin{pmatrix} (1-(V^*)^2) & -1 \\ \phi & b\phi \end{pmatrix}. \tag{1.27}$$

Since it is linear, the system define by the Eqs. (1.25) has solutions like:

$$\vec{r} = c_1 \vec{r}_1 e^{\lambda_1 t} + c_2 \vec{r}_2 e^{\lambda_2 t}, \tag{1.28}$$

where $c_i$ are constants that depend on the initial conditions of the system, $\vec{r}_i$ are the eigenvectors of the jacobian matrix and $\lambda_i$ are the eigenvalues, which are obtained from the characteristic equation of the matrix $A$:

$$\lambda_{1,2} = \frac{-((V^*)^2 - 1 + b\phi) \pm \sqrt{((V^*)^2 - 1 - b\phi)^2 - 4\phi}}{2}. \tag{1.29}$$

For $I = 0$ the eigenvalues are complex conjugates with values $\lambda_{1,2} = -0.5 \pm 0.42i$. The eigenvalues have negative real part and non-zero imaginary parts and thereby the fixed point is stable and trajectories around it are spirals.

When submitted to current pulses, the FitzHugh-Nagumo model behaves similarly to the Hodgkin-Huxley model. Figure 1.11 shows the response of the model to instantaneous current pulses given by $I(t) = Q\delta(t)$. The current pulses changes the variable $V$ from its rest value at the stable fixed point ($V^* = -1.2$) by a quantity $Q$. For small intensity current pulses (small $Q$) the system returns quickly to the rest state $V^*$, but overshooting to values smaller than $V^*$ due to the spiral trajectories near the fixed point. If the intensity of the current pulse is increased to a point where $V$ reaches the values $-0.64$ the system will move away from the left-hand

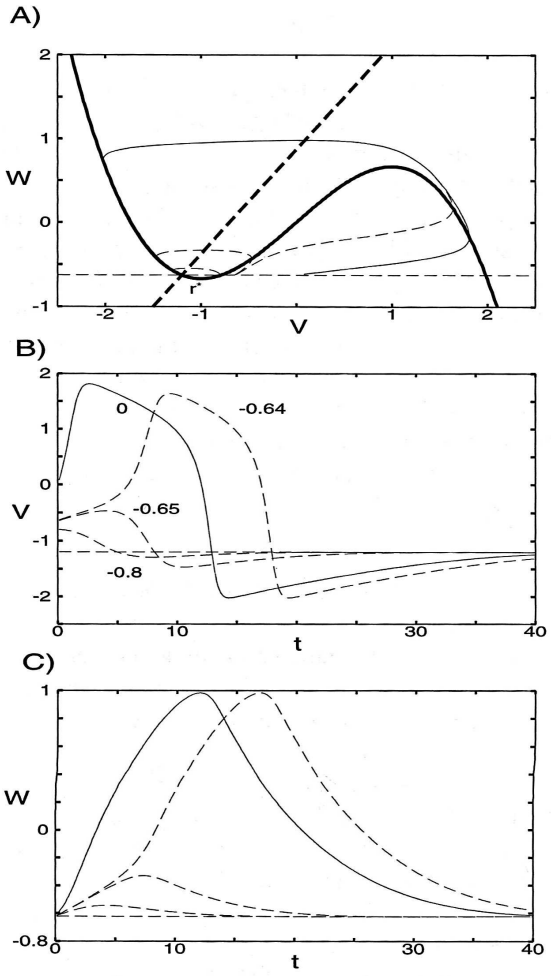


**Figure 1.11** A) A current pulse with intensity $I = Q\delta(t)$ stimulates the FitzHugh-Nagumo system, moving it away from its stationary state along the dashed horizontal line, increasing the value of $V$. B) and C) show the time evolution of the variables $V$ and $W$. If the initial change in $V$ caused by the current pulse causes it to reaches values up to $-0.65$ the system responds with a small depolarization and it returns quickly to the rest state. If, however, the change takes $V$ to values above $-0.64$ a spike is generated. faster than $W$. (Extracted from Christof Koch (1999) [11]).

branch $\dot{V} = 0$, with $V$ growing rapidly and $W$ remaining approximately constant until the right-hand branch of the nullcline $\dot{V} = 0$ is reached at the maximum $V$ value. This takes place due to the small value of $\phi$. Then, the phase space trajectory follows upwards slowly along the $\dot{V} = 0$ nullcline up until its local maximum. The system, then goes through a new fast moving phase, reaching $V$ values below that of the rest state, and then finally follows slowly downwards along the left-hand $\dot{V} = 0$ nullcline until it reaches its rest state again (Fig. 1.11A). While the system is hyperpolarized, i.e. close to the left-hand branch of the $\dot{V} = 0$ nullcline, it is required that the recovery variable $W$ returns to its rest state $W^* = -0.625$ before the system can make another trajectory like the one just described. Figures 1.11B and C show, respectively, the spike generated by the FitzHugh-Nagumo model and the recovery variable $W$.

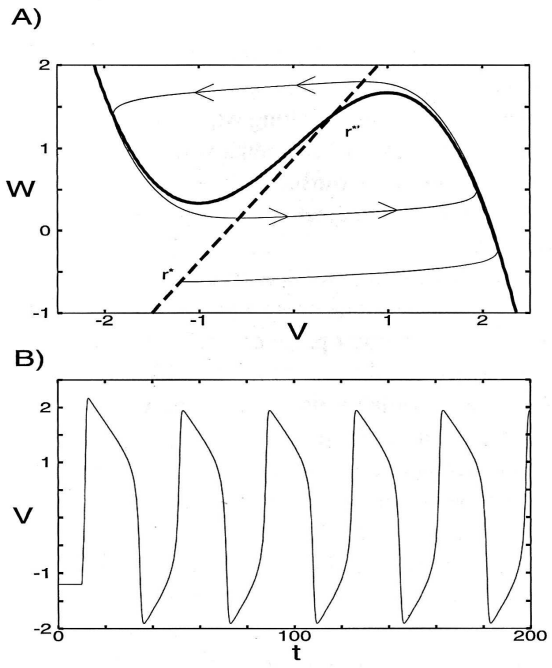


**Figure 1.12** Response of the FitzHugh-Nagumo model to constant current stimulation. The system is submitted to a constant current of intensity $I$. For $I < 0.32$ the new fixed point is stable and the system remains below the excitation threshold. A) For greater values (here $I = 1$) the new fixed point is located in the central branch of the $\dot{V} = 0$ nullcline a is unstable. In view of the limit cycle that appear in this case, a spike train is generated (B). (Extracted from Christof Koch (1999) [11]).

Although the all or none response is observed in the FitzHugh-Nagumo model, it does not have a well defined excitation threshold. From a numerical point of view, the intensity of the current pulse $I(t) = Q\delta(t)$ could be varied continuously from $-0.65$ to $-0.64$, creating all the intermediate trajectories in phase space between an small depolarization and a spike. This is known computationally as well as experimentally for the case of the squid giant axon, where there is only a separatrix region from which the possible responses diverge quickly to spikes or small depolarization. The size of this region in typical physiologic regimes, however, is so small that a all or none behavior is observed. For the FitzHugh-Nagumo model the constant $\phi$ controls the size of this separatrix region, with smaller $\phi$ rendering the region smaller [12].

If the system is stimulated with a constant depolarizing current, the $\dot{V} = 0$ nullcline will be shifted up in the phase space, while the $\dot{W} = 0$ will remain in the same position. This causes the position of the fixed point to change which may changes its stability. If the positive parts of the eigenvalues of the jacobian matrix become positive the fixed point will become unstable and small perturbations around the rest state will result in trajectories that tend to move away from the fixed point. According to Eq. (1.29), the real part of the eigenvalues changes sign for to values of $V^*$:

$$V_{\pm}^* = \pm\sqrt{1 - b\phi}, \tag{1.30}$$

therefore the fixed point is stable when the nullclines meet at the right hand and left hand

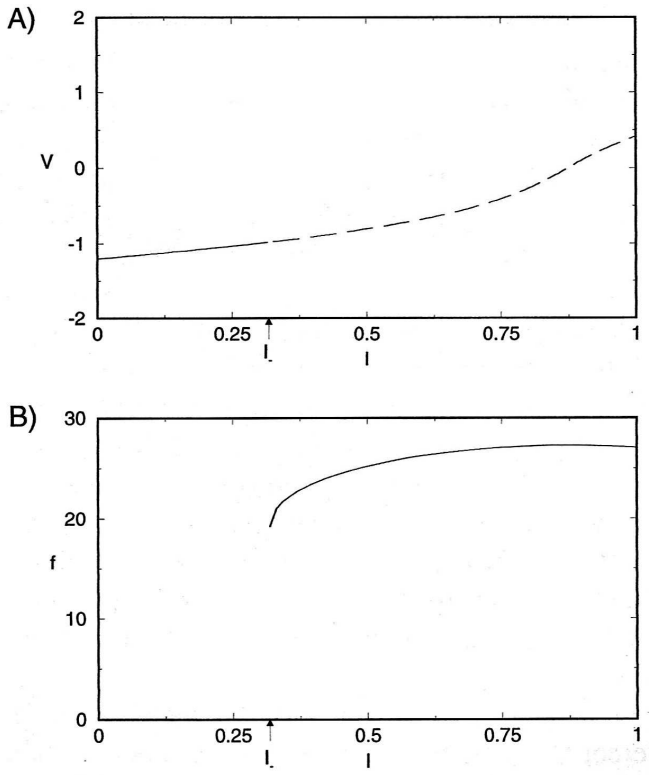


**Figure 1.13** A) Rest state of the activation variable $V$ as a function of the current $I$. For $I < I_-$ the fixed point is stable and $V$ adjusts itself to a new rest state. If $I > I_-$ the fixed point loses its stability and the system jumps to the stable limit cycle. B) Oscillation frequency as a function of the current $I$. Note that the minimum oscillation frequency is non-zero, which is indicative of a Hopf bifurcation. (Extracted from Christof Koch (1999) [11]).

branches of the $\dot{V} = 0$ nullcline. In the central branch of the $\dot{V} = 0$ nullcline $|V^*| < \sqrt{1 - b\phi}$ which makes the real part of the eigenvalues positive, making the fixed point unstable.

If the system is at its rest state $\vec{r}^*$ and is stimulated with a constant depolarizing current of low intensity, the real part of the eigenvalues remains negative and the new fixed point continue to be stable. If the current is between two critical values $I_- = 0.33$ and $I_+ = 1.42$, the nullclines meet at the central branch of the $\dot{V} = 0$ nullcline and fixed point becomes unstable. As shown in Fig. 1.12A the system goes on a trajectory that is similar to that of the spike generated by a strong enough current pulse. The key difference is that the system does not return to the new unstable fixed point $\vec{r}^{*I}$. In fact, the system remains on that oscillatory trajectory generating a infinite spike train (Fig. 1.12B). Since the oscillations are stable, the system is said to be on a stable limit cycle and trajectories starting in any point in the phase space, excluding the fixed point, will converge to the limit cycle.

The frequency of oscillations of the trajectories in the limit cycle is determined by the imaginary part of the eigenvalues of the jacobian matrix. The stability loss suffered by the fixed point when the constant current has values between $I_- = 0.33$ and $I_+ = 1.42$ makes the system oscillate with a non-zero starting frequency since the imaginary parts of the eigenvalues

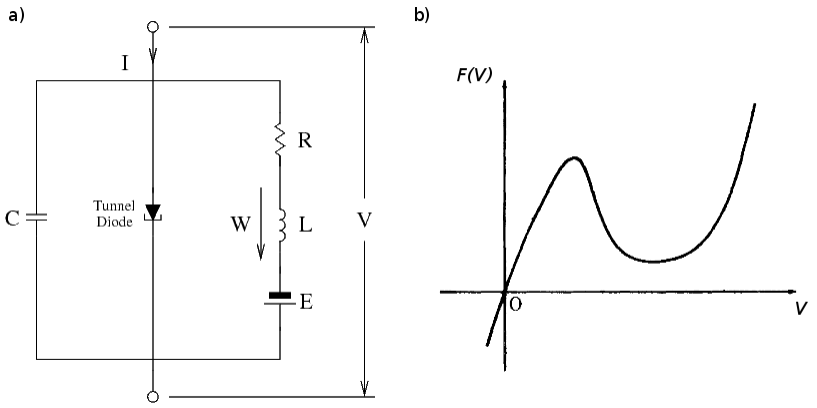


**Figure 1.14** Circuit proposed by Nagumo *et al.* (a) and response curve of a tunnel diode (b). (Adapted from Nagumo *et al.* (1962) [10])

are also non-zero. This kind of dynamical phenomenon where high amplitude oscillations appear with non-zero frequency as a result of the continuous change of a parameter is known as subcritical Hopf bifurcation. This phenomenon is notorious in the Hodgkin-Huxley model, where the minimum firing frequency of the spike trains is about 50 Hz. Experimentally this is also true for most axon membranes as well as for the generation of spike trains in the soma of certain kinds of neurons [13]. In the FitzHugh-Nagumo model the minimum firing frequency is about 23 Hz when $I = I_+$. Figure 1.13A shows the rest state value of the excitation variable $V$ as a function of the bifurcation parameter $I$. Figure 1.13B shows the oscillation frequency of the limit cycle as a function of the current $I$. The results are similar to those of the Hodgkin-Huxley model.

This last section was based on the textbook by Christof Koch (1999) [11].

## 1.5 Neurons modeled by electronic circuits

There are several electronic circuits reported in the literature which have been designed to present a neuron-like dynamical response. Here we present a collection of some of those circuits that have served different purposes, from simple reproduction of excitable behavior to interaction with real biological neurons.

The work of FitzHugh and Nagumo to obtain a simplified version of the Hodgkin-Huxley model was inspired in a non-linear oscillator model known as Bonhoeffer-van der Pol model, from which the FitzHugh-Nagumo model is a particular case. The analogical circuit proposed by Nagumo *et al.* [10] (Fig. 1.14a) replicates the cubic non-linearity of Eq. (1.22)a using the interesting property of a tunnel diode. Figure 1.14b shows that for the tunnel diode there is a region where it operates with negative resistance, i.e. the current through it decreases with increasing applied voltage.

From Kirchoff's laws, it is easy to note that the circuit in Fig 1.14a leads to the following

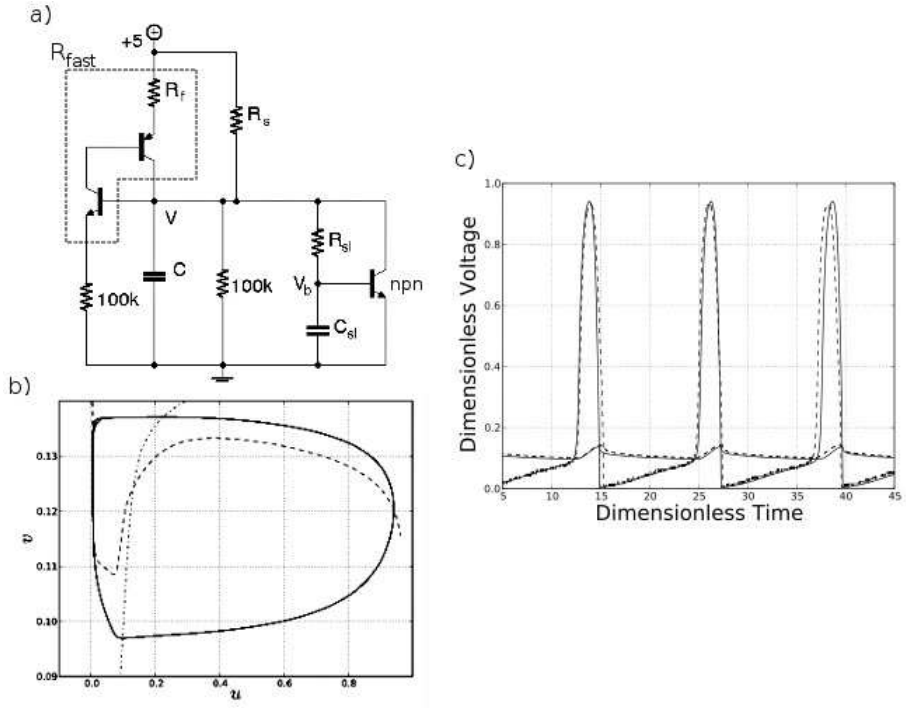


**Figure 1.15** Three transistors excitable circuit proposed by Lancaster and Helen. a) The dynamics of the region delimited by the dashed line is modeled by a resistance with value depending on the voltage $V$ at the capacitor $C$. b) Numerical simulation of the circuit phase space showing the nullclines of the variables $V$ e $V_b$ and the system trajectory during a spike. c) Experimental spike train (dashed line) and numerical simulations (solid lines). (Adapted from Lancaster and Helen (2010) [14])

set of equations:

$$\begin{aligned} C\dot{V} &= I - F(V) - W \\ L\dot{W} &= E - RW + V, \end{aligned} \tag{1.31}$$

where $I$ is the injected current in the circuit and $W$ is the current through the inductance $L$. The function $F(V)$ that describes the behavior of the tunnel diode was modeled by Nagumo with a cubic curve. This approximation and an appropriate change of variables reduces the Eqs. (1.31) to the Eqs. (1.22) of the FitzHugh-Nagumo model.

Other circuits were also proposed to reproduce electronically the behavior of the FitzHugh-Nagumo model. One of the most intuitive ones was designed by Lancaster and Helen [14] using voltage multipliers integrated circuits to create the cubic non-linearity required by the model. Lancaster and Helen also contributed with an electronic circuit design that, although does not relate to the FitzHugh-Nagumo equations, presents an excitable behavior as expected from a neuron membrane. From measurements on the circuit shown in Fig. 1.15a they derived

the following set of equations:

$$\begin{aligned} C\dot{V} &= \frac{5-V}{R_{fast}(V)} + \frac{5-V}{R_s} - \frac{V}{100} - \frac{V-V_b}{R_{sl}} - I_C(V,V_b) \\ C_{sl}\dot{V}_b &= \frac{V-V_b}{R_{sl}} - I_B, \end{aligned} \tag{1.32}$$

where $I_c$ and $I_B$ are the currents in the collector and emitter terminals of the npn transistor and $R_{fast}$ is a resistance with value depending on the voltage $V$ at the capacitor $C$. This resistance is determined by the dynamics of the region delimited by the dashed line in Fig. 1.15a. The currents on the transistor terminals are calculated be the Ebers-Moll model [15]. Figure 1.15b shows a numerical simulation of the circuit phase space. The nullclines of the variables $V$ e $V_b$ as well as the trajectory of the system during a spike. Figure 1.15 shows an experimental spike train (dashed line) and the data from the numerical simulation of the Eqs. (1.32) (solid line).

Electronic circuit models can also be made to reproduce with great precision most of the biological characteristics of neuron. One such circuit with strong physiological basis was proposed by Mahowald and Douglas [16] with the aim of mimicking the pyramidal neurons of the neocortical region of the brain. The so caller silicon neuron is able to emulate the ionic currents that generate electrical membrane activity.

Some of the electronic circuit designed to reproduce neuron-like behavior were thought aiming dynamic interaction with biological neurons rather than stimulating them using response independent current commands. In this way, electronic circuits which analogically integrated the Hindmarsh and Rose equations [17] were coupled to the neurons of a preparation of lobster pyloric CPG neurons. This allowed to show that regularity could emerge as a collective dynamical property of units which individually presented complex dynamics. In another set of experiments, electronic neurons interacting with a biological preparation were used to unveil which dynamical properties of a neuron network depend on the bifurcation leading to excitation for the units, rather than on the details of the neuronal dynamics. To carry out this program, a standard form for type-I excitable dynamics [13], where there is a clear threshold for excitation rather than just a separatrix region as presented by both Hodgkin-Huxley and FitzHugh-Nagumo models, was analogically integrated with a circuit, which was used to replace a neuron in a midbody ganglion of the leech Hirudo medicinalis [18]. The responses under the stimulation of both the natural preparation and the one with a replaced neuron were found to be similar. Beyond the possibility of interacting with neurons through a dynamically sensible way, these efforts provide empirical support to the program of studying neuronal processes through simple and relatively low dimensional dynamical systems. Depending on the question under study, it might be desirable to be able to establish a closer link between the device and a neuron. In this spirit, a device implementing a conductance model was recently proposed [19].

These circuits, however, have two limitations for our purposes. First, they are still too complex to be replicated in large scale. Second, they do not have a controllable noise source to produce stochastic spike trains, a feature that is common to the both models [20] and real neurons [1, 21, 22]. The present work is a first step in this direction. We propose an excitable

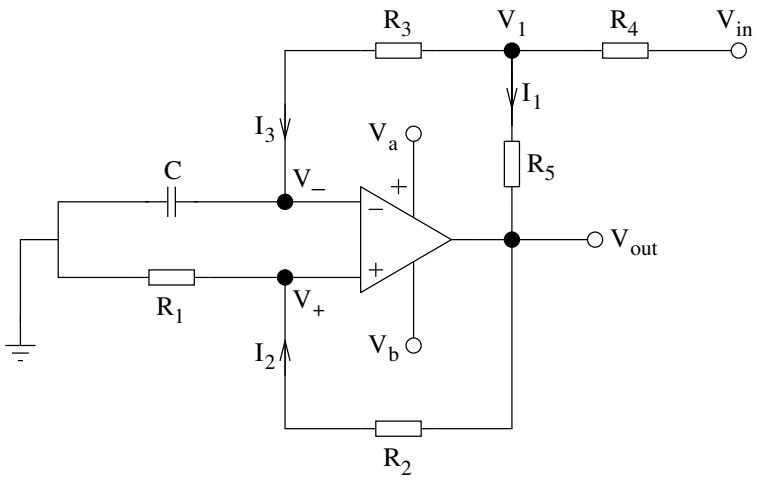


**Figure 1.16** Electronic Excitable Circuit. $V_a$ and $V_b = -V_a$ are the operational amplifier supply voltages, $V_{in}$ is the input voltage corresponding to any combination of external stimuli. The circuit is mathematically described as two-dimensional dynamic system on the variables $V_-$ and $V_{out}$ (see Eq. (1.39)).

electronic circuit which can serve as a building block of an electronic sensor. The advantages of its extreme simplicity are twofold: it allows for scalability and, at the same time, simple mathematical modeling.

## 1.6 A simple electronic neuron model

Here we present our own model of an electronic sensory neuron [23]. Since this is the object of our study throughout most of this work, the description of the characteristics of this circuit is more detailed than that presented previously for other electronic neuron models. Our aim with the circuit shown in Fig. 1.16 was to create a design simple enough to be easily reproduced and to have a straightforward mathematical modeling. These two characteristics allow for scalability, i.e. the circuit model can be used as building block for the construction of large networks. The circuit consists only of a few resistors, a capacitor and an operational amplifier. The input voltage $V_{in}$ corresponds to any sort of external stimuli arriving at the neuron (i.e. a combination of excitatory and inhibitory post-synaptic potentials, a constant stimulus resulting from a DC voltage or noise). The voltages $V_a$ and $V_b$ are the external energy supply for the operational amplifier, which, as per usual in applications involving operational amplifiers, were made symmetric ($V_b = -V_a$), while $V_-$ and $V_+$ are, respectively, the voltages of the inverter and non-inverter terminals of the amplifier.

The mathematical modeling of the circuits is based on the dynamic of the operational am-

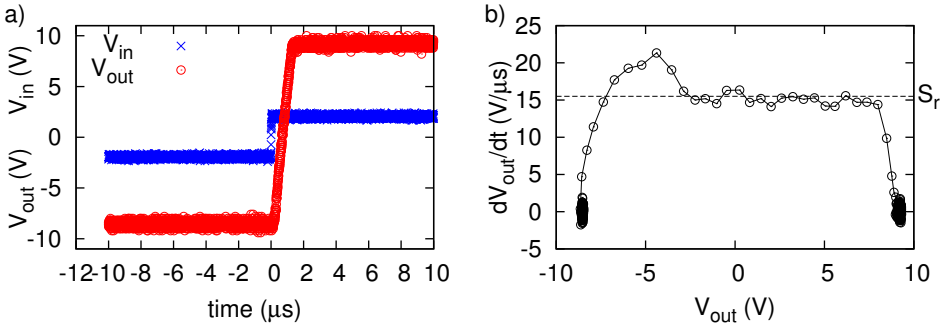


**Figure 1.17** Experimental measure of a comparator circuit response. a) The difference between the non-inverter and inverter terminal is $V_+ - V_-$ (blue crosses) and the output voltage is $V_{out}$ (red dots). b) The time derivative of the output voltage $dV_{out}/dt$ as a function of $V_{out}$. The horizontal solid line shows the value of the slew rate $S_r$.

plifier, which in this cases behaves as a comparator circuit[1]:

$$\begin{cases} V_{out} = V_a, \text{ if } V_+ > V_- \\ V_{out} = V_b, \text{ if } V_+ < V_- \ . \end{cases} \tag{1.33}$$

Equation (1.33), however, does not account for the finite time it takes for the operational amplifier to change between the two voltages $V_a$ and $V_b$. This time depends on the amplifier and it is related to the slew rate $S_r$, which can be easily measured from a pure comparator circuit (see Fig. A.1 in Appendix A). Figure 1.17A shows the response $V_{out}$ of such circuit when the difference between the two terminal voltages $V_-$ and $V_+$ is controlled.

The slew rate $S_r$ corresponds to the rate of change of the output voltage $V_{out}$. In Fig. 1.17B we show how this rate varies as $V_{out}$ changes and how to obtain the value of $S_r$ from the graph. For most operational amplifiers, the slew rate is measured by the manufacturer and its value is given in the product datasheet. The amplifiers used in the circuits throughout this work (TL071 and TL074) have a mean slew rate $S$ of 16 V/$\mu$s.

Below, we propose a model for comparator circuits that includes the effect of the slew rate $S_r$ on its temporal dynamics:

$$\frac{dV_{out}}{dt} = S_r \,\text{sign}\left[V_b - V_{out} + (V_a - V_b)\Theta(V_+ - V_-)\right], \tag{1.34}$$

where $\Theta$ is the Heaviside function. The function $\text{sign}(x)$ returns the sign of its argument $x$ or zero if the argument is also zero:

$$\text{sign}(x) = \begin{cases} 1, & \text{if } x > 0 \\ -1, & \text{if } x < 0 \\ 0, & \text{if } x = 0, \end{cases} \tag{1.35}$$

[1] see Appendix A for more details on comparator circuits and other basic operational amplifier circuits that appear on this work.

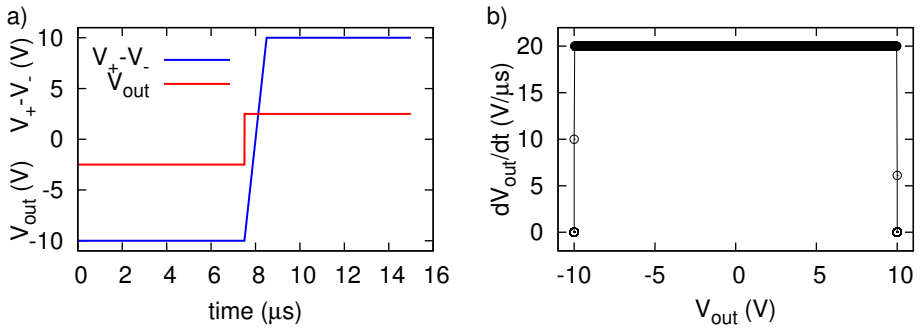


**Figure 1.18** Comparator model response. A) The difference between the non-inverter and inverter terminal is $V_+ - V_-$ (blue crosses) and the output voltage is $V_{out}$ (red dots). B) The time derivative of the output voltage $dV_{out}/dt$ as a function of $V_{out}$.

Integrating Eq. (1.34) when the difference between the two terminal voltages $V_+ - V_-$ is controlled in the same as showed in Fig. 1.17A leads to same response observed experimentally from the comparator circuit. The results are shown in Fig. 1.18.

Having defined the temporal dynamics for the output voltage $V_{out}$, we go back to the mathematical description of the excitable electronic circuit presented in Fig. 1.16. Applying Kirchoff laws we can show that:

$$V_+ = \alpha V_{out} \tag{1.36a}$$
$$V_1 = \beta V_{out} + \gamma V_{in}, \tag{1.36b}$$

where

$$\alpha \equiv \frac{R_1}{R_1 + R_2} \tag{1.37a}$$
$$\beta \equiv \frac{R_4}{R_4 + R_5} \tag{1.37b}$$
$$\gamma \equiv \frac{R_5}{R_4 + R_5}. \tag{1.37c}$$

To obtain Eq. 1.36b we assume that $R_3 \gg R_4, R_5$, therefore rendering the current $I_3 \simeq 0$. Computing the current at the capacitor C gives:

$$\frac{dV_-}{dt} = \frac{V_1 - V_-}{R_3 C}. \tag{1.38}$$

Applying Eq. 1.36a to Eq. (1.34) and Eq. 1.36b to Eq. 1.38, we obtain a two-dimensional dynamical system in the variables $V_{out}$ and $V_-$:

$$\begin{aligned} \frac{dV_{out}}{dt} &= \frac{V_c}{\varepsilon}\text{sign}(V_b - V_{out} + (V_a - V_b)\Theta(\alpha V_{out} - V_-)) \\ \frac{dV_-}{dt} &= \frac{1}{R_3 C}[\beta V_{out} + \gamma V_{in} - V_-], \end{aligned} \tag{1.39}$$

where $V_c$ is a characteristic voltage of the same order of magnitude of the supply voltages $V_a$ and $V_b$ and we have defined $\varepsilon = V_c/S_r$ as a characteristic (short) time scale when compared with the characteristic charge and discharge time $R_3C$ of the capacitor $C$. Throughout the remainder of this work, unless otherwise stated, $V_a = -V_b = 12$ V and $V_c$ was chosen to be equal to 10 V.

For purposes of mathematical analysis and numerical simulation of the system presented in Eq. (1.39) we employ a change to the following dimensionless variables:

$$v \equiv \frac{V_{out}}{V_c}, \tag{1.40a}$$

$$w \equiv \frac{V_-}{V_c}, \tag{1.40b}$$

leading to the new dimensionless system that describes the excitable circuit:

$$\dot{v} = \text{sign}\left(b - v + \frac{(a-b)}{1+e^{-(\alpha v - w)/x_0}}\right), \tag{1.41a}$$

$$\dot{w} = \phi\left[\beta v + \gamma j - w\right], \tag{1.41b}$$

where we defined the dimensionless groups:

$$\tau \equiv \frac{t}{\varepsilon}\ ;\ a = \frac{V_a}{V_c}\ ;\ b = \frac{V_b}{V_c}\ ;\ \phi = \frac{\varepsilon}{R_3C}\ ;\ j = \frac{V_{in}}{V_c}, \tag{1.42}$$

and replaced $\Theta$ by the continuous function

$$\tilde{\Theta}(x;x_0) = \frac{1}{1+e^{-x/x_0}}. \tag{1.43}$$

The $\dot{()}$ over the variables $v$ and $w$ means a derivative with respect to the dimensionless time $\tau$. Note that $\tilde{\Theta} \to \Theta$ as $x_0 \to 0$. The constant $\phi \ll 1$ sets the ratio between the fast and slow time scale as in the FitzHugh-Nagumo model, so that $R_3C$ ultimately controls the overall time scale of the problem.

The nullclines of the system are obtained by making $\dot{v} = 0$ and $\dot{w} = 0$. From Eq. (1.41a) we can easily verify that $\dot{v} = 0$ implies:

$$w = x_0 \ln\left(\frac{a-v}{v-b}\right) + \alpha v, \tag{1.44}$$

while from Eq. (1.41b) it follows that:

$$w = \beta v + \gamma j. \tag{1.45}$$

We can now compare the similarities of our electronic excitable circuit model and the FitzHugh-Nagumo model. In Figure 1.19 the nullclines for our model are shown. The $\dot{v} = 0$ is non-linear, resembling the cubic nullcline in the FitzHugh-Nagumo model while the $\dot{w} = 0$ is linear, in the same way the $\dot{W} = 0$ (Eq. (1.24b)) is in the FitzHugh-Nagumo model. The fixed points of the system are found numerically making Eq. (1.44) and Eq. (1.45) equal. To avoid the possibility that the system has more than one fixed point, it is sufficient that $\beta > \alpha$ as can be inferred from

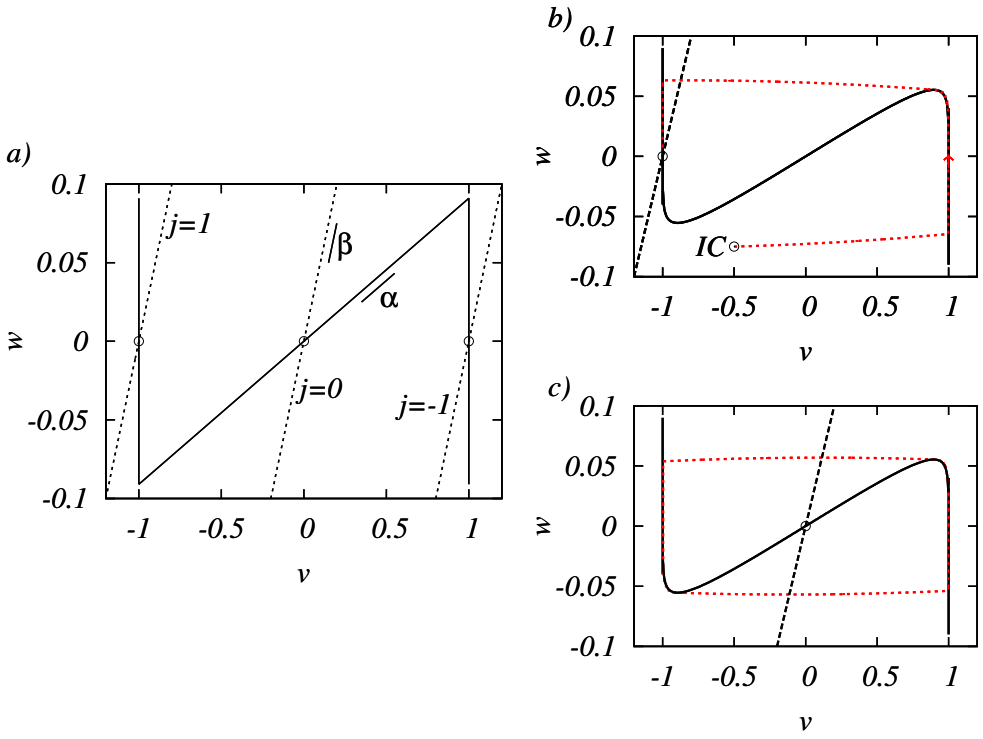


**Figure 1.19** a) Nullclines of the system presented in Eq. (1.41) with parameters $\alpha = 0.0909$, $\beta = 0.5$, $\gamma = 0.5$, $\phi = 0.01$, $a = 1$, and $b = -1$. The dashed lines correspond to the $\dot{w} = 0$ nullcline with different values of $j$ ($V_{in}$). The solid line corresponds to the $\dot{v} = 0$ when $x_0 = 0$. The circles at the nullclines intersections point the position of the single fixed point (for$\beta > \alpha$) for each value of $j$. b) Same as (a) but with $x_0 = 9 \times 10^{-3}$. The red dashed line is a trajectory in phase space starting at the initial condition (IC) $(-0.5, -0.075)$ and $j = 1$. c) Same as (b) but with $j = 0$. In this case the red dashed line is a stable limit cycle and the fixed point is unstable.

Fig. 1.19a. The position of the nullcline $\dot{w} = 0$ changes when the input parameter $j$, which corresponds to the input voltage $V_{in}$, is varied.

Note that when $x_0 \to 0$ the Eq. (1.43) becomes the Heaviside function: the $\dot{v} = 0$ nullcline, then, becomes a piece-wise linear function (as in Fig. 1.19a):

$$\dot{v} = 0 \overset{x_0 \to 0}{\Rightarrow} \begin{cases} v = b & \text{se } \alpha v < w, \\ v = a & \text{se } \alpha v > w, \\ w = \alpha v. \end{cases} \tag{1.46}$$

In Figures 1.19b and c the nullclines were plotted with $x_0 = 9 \times 10^{-3}$. System trajectories in the phase space are shown: a trajectory starting at an arbitrary initial condition and finishing at the stable fixed point (Fig. 1.19a) and a stable limit cycle when the single fixed point is unstable (Fig. 1.19b).

To analyze the stability of the fixed point of the system we linearize the Eqs. (1.41). At first,

we have:

$$\dot{v}' = \frac{\partial \dot{v}}{\partial v}\Big|_{(v^*,w^*)} v' + \frac{\partial \dot{v}}{\partial w}\Big|_{(v^*,w^*)} w' \tag{1.47a}$$

$$\dot{w}' = \frac{\partial \dot{w}}{\partial v}\Big|_{(v^*,w^*)} v' + \frac{\partial \dot{w}}{\partial w}\Big|_{(v^*,w^*)} w', \tag{1.47b}$$

where $v' = v - v^*$ and $w' = w - w^*$. The derivatives in (1.47a) and (1.47b) can be calculated in a more simple way if we avoid the complication of dealing with the function $\text{sign}(x)$ that has no derivative at $x = 0$ and focus only on its argument[2]. This simplification leads to the linearized form of the system in Eqs. (1.41)[3]:

$$\dot{v}' \simeq \left(-1 + \frac{\alpha}{x_0}(a-b)\Theta(1-\Theta)\Big|_{(v^*,w^*)}\right)v' - \left(\frac{1}{x_0}(a-b)\Theta(1-\Theta)\Big|_{(v^*,w^*)}\right)w'$$

$$\dot{w}' = \phi[\beta v' - w'].$$

In the above equations the second order terms were ignored. Note that the second equation is exact since $\dot{w}$ in Eq. (1.41b) is linear in $v$ and $w$. To shorten the notation, we define the function $g \equiv \frac{(a-b)}{x_0}\Theta(1-\Theta)$ which leads to:

$$\begin{cases} \dot{v}' \simeq \left(-1 + \alpha g\Big|_{(v^*,w^*)}\right)v' - g\Big|_{(v^*,w^*)} w' \\ \dot{w}' = \phi\beta v' - \phi w', \end{cases} \tag{1.48}$$

which can be written as $\dot{\vec{x}} = A\vec{x}$, where:

$$\vec{x} = \begin{pmatrix} v' \\ w' \end{pmatrix}$$

and $A$ is the jacobian matrix of the system:

$$A = \begin{pmatrix} -1 + \alpha g\Big|_{(v^*,w^*)} & -g\Big|_{(v^*,w^*)} \\ \phi\beta & \phi \end{pmatrix}. \tag{1.49}$$

From the sign of the real and imaginary parts eigenvalues of the jacobian matrix the stability of the fixed point is determined. As we vary $j$, and therefore change the position where the nullclines meet, we find 4 different kinds of behavior for the fixed point of the system which are depicted in Fig. 1.20: stable node in the region where the both real parts are negative and the imaginary parts are zero; stable spiral when the real parts are negative (and equal for the eigenvalues are complex conjugates) and the imaginary parts are non-zero; unstable spiral when the real parts become positive with non-zero imaginary parts; stable node when the real parts

[2]We could replace $\text{sign}(x)$ for a continuous function with defined derivative in all points in the same way that the $\Theta$ function was replaced: $\text{sign}(x) = \tanh(kx)$ where $k \gg 1$.

[3]Note que $e^{-(\alpha v - w)/x_0} = \frac{1-\Theta}{\Theta}$ when $x_0 \ll 1$.

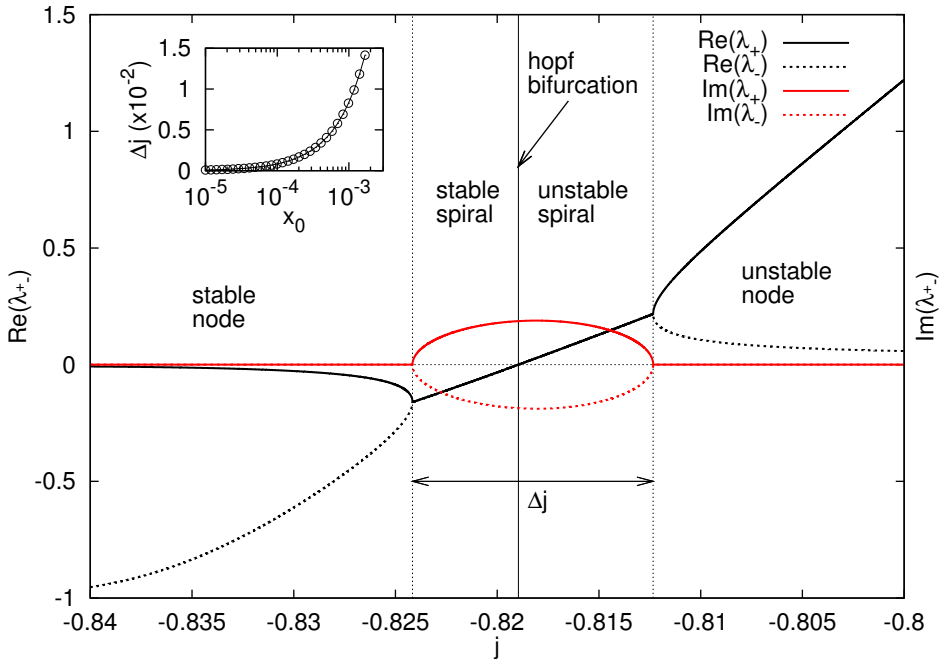


**Figure 1.20** Real (black lines) and imaginary (red lines) of the eigenvalues ($\lambda_+$ e $\lambda_-$) of the jacobian matrix $A$ as a function of the parameter $j$ (corresponding to $V_{in}$ in the circuit) for $\alpha = 0.0909$, $\beta = 0.5$, $\gamma = 0.5$, $a = 1$; $b = -1$, $\phi = 6.3 \times 10^{-4}$ and $x_0 = 1.18 \times 10^{-3}$. The vertical lines separate the regions where the fixed point has different behaviors. Inset: $\Delta j$ as a function of $x_0$.

are positive with zero imaginary parts. When the fixed point sits at the outer branches of the $\dot{v}$ nullcline it is stable and it loses stability when it crosses to its central region.

The parameter $\Delta j$ measures the range of values of $j$ where spirals can be observed. $\Delta j$ increases as $x_0$ increases, and since experimentally $x_0$ is expected to be small ($x_0 \simeq 10^{-5}$ resulting $\Delta j \simeq 10^{-4}$ ($\Delta V_{in} \simeq 1$ mV)), the detection of spiral trajectories is very hard without high precision voltage sources.

The change of stability of the fixed point, when the real parts of the eigenvalues change from negative to positive with non-zero imaginary parts happens via a Hopf bifurcation. A limit cycle becomes the only stable attractor and the trajectories in the region of unstable spirals will tend to it. The trajectories close to the limit cycle follow two time scales: in the "horizontal regions" of the cycle the trajectories are fast and the relevant time scale is $\varepsilon$, which is determined by the slew rate of the operational amplifier; in the "vertical regions" the trajectories are slow the relevant time scale is $R_3C$, the characteristic time of the capacitor. The onset of oscillations in phase space along the limit cycle happens with a discontinuous change in frequency (from zero to a finite non-zero value) as it is characteristic of Hopf bifurcations (Fig 1.21c). Below the Hopf bifurcations the circuit is said to be type-II excitable [13].

There is good quantitative agreement between experimental data from the circuit and the numerical integration, as can be seen in Fig. 1.21b, c, d and e. Note that through an analog

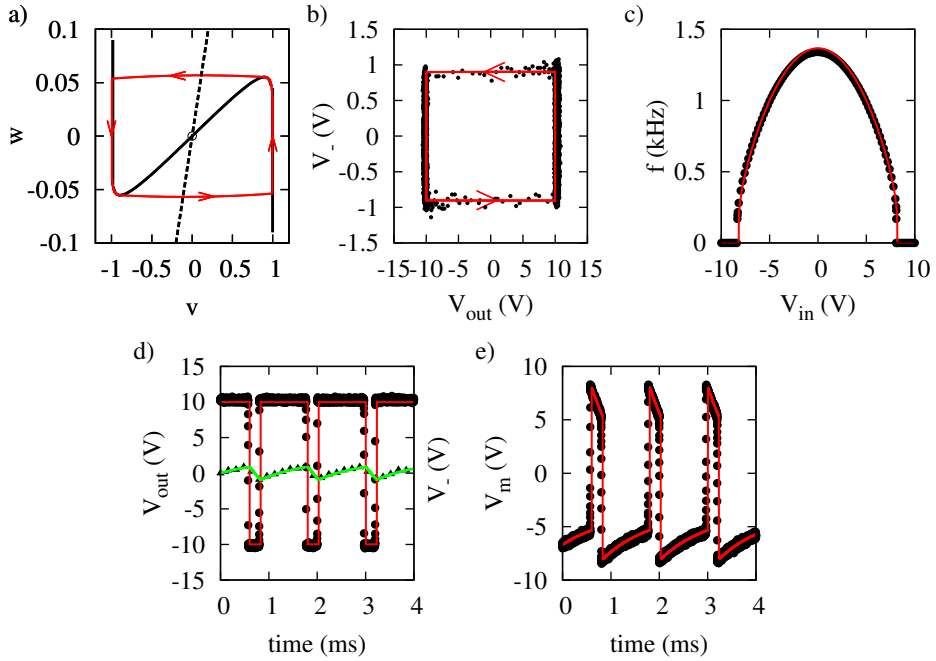


**Figure 1.21** Comparison between experimental data and numerical simulations of the excitable electronic circuit. a) Nullclines of system (1.41) for $a = 1$, $b = 1$, $\alpha = 0.0909$, $\beta = 0.5$, $\gamma = 0.5$, $j = 0$, $\phi = 0.01$ and $x_0 = 9 \times 10^{-3}$: solid black line for the $\dot{v} = 0$ nullcline and dashed black line for the $\dot{w} = 0$ nullcline. The fixed point is unstable and the trajectories are attracted to a limit cycle (red solid line). b) Experimental limit cycle (black dots) and numerical integration of the model (red solid line) for $x_0 = 1 \times 10^{-5}$, $V_a = 10$ V, $V_b = -10$ V, $V_{in} = -6$ V and $\phi = 5 \times 10^{-4}$ (other parameters are the same as in (a)). c) Experimental frequency response $f$ to the external DC stimulus $V_{in}$ (black dots) and the same for the numerical integration of the model (red line). d) Comparison between experimental time series of $V_{out}$ and $V_-$ (black circles and triangles, respectively) with numerical integration of the model (red and green lines, respectively). e) Experimental (black dots) and numerical (red line) spike trains obtained from the analog subtraction $V_m \equiv 1.5V_- - 0.67V_{out}$ of the dynamical variables.

subtraction $V_m \equiv 1.5V_- - 0.67V_{out}$ (see Fig. 1.22b[4]) the circuit exhibits the spikes typical of neuronal membrane potentials (Fig. 1.21e). We emphasize that in Fig. 1.21 experimental and numerical data agree without any fitting parameter, as long as $x_0$ is sufficiently small ($\lesssim 10^{-4}$).

## 1.7 Noise addition

So far we have discussed the response of the excitable circuit under DC stimulation ($V_{in} = V_{DC}$). Biological neurons, however, can show highly variable responses, even when subjected to a presumably constant stimulus. Examples range from highly variable responses olfactory receptor neurons (ORNs) to presentation of identical puffs of odorants [25], to cortical cells stimulated with a constant current via an intracellular electrode [21]. In an attempt to endow

[4]See also Apendix A and B for more information about circuits and values of the electronic components used.

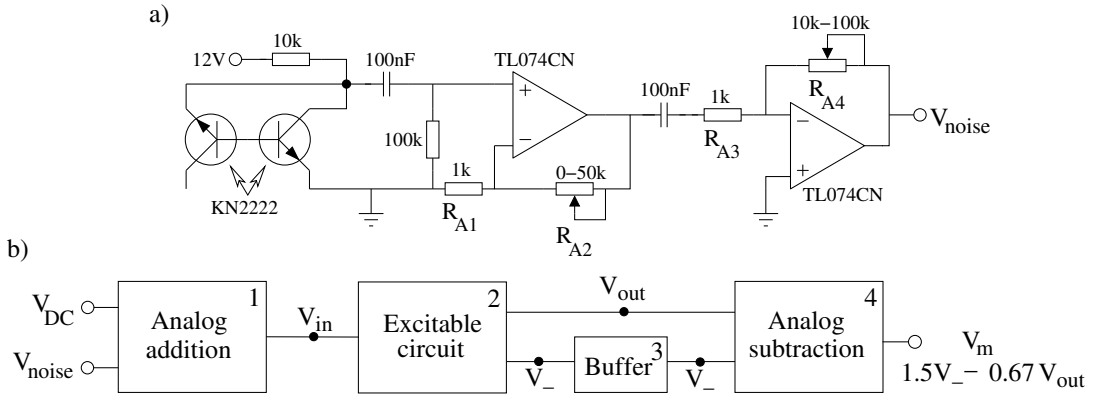


**Figure 1.22** a) An analog noise generator based on the amplification of transistors thermal noise. Noise amplification is given by $A = [(R_{A1} + R_{A2})/R_{A1}](R_{A4}/R_{A3})$. b) Block diagram of the circuit used to verify the excitability of the circuit presented in Fig. 1.16. Analog addition and subtraction are performed with standard TL074 op-amp operations [24].

our excitable circuits with the variability in the spike trains observed in biological neurons, we propose the simple analog noise generator shown in Fig. 1.22a. Once more, its simplicity allows one to attach independent noise generators to each excitable circuit when connecting them in a network.

The circuit in Fig. 1.22a provides a two-stage amplification control via two operational amplifiers to the thermal noise produced by the KN2222 transistors. The total amplification factor $A$ is given by:

$$A = [(R_{A1} + R_{A2})/R_{A1}](R_{A4}/R_{A3}). \tag{1.50}$$

Its output voltage $V_{noise}$, shown in Fig. 1.23a, is approximately a uncorrelated Gaussian white noise voltage with zero mean and a cutoff frequency around 10 kHz, as shown in Fig. 1.23b by its fast Fourier transform.

To obtain variable spike trains, the stimulus $V_{in}$ consists in the analog addition of $V_{DC}$ and $V_{noise}$ (see blocks 1 and 2 in Fig. 1.22b). In the model, this corresponds to replacing Eq. (1.41b) with

$$\dot{w} = \phi\,[\beta v + \gamma j + D\xi(t) - w]\,, \tag{1.51}$$

where $D$ governs the amplitude of the noisy input $\xi(t)$ an it grows linearly with the gain in the noise amplification $A$ (which in turn is controlled by the variable resistors shown in Fig. 1.22). The noise is assumed uncorrelated with zero mean, i.e.:

$$\langle \xi(t) \rangle = 0, \tag{1.52a}$$

$$\langle \xi(t)\xi(t') \rangle = \delta(t - t'). \tag{1.52b}$$

As mentioned in the previous section, to obtain spikes from the circuit it is necessary to perform an analog subtraction of the two dynamic variables $V_{-}$ and $V_{out}$ (block 4 in Fig. 1.22b) but to avoid interference to the voltage $V_{-}$ provided by the capacitor $C$ in the electronic circuit a buffer circuit (a circuit that creates a high impedance copy of the voltage at its input) is employed before the subtraction of $V_{-}$ (block 3).

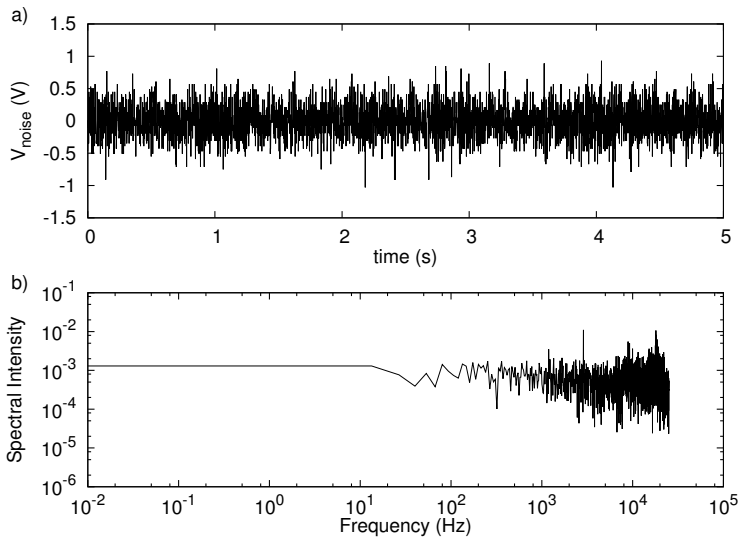


**Figure 1.23** a) Voltage $V_{noise}$ obtained from the noise generator circuit shown in Fig. 1.22a. and (b) its fast Fourier transform.

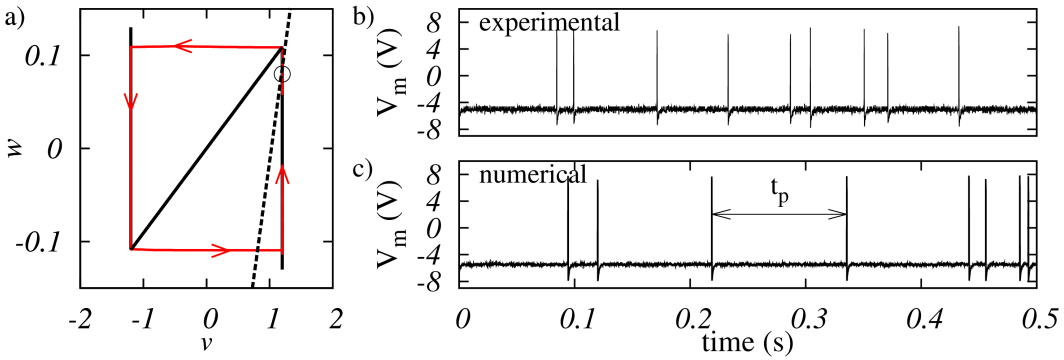


**Figure 1.24** Electronic circuit response when submitted to noise. a) Numerical phase plane trajectory (red line) due to noise excitation. Without noise the system would stay in a resting state at the fixed point (white dot). Experimental (b) and numerical (c) spike train series are shown when the system is in the excitable state (stable fixed point as shown in (a)).

Setting $V_{DC}$ below the Hopf bifurcation, the circuit sits at a stable fixed point at the right branch of the $\dot{v} = 0$ nullcline, from which it eventually departs owing to noise (Fig. 1.24a). This generates spike trains with variable interspike intervals $t_p$ as shown in Fig. 1.24b. Numerical simulations of the circuit when it is subjected to a gaussian white noise input also reproduce this behavior as shown in Fig. 1.24c. In our simulations, addition of noise was implemented with the standard Euler-Maruyama method [26] with a dimensionless time step $\Delta\tau = 0.005$.

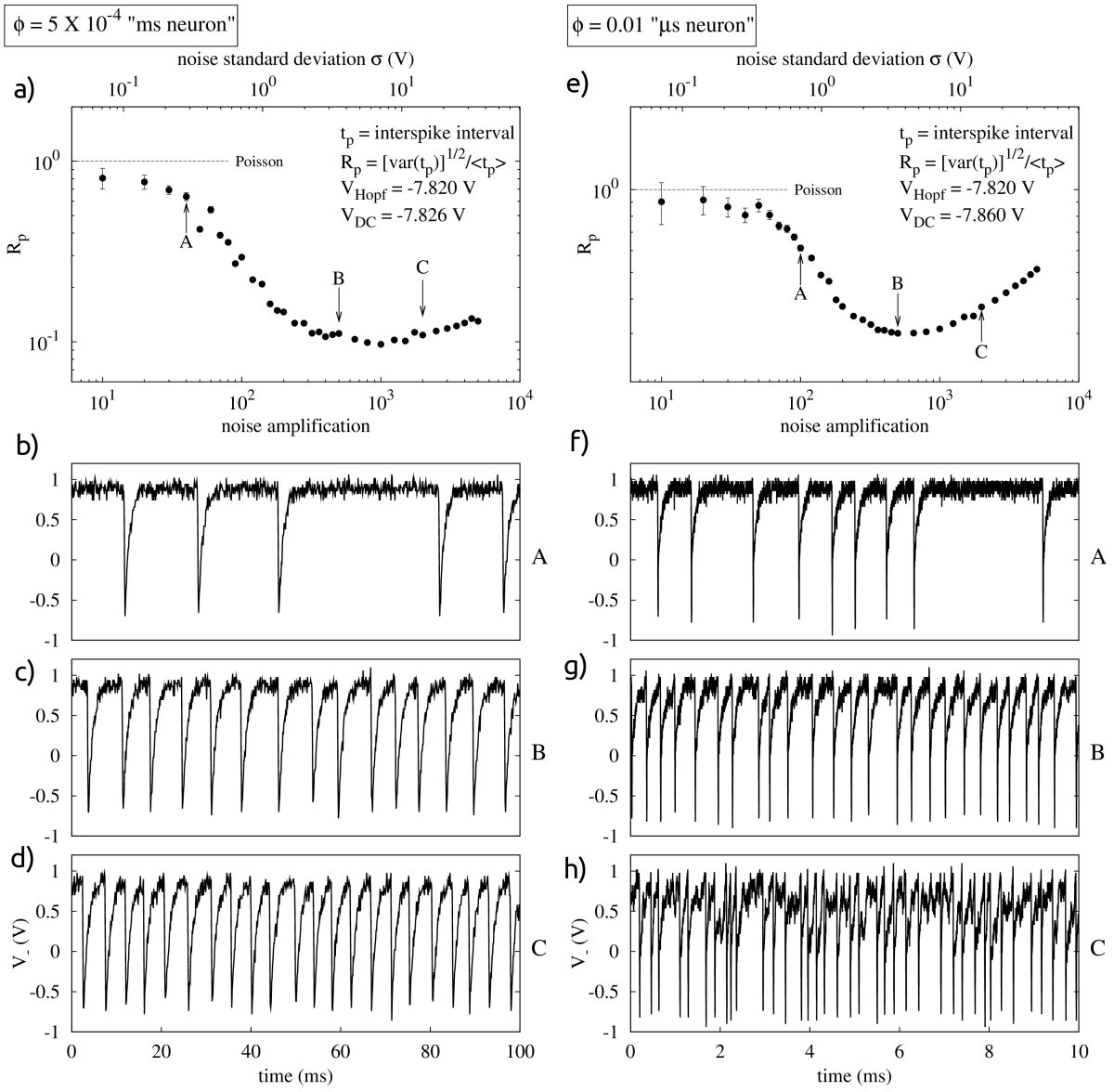


**Figure 1.25** Experimental coherence resonance curve for the electronic circuit. a) $R_p$ as a function of noise amplification (bottom x-axis) and standard noise deviation $\sigma(V)$ (top x-axis). $C = 1$ nF and $V_{DC} = -7.826$ V (see Fig. 1.16). Each point corresponds to a 10 s time series. Three spike train regimes are marked by the arrows A, B and C. b) Time series for the $V_-$ variable corresponding to the A arrow. Small noise amplitude causes low firing rate and low coherence. The interspike intervals distribution resembles that of a poissonian distribution. c) Time series for $V_-$ variable corresponding to the B arrow. Moderate noise amplitude leads the system to optimum coherence. d) Time series for $V_-$ variable corresponding to the C arrow. Large noise amplitudes causes high firing rate and low coherence. Figures (e), (f), (g) and (h) are similar to (a), (b), (c), and (d), but with $C = 50$ pF and $V_{DC} = -7.86$ V.

## 1.8 Coherence resonance

We now show that the interplay between noise and excitability behaves as expected in our simple circuits. Pikovsky and Kurths [27] have shown that the coherence spike trains caused by uncorrelated white gaussian noise with zero mean of a FitzHugh-Nagumo model neuron in an excitable regime peaks at an intermediate noise value. This means that for small and large noise amplitude the interspike interval $t_p$ in those spike trains is rather irregular, while for moderate noise intensities coherent (regular) oscillations are observed. This phenomenon is called "coherence resonance". The coherence (or incoherence) of a spike train can be measured by the normalized standard deviation of the interspike intervals:

$$R_p \equiv \frac{\sqrt{\langle t_p^2 \rangle - \langle t_p \rangle^2}}{\langle t_p \rangle}. \tag{1.53}$$

The parameter $R_p$ has value zero if the spike train is perfectly periodic and it tend to the value 1 as the interspike distribution becomes closer to a poissonian distribution. This parameter should have a minimum as a function of the noise intensity applied to the system.

Figure 1.25a shows this exact behavior when our electronic neuron is in the excitable regime and receives a noisy input (as shown in Fig. 1.24) with a controllable amplitude. The onset of the Hopf bifurcation happens at $V_{Hofp} = -7.82$ V and the input voltage is set slightly below that value $V_{DC} = -7.826$ V. It can be seen that for slow noise intensities (arrow A) the system approaches $R_p = 1$. The time series corresponding to that regime is shown in Fig. 1.25b. In this case the dynamical variable $V_{-}$, the counterpart to the dimensionless variable $w$, was chosen to demonstrate the time series since it is the one directly affected by the noise and each of its minimums corresponds to spike. This choice was also made in the original work of Pikovsky and Kurths. Regularity of the time series is attained at an intermediate noise value (arrow B) near the minimum of $R_p$ (time series shown in Fig. 1.25c). Further increasing the noise intensity cause the spike train to lose coherence (arrow C, time series in Fig. 1.25d). This set of measurements was made when the electronic circuit capacitor had the value $C = 1$ nF. This set the ratio between the time scales of the fast ($V_{out}$ or $v$) and slow ($V_{-}$ or $w$) variables at $\phi = 5 \times 10^{-4}$ meaning that the characteristic charge time $R_3C = 1$ ms is much slower then the time scale set by the slew rate of operational amplifier $\varepsilon$. Since the spike duration and refractory period is determined by the capacitor $C$, this electronic circuit is called a "millisecond neuron". Another set of measurement was made with a faster capacitor ($C = 50$ pF, same voltage value for the Hopf bifurcation and $V_{DC} = -7.86$ V). The results shown in Fig. 1.25e, f,g and h are similar regarding the presence of a coherence minimum. Nonetheless, due to the faster response of the circuit to noise oscillations, coherence is not as strong as in the previous case (the minimum in the first case is closer to zero than in the second case). The fast response also allows the phenomenon to occur even when the DC voltage is not as close $V_{Hopf}$. In this case the rate between the time scales of the fast and slow variables is $\phi = 0.01$ and the excitable circuit is called "microsecond neuron".

For small noise amplitudes ($V_{noise} \sim 50$ mV, or $A \sim \mathcal{O}(1)$ in Fig. 1.25a and e), spikes are sparse and $R_p$ approaches unity. This suggests a Poisson process in which the interspike interval

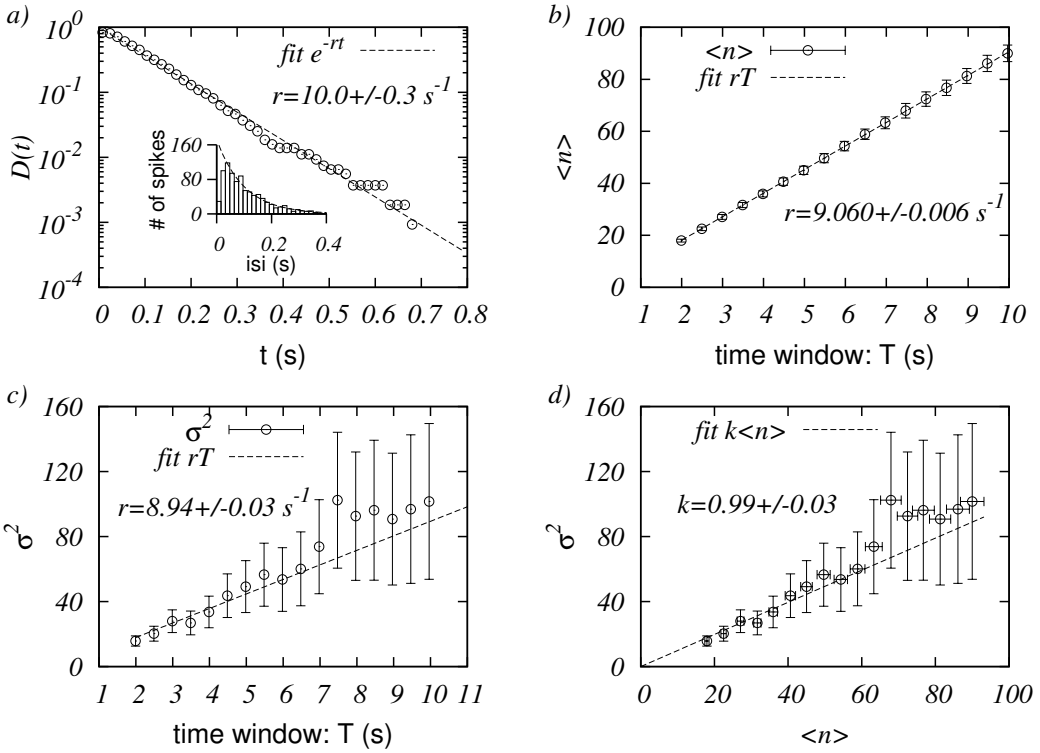


**Figure 1.26** Spike train statistics of a 100 s duration series from the circuit of Fig. 1.22b. a) Interspike interval (isi) accumulated distribution in log-linear scale. Inset: corresponding histogram of isi. The dashed line corresponds to an exponential fit of a Poisson distribution with mean firing rate $r = 10.0(3)$ $s^{-1}$. The deviation from the Poisson distribution for small isi is due to the refractoriness of the excitable circuit. In the following graphs we have divided the series in time windows of duration $T$. The mean number of spikes $\langle n \rangle$ (b) and the variance $\sigma^2$ (c) are shown as functions of $T$. In (d) we have $\sigma^2$ as a function of $\langle n \rangle$. The dashed lines are fits of $\sigma^2 = \langle n \rangle = rT$ according to the Poisson distribution.

distribution approaches an exponential

$$P(t_p) = re^{-rt_p}, \tag{1.54}$$

where $r$ is time rate constant. This Poisson limit is interesting because it is observed in different neuronal preparations [1, 22], so we performed a detailed statistical analysis of the small $V_{noise}$ regime.

In Fig. 1.26a the statistics of a 100 s experimental time series was compared to the accumulated distribution

$$D(t) \equiv \int_t^\infty re^{-rt_p} dt_p = e^{-rt}, \tag{1.55}$$

showing good agreement for a fitted rate $r \simeq 10.0(3)$ $s^{-1}$. To check for consistency, we divided the time series in small time windows of size $T$ and sampled the number $n$ of of spikes per window. In a Poisson process one has the linear relationships $\langle n \rangle = rT$, $\sigma_n^2 \equiv \langle n^2 \rangle - \langle n \rangle^2 = rT$ which are confirmed in Fig. 1.26b and c. The unit slope in the $\sigma_n^2$ versus $\langle n \rangle$ plot is also verified

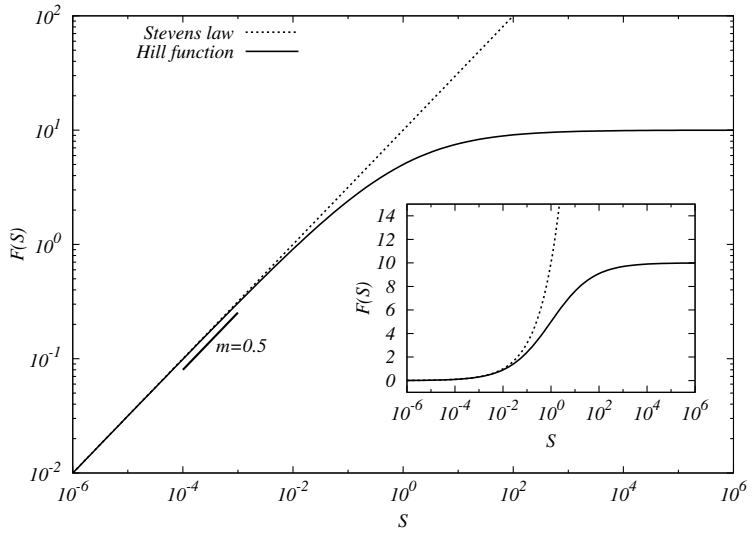


**Figure 1.27** Comparison between the Stevens' Law $F(S) = CS^m$ and the Hill function $F(S) = F_{max}S^m/(S^m + S_0^m)$, with parameters $m = 0.5$, $C = 10$, $F_{max} = 10$ e $S_0 = 1$ in logarithmic scale. The inset shows the same functions in a log-linear scale.

(see Fig. 1.26d). These results show that our circuit can be used to mimic not only deterministic dynamics, but also simple statistical properties which appear in biological neurons.

## 1.9 The dynamic range problem

The human sensibility to external stimuli is subject to study since the nineteenth century. The Psychology field that studies the perception of subjects to physical stimuli such as heat, brightness, pressure and others is called Psychophysics. Ernst Heinrich Weber was one of the first to study the human response to physcal stimuli in a quantitative way. Later, Gustav Theodor Fechner worked on a theory based on the finding of Weber, resulting in the Weber-Fechner law. Their results suggest that the psychophysical response $F$ is a logarithmic function of the external stimulus $S$: $F(S) = C\log(S)$. By the 1960's the psychophysicist Stanley Smith Stevens [28] published a series of psychophysical data suggesting that the relationship between the response and the stimulus is a power law: $F(S) = CS^m$, which is known as Stevens' law. Other functions were proposed to adjust data with a greater range of stimulus intensities, taking into account the saturation in the perceived response, in particular the Hill function $F(S) = F_{max}S^m/(S^m + S_0^m)$ where $F_{max}$ is the saturation response and $S_0$ is the value of the stimulus corresponding to $F_{max}/2$. Figure 1.26 shows a comparison between the Stevens' Law and the Hill function. In the region of low intensity stimuli, they coincide.

In general, psychophysical laws show that subjects perceive with great distinction stimuli of different orders of magnitude. Recent studies [29] suggest that the ability to respond differently to a large range of stimulus intensities or, in other words, large dynamic range, arises as a collective phenomena of excitable elements with small dynamic range connected in a network. The appeal of such systems goes beyond basic research in neuroscience. The idea could be

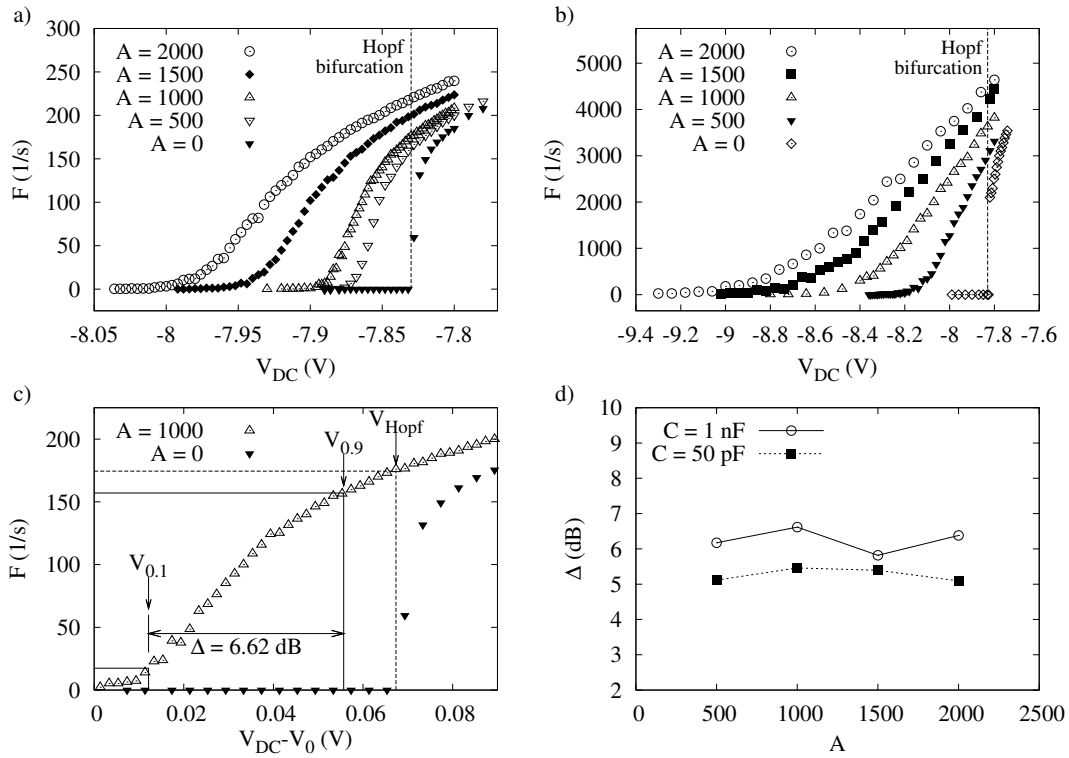


**Figure 1.28** Experimental response curves $F(V_{DC})$ measured at different values of the noise amplification $A$. a) $C = 1$ nF ($\phi = 5 \times 10^{-4}$ and $T_m = 10$ s). b) $C = 50$ pF ($\phi = 0.01$ and $T_m = 0.2$ s). c) Response curve for $C = 1$ nF (A=1000), and relevant parameter for calculating the dynamic range. d) Dynamic range as function of noise amplification for $C = 50$ pF (black squares) and $C = 1$ nF (white circles).

reversed, leading to biologically inspired artificial sensors, which have been used in a variety of scenarios (see e.g. [30]).

In this section we study the response of our electronic excitable system to varying input voltage $V_{DC}$, considering the noise amplitude $V_{noise}$ constant. Although in real neurons the background noise may have a dependence on the stimulus, it is a fair approximation to treat the noise amplitude as constant and focus on the dependence on input signal as a control parameter of the dynamics. In what follows, the response of the circuit is defined as the mean firing rate $F$ measured over a fixed time interval $T_m$. This so-called "rate coding" is also a longstanding approximation [31], which seems to fit data in several cases [11, 32].

For fixed $T_m$ and noise amplification $A$, the response $F$ of our circuit is an increasing function of the stimulus $V_{DC}$ because larger values of $V_{DC}$ amounts to increased excitability, lowering the "effective threshold" to noise-induced spike generation (as mentioned before, there is no real threshold in type-II excitable neurons [12]). Conversely, for fixed $V_{DC}$, the response $F$ also increases with increasing noise intensity $A$. These results are shown in Fig. 1.28a, where we plot (for different noise intensities) the responses $F(V_{DC})$ of our excitable circuit with a 1 nF capacitor. This choice sets the time scale of the neuron in the millisecond range (i.e. that of biological neurons). Note that in the absence of noise ($A = 0$) the response is null up to the Hopf bifurcation (so the lowest curve in Fig. 1.28a is similar to Fig. 1.21c). Results in Fig. 1.28b

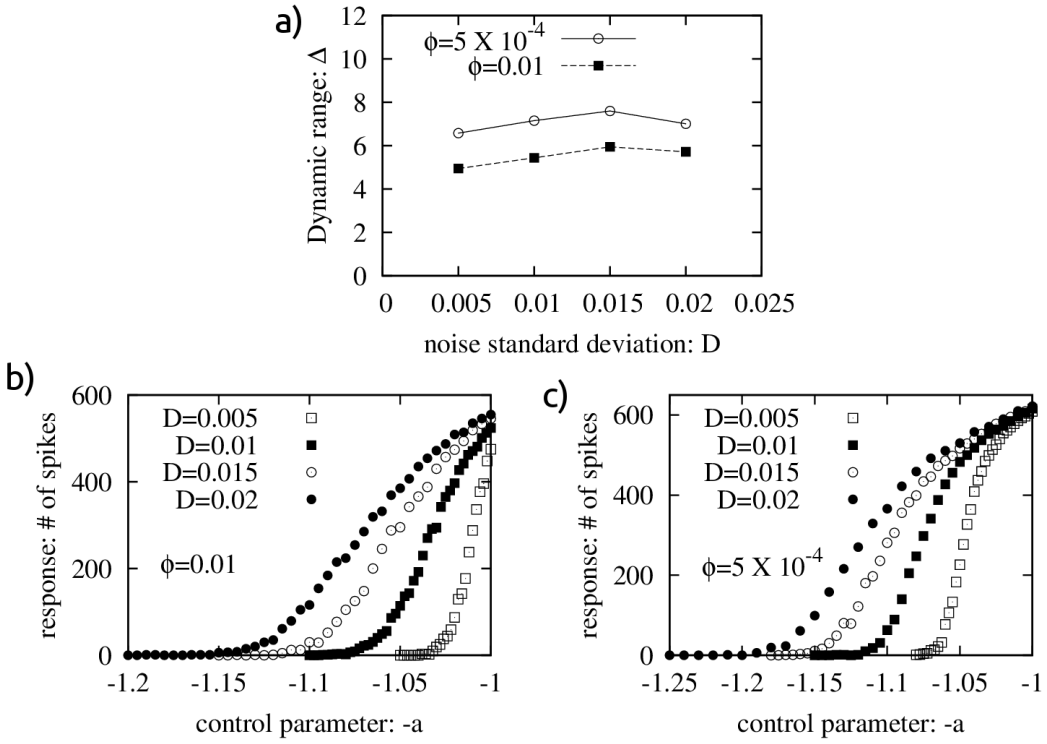


**Figure 1.29** Numerical response curves measured at different values of the noise amplification $D$. a) Dynamic range as function of $D$ for both values of $\phi$. b) Response of the FitzHugh-Nagumo model with $\phi = 0.01$ and c) when $\phi = 5 \times 10^{-4}$. The response is measured counting the number of spikes in a time series of 2000 time units.

correspond to a circuit with a 50 pF capacitor. This single change renders a much faster circuit, now operating in the microsecond range, but with its dynamical features otherwise preserved. This has potential applications, because a faster circuit requires shorter measurement intervals $T_m$ (=0.2 s in our example) for a reliable estimation of the firing rate.

Given a response curve, we can calculate its dynamic range, which roughly speaking corresponds to the range of stimulus intensity that the firing rate can "appropriately code". Measured in decibels, this is arbitrarily defined as [25, 33]

$$\Delta \equiv 10 \log_{10} \left( \frac{V^*_{0.9}}{V^*_{0.1}} \right), \tag{1.56}$$

where $V^*_x \equiv V_x - V_0$ is measured relative to the voltage $V_0$ at which the response becomes non-zero, which we arbitrarily defined to happen when $F = 0.01 F_{max}$, and

$$F(V_x) = x F_{max} \qquad (0 \leq x \leq 1)\,, \tag{1.57}$$

where $F_{max}$ is the firing rate at the Hopf bifurcation. In words (see Fig. 1.28c), $\Delta$ measures the range of stimulus $V_{DC}$ which are neither too small ($V_{DC} < V_{0.1}$) to go undetected nor too close ($V_{DC} > V_{0.9}$) to the autonomous oscillations that emerge at $V_{Hopf}$.

As shown in Fig. 1.28d, the dynamic range is a rather robust feature of our excitable circuit: it changes little as the noise intensity is varied, regardless of the time scale at which it operates. In both cases, $\Delta \simeq 6$ dB, which is closer to the values obtained experimentally ($\Delta \simeq 10$ dB for olfactory sensory neurons [25], $\Delta \simeq 14$ dB for retinal ganglion cells [34, 35]) than results obtained theoretically for discrete models of excitable elements ($\Delta \simeq 14$ dB in [35] and $\Delta \simeq 19$ dB in [36]).

Numerical simulations of the above results were made using a slightly different version of the FitzHugh-Nagumo model presented before. This version allows for easier integration of the equations when noise is present:

$$\phi \frac{dv}{dt} = v - \frac{v^3}{3} - w\,, \tag{1.58a}$$

$$\frac{dw}{dt} = v - \zeta + D\xi(t). \tag{1.58b}$$

The parameter $\zeta = -1.05$ ensures that the model is in a excitable regime, since the Hopf bifurcation occurs for $\zeta = -1.0$. The results of the simulations are shown in Fig. 1.29 and reproduces well the behavior of our electronic circuit for two values of ratio $\phi$ between the time scale of the two dynamical variables.

CHAPTER 2

# Electronic Synapse

In this chapter we tackle the mechanisms that allow neurons to connect and transmit electric signals between each other. In the last chapter we discussed, from a physiological point of view, how electric signals propagate within the neuron, in particular we focused on the description of action potential generation within an axon. Synapses are the point at which communication between neurons happens and they are fundamental for many biological process such as perception and learning. The term synapse was introduced at the beginning of the nineteenth century by the neurophysiologist Charles Sherrington although the region had first been described histologically (at the level of light microscopy) by Ramón y Cajal.

With the aim of constructing an excitable medium by connecting electronic neurons each with small dynamic range, we developed a model of electronic synapse inspired in their biological counterparts. Here we are going to present a brief physiological description of synapses followed by mathematical models and efforts to create electronic connections that mimic synapses. Finally we will describe our model of electronic synapse that share the same characteristics of our electronic neuron: it is simple, allowing it to be reproduced in scale and it has an straightforward mathematical characterization.

## 2.1 Review of basic synapse physiology

Synapses connect two cells that are involved in the transmission and reception of electrical signals. This connection can be between two nerve cells or between a nerve cell and a muscular cell. Synapses also come in two flavors: they are either electrical or chemical. This fact was only verified after a considerable amount of debate from the community when better physiological techniques were employed around the 1950's and 60's.

### 2.1.1 Electrical synapses

In electrical synapses the two cells interact through a specialized contact region known as gap junction channel. For this reason this kind of synapses are also called gap junction synapses. These channels are protein structures that physically connects the cytoplasms of both cells and provide a low resistance (high conductance) pathway for transmission of electric signals. At the point of contact, the two cells are separated by distances around 4 nm, which is much closer than the usual separation between neurons (20 nm). The junction consists of pair of hemichannels, one in each cell, called connexons. A connexon is made of six identical protein subunits called connexin. In Figure 2.1a we show a schematic representation of a gap

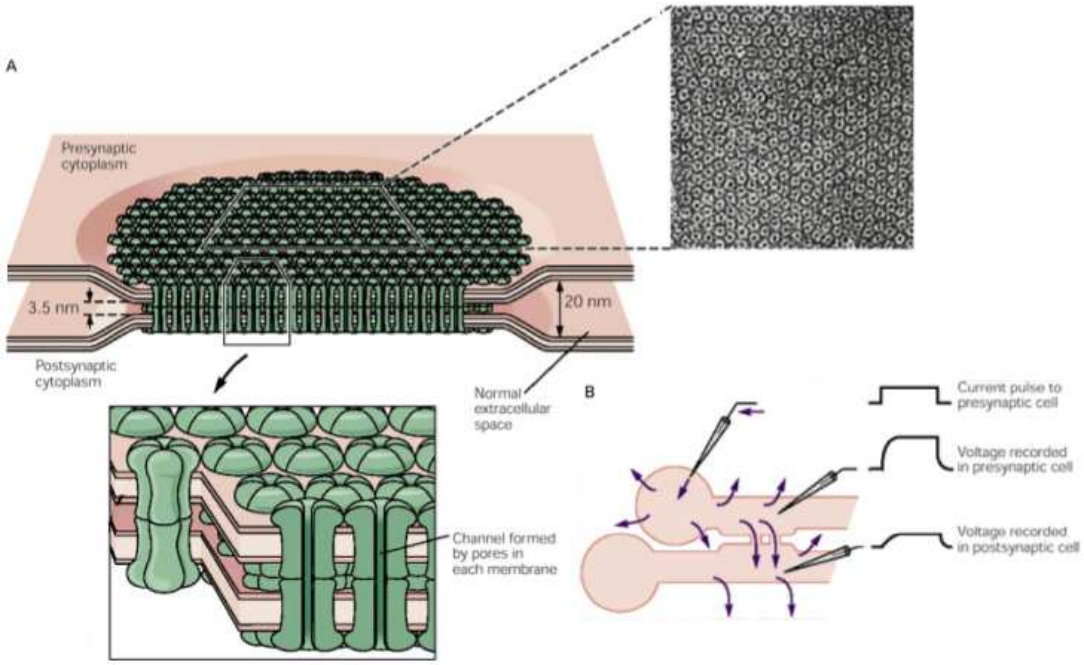


**Figure 2.1** A) Schematic representation of electrical synapses showing the connexons and connexins composing the gap junctions. B) Electric signal transmission by an electrical synapse suffers attenuation from the membrane resistance of both pre and post-synaptic cells. (Adapted from Kandel (2000) [2]).

junction synapse.

The transmission of electric signals from one neuron, the pre-synaptic neuron, to another, the post-synaptic neuron, in electrical synapses happens with little delay, i.e. the transmission is almost instantaneous due to the direct connection between the membranes. Since the transmission is mediated by the passive electrical properties of the ion channels, this comes at the cost of attenuated post-synaptic response caused by the membrane resistance in both pre and post-synaptic cells (Fig. 2.1b). The fast transmission, however, allows for easy synchronization between groups of neurons connected with electrical synapses, which is important in biological mechanisms that require fast responses, such as a defensive reflex. The electrical synapses usually admit signal transmission in both ways, so that changes in the membrane potential in any of the two neurons connected by a gap junction are transmitted to the other cell, with an ionic current proportional to difference between the two membrane potentials. In this sense, gap junctions admits both depolarizing and hyperpolarizing potentials to be transmitted with no distinction. This kind of transmission is similar to the passive propagation of subthreshold electric signals along axons. There are, however, electrical synapses that rectify, i.e. the current flows preferably in one direction.

### 2.1.2 Chemical synapses

The mechanism involving electrical signaling through chemical synapses differs greatly from electrical ones. First of all, there is no physical continuity of the cytoplasms of pre-

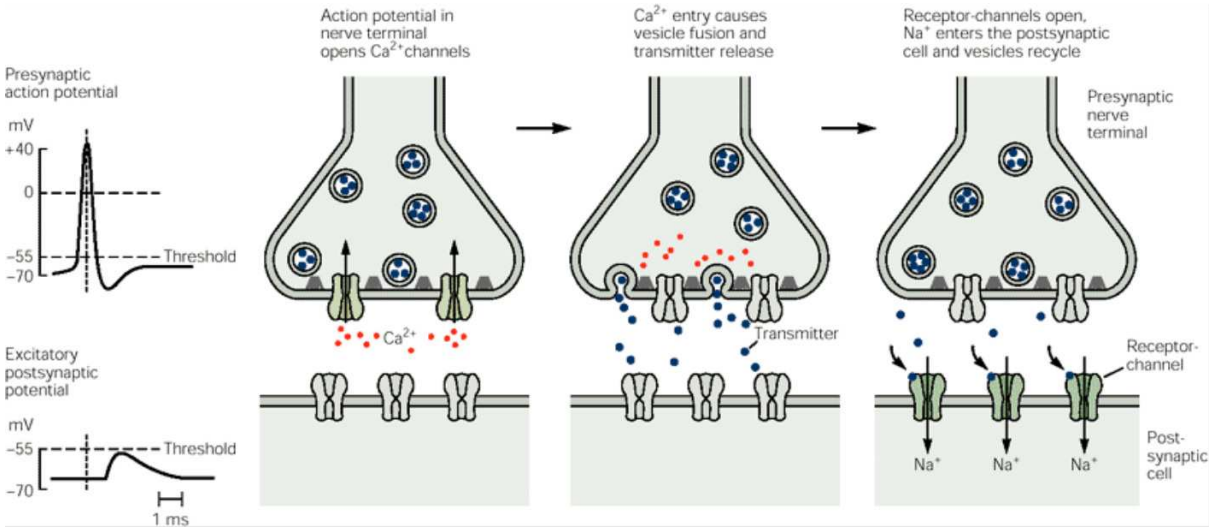


**Figure 2.2** Schematic representation of electrical synapses showing the neurotransmitter release by the pre-synaptic cell due to the influx of $Ca^{+}$, their diffusion through the synaptic cleft and their binding with the receptors at the post-synaptic neuron. The delayed response, the post-synaptic potential is also shown in comparison with the pre-synaptic action potential. (Extracted from Kandel (2000) [2]).

synaptic and post-synaptic cells. The region separating the two cells near the synapse is called synaptic cleft and sometimes the separation is greater (20-40 nm) than the usual adjacent non-synaptic intercellular space (20 nm). To cover that separation, the pre-synaptic cell relies on the release of specific chemicals, called neurotransmitters, into the cleft by its pre-synaptic terminals, usually located at the end of the axon of a neuron. The pre-synaptic terminals hold synaptic vesicles, each containing specific neurotransmitters.

The neurotransmitter vesicles are stored in a specialized membrane region called active zone. This region is sensitive to the arrival of pre-synaptic action potentials, by means of activation of $Ca^{+}$ voltage dependent ion channels. The influx of calcium triggers the release of the vesicles, which then fuse with the membrane of the pre-synaptic neuron liberating the neurotransmitter into the synaptic cleft. Once outside the pre-synaptic cell, the neurotransmitter has to diffuse through the synaptic cleft and bind to an appropriate receptor at membrane of the post-synaptic cell. The binding of the neurotransmitter activates the post-synaptic cell in some way causing a variation in the flux of ions across its membrane and therefore generating a post-synaptic potential. In Figure. 2.2 this sequence of events is illustrated. These complex structures responsible for the release of neurotransmitter causes chemical synapses to be unidirectional only, i.e. changes in the membrane potential of the post synaptic neuron do not trigger any response in the pre-synaptic neuron. Also, since the release of vesicles by the active zone depends on a large influx of calcium ions, only supra threshold stimuli (those that generate an action potential) are transmitted to the post-synaptic cell. After the post-synaptic response, a mechanism for the removal of the neurotransmitter from their binding place at the receptor must take place, otherwise the cell would rapidly become unable to respond to new incoming neurotransmitter as all the receptors become saturated. The blocking of neurotransmitter receptors is how many drugs that affects the nervous system operate.

The process of diffusion and binding of the neurotransmitter, followed by the activation of the post-synaptic cell causes a significant delay in the creation of post-synaptic potentials when compared to fast response of electrical synapses. Although there are reports of post-synaptic response delays no longer than 0.3 ms, it is common to observer delays that last several milliseconds or more. Nonetheless, chemical synapses can amplify the signal coming from the pre-synaptic neuron since a single vesicle carries within itself several thousand neurotransmitter molecules. Usually two neurotransmitter molecules are enough to induce the opening of one ion channel in the post-synaptic cell, therefore a single vesicle has the power to open thousands of ion channels, even considering that some neurotransmitter molecules are "lost" in the diffusion through the synaptic cleft, never reaching an appropriate receptor.

The activation of the post-synaptic cell after the binding of the neurotransmitters in the receptors can be either direct or indirect. In a direct process, also called ionotropic, the receptors open ion channels that are gated directly by the binding of the neurotransmitter. These are called ligand-gated ion channels. The opening of such channels causes a direct influx of ions that creates the post-synaptic potential. In an indirect processes, also known as metabotropic, the receptors modulate the production of chemical messengers inside the post-synaptic cell, also called second messengers, which in turn trigger metabolic reaction that causes the opening of ion channels. Ionotropic activation usually is associated with short duration post-synaptic potentials, during milliseconds. On the other hand, metabotropic activation causes long duration responses, lasting from seconds to minutes.

Depending on the nature of the neurotransmitter and the type of receptor, the post-synaptic potential response can be either depolarizing or hyperpolarizing. An excitatory post-synaptic potential (EPSP) happens when the post-synaptic neuron depolarizes and an inhibitory post-synaptic potential takes place when the post-synaptic neuron hyperpolarizes or when they become less susceptible to EPSPs (as in the case of shunting inhibition). The same neurotransmitter can act in both fashions, excitatory and inhibitory, depending on the type of post-synaptic receptor they are bound to.

Neurotransmitters come in a variety of types of molecules and there are many ways to classify them, although the division in amino acids, peptides and monoamines is common. Glutamate and GABA ($\gamma$-aminobutyric acid), both amino acids, are the most common excitatory and inhibitory neurotransmitters in the brain, respectively, both being able to act either ionotropically or metabotropically. For glutamate, the principal types of receptor are called AMPA ($\alpha$-amino-3-hydroxy-5-methyl-4-isoxazolepropionic acid) and NMDA (N-methyl-D-aspartate)

AMPA receptors are the typical mediators for fast excitatory currents in the brain, often with submillisecond rise and decay time constants, but also found with decay time constants of couples of milliseconds. The ion currents, most commonly composed of sodium and potassium ions, produced in the post-synaptic membrane by this type of receptor have reversal (or equilibrium) potential around 0 mV. The NMDA receptors are also excitatory current mediators but with considerably slower rising and decay constants, reaching around 20 ms. The slow kinetics of opening is due to the requirement that two neurotransmitter molecules must bind for the channel to start conducting. Their reversal potentials are also around 0 mV and are mediated by sodium, calcium and potassium ion currents. Additionally, NMDA receptors

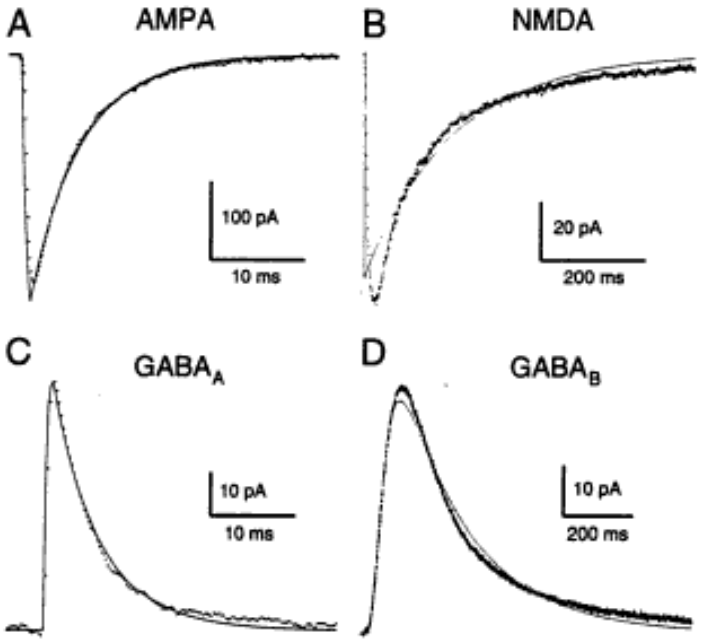


**Figure 2.3** Post-synaptic currents for the AMPA (A), NMDA (B), $GABA_A$ (C) and $GABA_B$ (D) receptors. A negative current (AMPA and NMDA receptors) means a net flow of positive charges to interior of the neuron which causes membrane depolarization, while a positive current ( $GABA_A$ and $GABA_B$ receptors) means a net flow of positive charges to the extra-cellular medium, causing membrane hyperpolarization. Time scales and current amplitudes are also shown. (Extracted from Koch & Segev (1998) [37]).

have a unique property of being blocked by physiological concentrations of the $Mg^{2+}$ ion. The blocking is voltage dependent, happening only when the post-synaptic cell is hyperpolarized, i.e. the NMDA receptor channels conduct ions only when the pre-synaptic cell is depolarized and neurotransmitters are bound to it, thus making it a molecular coincidence detector.

The GABA neurotransmitter activates two important receptors. In the central nervous system most fast inhibitory post-synaptic potentials are mediated by $GABA_A$ receptors, with reversal potential $-70$ mV controlled by chloride ion currents. Upon activation, $GABA_A$ receptors conduct $Cl^-$ reducing the chances of the occurrence of a successful action. $GABA_B$ receptors are also responsible for inhibitory post-synaptic potentials, although in a much slower time scale than the $GABA_A$ receptors. $GABA_B$ is a metabotropic type receptor (while AMPA, NMDA and $GABA_A$ are all ionotropic) that upon activation opens $K^+$ ion channels which then hyperpolarizes the membrane preventing the opening of sodium ion channels and therefore the occurrence of spikes. The reversal potential of $GABA_B$ receptors, around $-100$ mV, is mediated by second messengers that are associated with the opening of potassium ion channels, causing IPSPs to be much more hyperpolarized then the ones due to $GABA_A$ receptors.

Figure 2.3 shows the post-synaptic currents caused by each of the four receptors mentioned here. The negative currents of the AMPA and NMDA receptors means that a net flow of positive charges is directed to the interior of the neuron, thus causing the membrane to depolarize,

while the positive currents of $GABA_A$ and $GABA_B$ means that a net flow of positive charges is directed to the extra-cellular medium, therefore hyperpolarizing the cell. The time scale and the amplitude of the currents for each receptor can be compared.

Neurons in the nervous system are connected to several thousand others through synapses. Usually, each neuron receives a combination of excitatory and inhibitory synapses and the combination of the arriving EPSPs and IPSPs determines whether the post-synaptic neuron will fire or not. EPSPs and IPSPs arriving at different parts of the post-synaptic neuron travel down to the cellular body where they are added together. In this fashion, the soma acts as a computer, passing the "result" of its calculation to the axon hillock: if the net potential is greater than the firing threshold, an action potential will be generated and conducted by the axon. The origin point of a post-synaptic potential in the post-synaptic neuron has great influence in the result, for an EPSP or IPSP coming from a dendrite far away from the soma suffers more with passive membrane attenuation than a potential that is generated near the soma. A temporal summation can also occur, where potentials arriving in quick succession overlap and summate with each other, but it is necessary that the potential last longer than the interval between pre-synaptic spikes. In Figure 2.4 we show how a single pre-synaptic neuron firing fast enough can induce an action potential in a post-synaptic neuron. One spike alone does not produce an EPSP strong enough to create a spike, but adding the overlapping EPSPs caused by three successive spikes causes a suprathreshold stimulation.

### 2.1.3 Mathematical models of synapses

In the same way that the neuronal dynamics and its excitation mechanisms can be described by mathematical equations, so does the generation of post-synaptic potentials in the synapses. Here we are going to focus only on mathematical models for chemical synapses, since in general their dynamics are more complex than electrical synapses.

Modeling chemical synapses is a two part effort: firstly, the concentration of neurotransmitter released in the synaptic cleft by the pre-synaptic neuron must be known and secondly how this concentration induces the ionic currents once the neurotransmitters are bound to their receptors. Models for both phases of post-synaptic potentials generation usually involve kinetic considerations, taking into account transition rates between states of ionic channels or receptors. These models are similar to the model describing transition to open or close states of activation particles in the Hodgkin-Huxley model (Eq. (1.14)). For example, a proposed kinetic model [39, 40] for the release of neurotransmitters contemplate many states:

$$\begin{aligned} &\xrightarrow{k(V_{pre})} \mathrm{Ca}^{2+} \\ 4\mathrm{Ca}^{2+} + X &\underset{k_u}{\overset{k_b}{\rightleftharpoons}} X^* \\ X^* + V_e &\underset{k_2}{\overset{k_1}{\rightleftharpoons}} V_e^* \\ V_e^* &\xrightarrow{k_3} nT \\ T &\xrightarrow{k_c} \end{aligned} \tag{2.1}$$

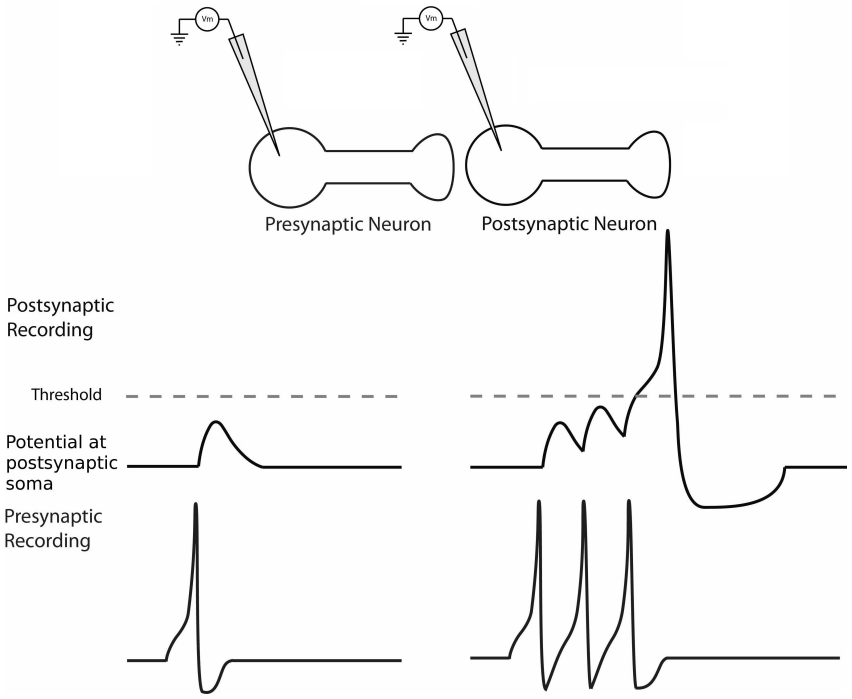


**Figure 2.4** Excitatory post-synaptic potentials arriving from a single pre-synaptic neuron may or may not induce a spike. A EPSP from one spike does not reach the post-synaptic soma with enough amplitude to create spike. Three spikes fired in quick succession however make the EPSPs overlap, adding to a suprathreshold stimulation. (Image under Creative Commons License, adapted from the original work of Curtis Neveu [38]).

where $V_{pre}$ is the pre-synaptic neuron potential, $X$ and $X^*$ are the non-activated and activated state of the calcium protein that releases the neurotransmitter vesicles, $V_e$ and $V_e^*$ are the non-activated and activated states of the neurotransmitter vesicles, $T$ is the neurotransmitter released in the synaptic cleft and $n$ is the number of neurotransmitter inside the vesicle. Although this model does not capture all the details of the neurotransmitter release process, it is still too complex if used for computations that involve a large number of synapses. A simpler representation can be made taking into account that the concentration of neurotransmitter $[T]$ follows $V_{pre}$ closely [39]:

$$[T] = \frac{T_{max}}{1 + e^{-(V_{pre} - V_p)}/K_p}, \tag{2.2}$$

where $T_{max}$, $V_p$ and $K_p$ are parameters that can be fit to experimental data. Further simplification of this model can be made if it is assumed that $[T]$ in the synaptic cleft rises extremely fast after vesicle release, remaining at a high value $T_{max}$ for a period $\bar{t}$ and then falls rapidly to zero, therefore making $[T]$ a step function of the time.

With a model for the neurotransmitter concentration in the synaptic cleft we can now look at post-synaptic response models that aim for the determination of currents associated with each receptor type. For fast response receptors (AMPA and $GABA_A$) this current can be obtained

from a simple first order kinetic reaction:

$$C + T \underset{\beta}{\overset{\alpha}{\rightleftharpoons}} O, \tag{2.3}$$

where $C$ is the closed state and $O$ is the open state of the ionic channel associated with the receptor and $T$ is a neurotransmitter molecule. From Equation 2.3 follows that:

$$\frac{ds}{dt} = \alpha[T](1-s) - \beta s, \tag{2.4}$$

where $s$ is the fraction of channels in the open state and $[T]$ is the concentration of neurotransmitter in the synaptic cleft. The fast synaptic currents follow a standard model for a current through an ionic channel:

$$I^i_{syn} = \overline{g_i} s(V_{post} - E_i), \tag{2.5}$$

where $i$ corresponds to the appropriate receptor type (AMPA or $GABA_A$), $g_i$ is the maximum channel conductance, $V_{post}$ is the post-synaptic membrane potential and $E_i$ is the reversal potential of the receptor. The change in $V_{post}$ due to the synaptic current then is:

$$C\frac{dV_{post}}{dt} = -I^i_{syn}, \tag{2.6}$$

where $C$ is the membrane capacitance (see Eq. (1.10)).

The final step to obtain $V_{post}$ as a response to the synaptic current is to solve Eq. (2.4) considering the model for the neurotransmitter concentration $[T]$. If we admit the simple assumption of $[T]$ as a step function of time (as mentioned before) then the fraction of open channels $s$ can be solved exactly resulting:

$$s(t) = \begin{cases} s_\infty + (s(0) - s_\infty)e^{-t/\tau_s} & \text{if } [T] = T_{max}, \\ s(0)e^{-\beta t} & \text{if } [T] = 0, \end{cases} \tag{2.7}$$

where $s_\infty = \alpha T_{max}/(\alpha T_{max} + \beta)$, and $\tau_s = 1/(\alpha T_{max} + \beta)$.

Although the slow response of NMDA and $GABA_B$ receptors can be modeled in a similar way, a more complex functional dependency is needed in Eq. (2.5). Another way to describe both the rise and fall of the conductance is to express $s$ as a so-called alpha function. For an isolated pre-synaptic action potential occurring at $t = 0$ the synaptic conductance is written as:

$$s(t) = \frac{s_{max} t}{\tau_s}(e^{(1-t/\tau_s)}), \tag{2.8}$$

where $s_{max}$ is the maximum conductance, achieved at time $\tau_s$ followed by a decay with time constant $\tau_s$

A more detailed review of the well-established subjects covered in the past section can be found in the following references, from which this text was based on: the textbooks by Peter Dayan and L. F. Abbott (2001) [1], E. R. Kandel (2000) [2], Christof Koch (1999) [11]), Christof Koch and Idan Segev (1998) [37] and the lecture notes by Sue A. Campbell (2010) [41].

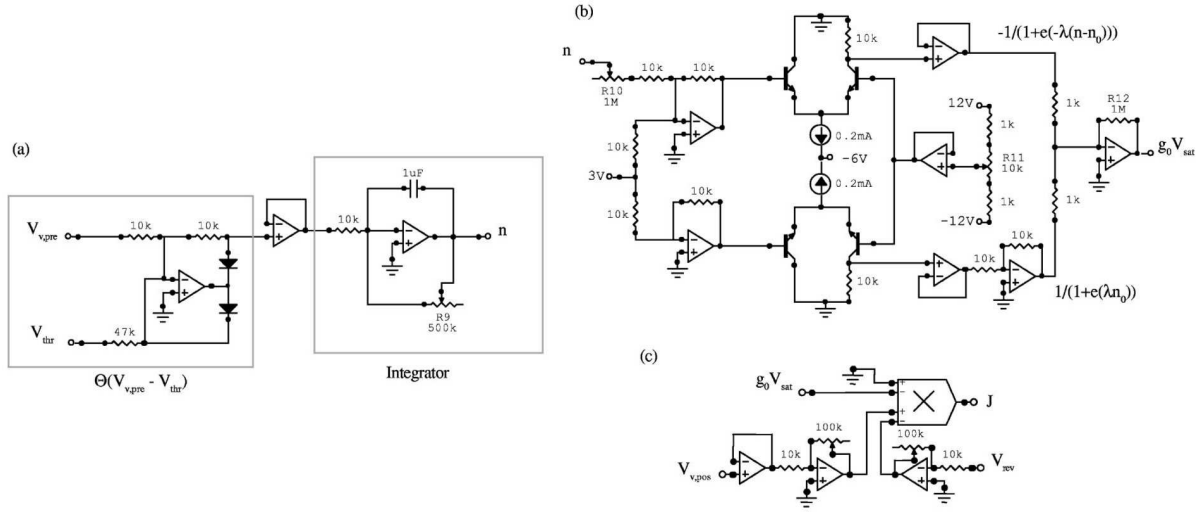


**Figure 2.5** Aliaga *et al.* electronic chemical synapse. a) The first circuit block implements the $\Theta$ function while the second performs the integration of Eq. (2.9)a. b) This circuit outputs a voltage $g_0 V_{sat}$ where $V_{sat}$ corresponds to the term inside the second parenthesis of Eq. 2.9b. c) This circuit performs the evaluation of the difference between the post-synaptic potential $V_{v,pos}$ and the constant $V_{rev}$ and multiplies it with the output of the circuit shown in (b). (Adapted from Aliaga *et al.* (2003) [18]).

## 2.2 Electronic models of synapse

There are many artificial synapses reported in the literature. Their construction methods and purpose vary greatly from author to author, but the basic principle behind those devices is to mimic the behavior of either electrical or chemical synapses. Here we discuss a few selected models that fulfill this basic idea.

In the work of Ciszak *et al.* [42], where two electronic neurons obeying the FitzHugh-Nagumo model equations were coupled together in a master-slave setting, i.e. the connection is unidirectional, to observe anticipating behavior from the slave neuron. The connection between the two neurons was made by a single resistor, that due it its passive electric properties, mimics an electrical synapse.

Szûcs *et al.* [17] used a electronic circuit modeled by three dimensional differential equations to interact with real neurons of the stomatogastric ganglion of crustaceans. In order to do that, an electronic circuit simulating an electrical synapse was employed, allowing the experimenter to set its conductance. In this circuit the sign of the resulting current flowing from the electronic neuron to the real neuron depends on the actual potential difference of between the two neurons.

Pinto *et al.* [43] used computer simulated synaptic currents to transmit signals to real neurons. They employed complex circuits to convert digital signal from the computer to analog signals with great physiological precision. This also allowed them to simulate neurons with equal precision. The complexity of the circuit allowed them to change synaptic parameters in real time, even while they are connected to real neurons.

Aliaga *et al.* [18] designed an electronic neuron replacement for a midbody ganglion neuron

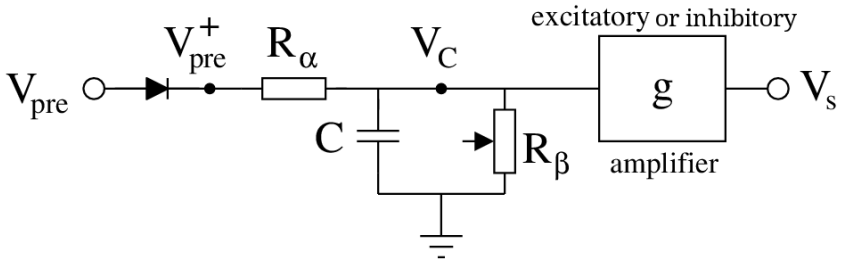


**Figure 2.6** Circuit that mimics the behavior of a chemical synapse. $V_{pre}$ is the pre-synaptic input, while $V^{+}_{pre}$ takes into account only positive values of $V_{pre}$. The resistances $R_\alpha$, $R_\beta$ and the capacitor $C = 10$ nF control the time scale $\tau$ of the synapse. The equivalent of the synaptic conductance $g$ can be set by a standard amplifier (see Appendix A), which yields the post-synaptic potential $V_s = gV_C$.

of the leech Hirudo medicinalis. To integrate their electronic neuron with the tissue of the ganglion they employed an electronic synapse modeled by a set of equations derived from a first order kinetic reaction that also incorporates neurotransmitter concentrations, therefore mimicking the behavior of chemical ionotropic synapses. Their model is as follows:

$$\frac{dn}{dt} = \Theta(V_{v,pre} - V_{thr}) - \gamma n, \tag{2.9a}$$

$$J = g_0(V_{v,pos} - V_{rev})\left(\frac{1}{1+e^{-\gamma(n-n_0)}} - \frac{1}{1+e^{\lambda n_0}}\right), \tag{2.9b}$$

where $\theta$ is the Heaviside function, $n$ is the neurotransmitter concentration, $J$ is the synaptic current, $\gamma$ is the neurotransmitter loss rate, $V_{v,pre}$ and $V_{v,pos}$ are the pre and post-synaptic potentials, $V_{thr}$ is the voltage above which the pre-synaptic cell releases neurotransmitters and $V_{rev}$ is the reversal potential while $g_0$, $\lambda$ and $n_0$ are parameters that characterize the saturation nature of the current. Figure 2.5 shows the circuits designed by Aliaga *et al.* to implement the synaptic Equations (2.9).

## 2.3 A simple electronic model for fast chemical synapses

To move forward towards our goal of creating networks of electronic excitable elements we need a model of electronic synapse to connect such elements. Here we differentiate from the previously presented models of artificial synapses in the aspect of simplicity. Again, we prioritize simple devices which have a straightforward mathematical description and also allow to be easily reproduced. With that in mind, it is also desirable that such device offers some freedom of choice regarding its parameters, such as rise and decay time constants and conductance values. Therefore we opt for a chemical-synapse-inspired device, for chemical synapses in general have a richer dynamics when compared to electrical ones.

The circuit of our electronic synapse is presented in Fig. 2.6. At its input voltage $V_{pre}$, it receives signal coming from one of our electronic excitable circuit presented in Fig. 1.16 after the two dynamic variables have been analogically subtracted (as in Fig. 1.22a). In this way, the electronic excitable circuit works as a pre-synaptic neuron. Due to the diode at its input, it is

activated whenever the output $V_{pre}$ of the pre-synaptic neuron becomes positive ($V_{pre}^{+}$), which happens only during a spike (shown in Fig. 1.21e, for example.) The capacitor $C$ and the two resistances $R_\alpha$ and $R_\beta$ are responsible for setting the rise and decay time scales $\tau$ of the output of our electronic synapse. The block labeled $g$ sets the value of the synaptic conductance and also determines if the circuit will produce EPSPs our IPSPs, i.e. if the synapse will be excitatory or inhibitory. The electronic analog $V_s$ of the excitatory or inhibitory post-synaptic potential is obtained by multiplying the voltage $V_c$ at the capacitor $C$ by a controllable gain $g$ with a standard operational amplifier circuit [24] which effectively controls the strength of the coupling between pre and post-synaptic electronic neurons:

$$V_s = gV_c, \tag{2.10}$$

with the sign of $g$ determining the if $V_s$ corresponds to an EPSP or IPSP.

The mathematical description of the electronic synapse circuit follows directly from the application of Kirchoff' laws. If $I = i_1 + i_2$ is the current flowing through the resistance $R_\alpha$ and $i_1$ is the current through the capacitor $C$, we can write:

$$i_1 = C\frac{dV_c}{dt} = I - i_2. \tag{2.11}$$

Since the current $I$ and $i_2$ can also be written in terms of $V_c$ as:

$$I = \frac{V_{pre}^{+} - V_c}{R_\alpha}, \tag{2.12a}$$

$$i_2 = \frac{V_c}{R_\beta} \tag{2.12b}$$

Hence the differential equation governing the voltage at the capacitor $C$ is:

$$\frac{dV_c}{dt} = \frac{1}{R_\alpha C}(V_{pre}^{+} - V_c) - \frac{V_c}{R_\beta C}. \tag{2.13}$$

Equation (2.13) can be rewritten in the form:

$$\frac{dV_c}{dt} = \frac{1}{\tau}\left[V_\infty(t) - V_c\right], \tag{2.14}$$

where the characteristic rise time is $\tau = \tau_{up} = \frac{R_\alpha R_\beta C}{R_\alpha + R_\beta}$ and the asymptotic value is $V_\infty(t) = \left(\frac{R_\beta}{R_\alpha + R_\beta}\right) V_{pre}^{+}(t)$. Equation (2.14) is only valid when $V_{pre} > 0$. If, however, $V_{pre}^{+}(t) = 0$ (when the pre-synaptic output $V_{pre}$ is zero or negative) the characteristic decay time reduces to $\tau = \tau_{down} = R_\beta C$ since the diode does not allow the capacitor to discharge through the resistor $R_\alpha$. In this model we disregard the voltage drop caused by the diode at the voltage $V_{pre}^{+}$ since it is small when compared to the amplitude of the spike of the electronic excitable circuit.

First order kinetics such as that of Eqs. (2.13) and (2.14) describing the behavior of electronic synapse have close similarity with the Eq. (2.4), thus making our circuit a reasonable

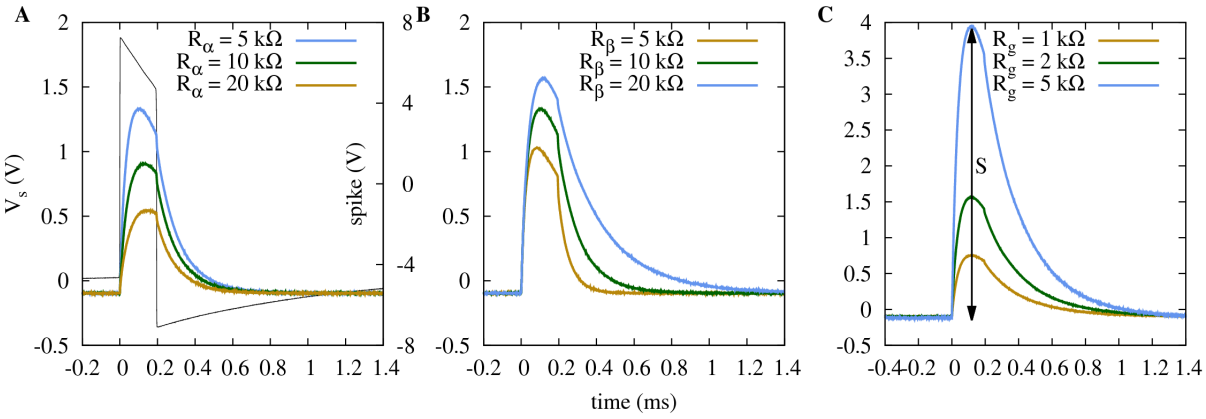


**Figure 2.7** Output $V_s$ of the electronic synapse when subjected to a pre-synaptic spike. (A) Black line corresponds to the pre-synaptic spike (scale on the right). The rise time of $V_s$ is governed by $R_\alpha$ ($R_\beta = 10$ kΩ, $R_g = 2$ kΩ), while (B) changes in $R_\beta$ influence the decay time of $V_s$ (when $V^+_{pre}(t) = 0$ V; $R_\alpha = 5$ kΩ, $R_g = 2$ kΩ). (C) The gain $g$ is proportional to the amplifier resistance $R_g$, which affects only the maximum amplitude $S$ of $V_S$ ($R_\alpha = 5$ kΩ, $R_\beta = 20$ kΩ). The synaptic time scales in each figure, calculated from the capacitance and resistance values are (A) $\tau_{up} = 0.33$ ms (blue line), $\tau_{up} = 0.5$ ms (green line), $\tau_{up} = 0.66$ ms (yellow line) and $\tau_{down} = 0.1$ ms; (B) $\tau_{up} = 0.4$ ms and $\tau_{down} = 0.2$ ms (blue line), $\tau_{up} = 0.33$ ms and $\tau_{down} = 0.1$ ms (green line), $\tau_{up} = 0.25$ ms and $\tau_{down} = 0.05$ ms (yellow line); (C) $\tau_{up} = 0.4$ ms and $\tau_{down} = 0.2$ ms.

approximation for the dynamics of chemical synapses with fast responses such as those mediated by AMPA (excitatory) or $GABA_A$ (inhibitory) receptors. This is achieved with minimum use of electronic components of extremely low complexity.

As shown in Fig. 2.7, this setup allows us to control several interesting features of the electronic synaptic output, here behaving as an EPSP: $R_\alpha$ controls the rise time of $V_s$ (Fig. 2.7A), $R_\beta$ controls the decay time of $V_s$, while both have influence on its maximal value $S$, (Fig. 2.7B), which can also be independently controlled by the gain $g$ (Fig. 2.7C). The gain $g$ is proportional to control resistance $R_g$ in the amplifier circuits of the block $g$ shown in Fig. 2.6 (see Appendix A for details on basic op-amp circuits). From hereon the maximum value $S$ of the synaptic output $V_S$ will be referred as synaptic strength or synaptic amplitude.

To couple two electronic excitable circuits using the electronic synapse the synaptic output $V_S$ is added to the input voltage of the post-synaptic circuit together with the constant DC signal $V_{DC}$ and the noisy input from the circuit shown in Fig. 1.22a:

$$V_{in} = V_{DC} + V_{noise} + gV_C \,. \tag{2.15}$$

If the noisy input is set to zero and the two excitable circuits are in the tonic regime, i.e. with $V_{DC}$ above the Hopf bifuracation and both circuits are firing regular spike trains, it is possible to observe a regime where both circuits fire together, with a fixed time difference between pre and post-synaptic spikes. This time difference can be characterized as a function of the synaptic parameters. We focus on the synaptic amplitude $S$ and the decay time constant (controlled by $R_\beta$) which have more pronounced influence on the post-synaptic response. It is important

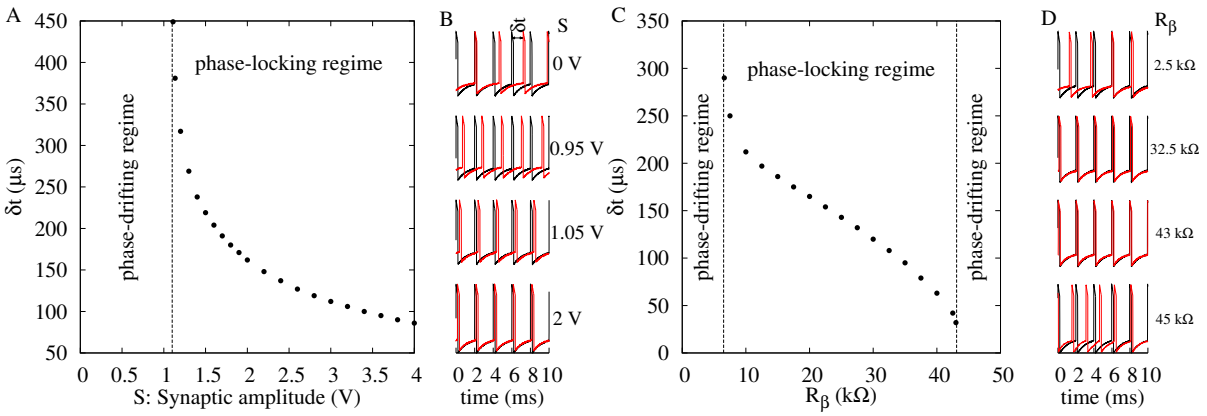


**Figure 2.8** (A) Time difference $\delta t$ between pre and post-synaptic spikes as a function of the synaptic amplitude $S$ when the electronic excitable circuits are in a tonic regime. For values of $S$ below a critical value the phase between pre and post-synaptic spikes is not defined as the circuits fire at different frequencies. After that point the phase becomes constant for any given value of $S$ and increasing values of $S$ decreases $\delta t$. (B) The spike trains of pre-synaptic (black lines) and post-synaptic (red lines) excitable circuits are shown for different values of $S$. From top to bottom: uncoupled circuits showing their natural frequencies ($S = 0$ V); increase in the mean firing rate of the post-synaptic circuit before the phase-locking; circuits in the phase-locking regime; decrease in $\delta t$. Parameters are $R_\alpha = 5$ kΩ, $R_\beta = 20$ kΩ $V_{Hopf}(pre) = -7.70$ V, $V_{Hopf}(post) = -7.40$ V, $V_{DC} = -7.00$ V. (C) Same as (A) but with $S$ fixed and $R_\beta$ varying. In this case $\delta t$ responds to changes in the decay time constant in similar way to what we observe for the response to changes in the synaptic amplitude, the only difference being that for large enough values of $R_\beta$ phase-locking is lost due to the increase in the period in which the synaptic response is active. (D) Same as (C) but values of $R_\beta$ are shown instead of $S$. Parameters are equal except for $R_g = 2$ kΩ.

to remember that the coupling provided by the electronic synapse is unidirectional, i.e. the post-synaptic excitable circuit has no influence on the post-synaptic one.

### 2.3.1 Coupling in the absence of noise

To test our electronic synapse, we couple two electronic excitable circuits with the simplest configuration: a pre-synaptic electronic neuron connected to a pos-synaptic neuron with a single excitatory synapse. Here we aim to reproduce known results regarding phase differences between pre- and post-synaptic spikes that emerge from this simple configuration [44].

Figure 2.8a shows the time difference $\delta t$ between the pre-synaptic and post-synaptic excitable circuits when the synaptic amplitude $S$ is varied. The two presumed identical electronic neurons are subject to the same DC input $V_{DC}$ setting both in the tonic regime, but due to differences in the electronic components (within factory tolerance) they have different voltage values for their Hopf bifurcations, therefore causing the pre-synaptic excitable circuit to fire at a slightly greater frequency than the post-synaptic excitable circuit when they are disconnected, i.e. when $S = 0$. For small values of the synaptic amplitude $S$ the phase between the spikes of both neurons is not constant, therefore the system is said to be in a phase-drifting regime. There

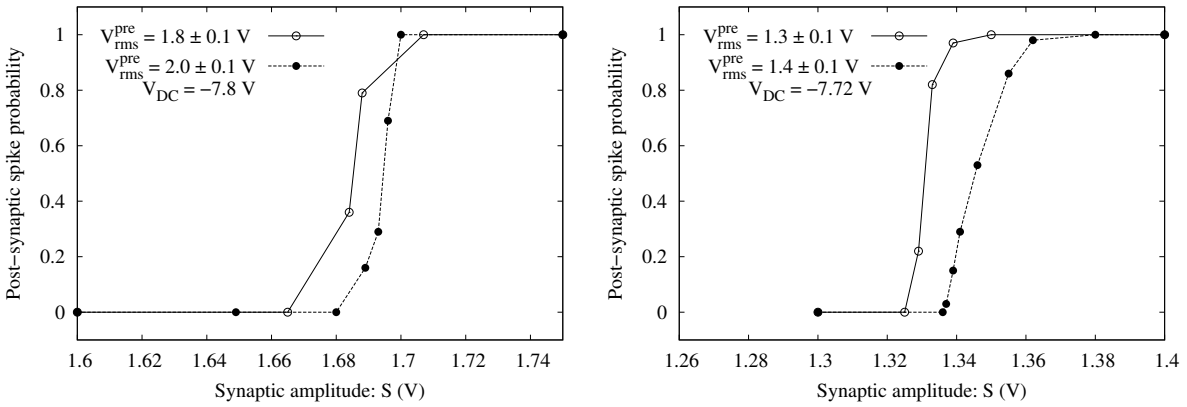


**Figure 2.9** Post-synaptic spike probability measured when noise is introduced only in the pre-synaptic input and both pre- and post-synaptic circuits are in the excitable regime as a function of the synaptic amplitude $S$. As the DC input is increased, becoming less negative, the synaptic amplitude required to induce a post-synaptic spike becomes smaller. The qualitative behavior of the probability, characterized by the small region where the probability of a post-synaptic spike is greater than zero and smaller than one, is the same for different values of the DC input and noise amplitude ($V^{pre}_{rms}$).

is, however, a value of $S$ from which this phase, and consequently $\delta t$, becomes constant, with their values becoming smaller as $S$ is increased. The system is said to be in a phase-locking regime.

Figure 2.8b shows the time difference $\delta t$ as a function of the resistance $R_\beta$ which controls the decay time $\tau_{down}$ of the synaptic input. Again, for a weak coupling between the two excitable circuits the system stays in a phase-drifting regime and, above a critical value, increasing values of $R_\beta$ makes the system go into a phase-locking regime. The difference from the previous case is that for a large enough value of the decay time constant phase-locking is lost due to the increased duration of the synaptic response to the input spike. In that regime, each pre-synaptic spike generates, on average, more than one spike in the post-synaptic circuit. This kind of measurement might be relevant for future studies involving more than two excitable elements where synchronous firing is important, such as anticipated synchronization [42, 45] and spike-timing dependent synaptic plasticity [46].

### 2.3.2 Coupling in the presence of noise

To study how noise affects the generation of spikes in the post-synaptic circuit, we first introduce noise only in the pre-synaptic excitable circuit while keeping both elements in an excitable regime, i.e. the DC input (equal for both elements) is such that no spikes are generated by any of the excitable circuits in the absence of noise. The post-synaptic spike probability given the recent occurrence of a pre-synaptic spike is obtained by measuring the mean number of spikes generated at the post-synaptic excitable circuit per spike generated at the pre-synaptic excitable circuit as a function of the synaptic amplitude $S$. Using this approach we can isolate the effect of the synapse in the generation of spikes in the post-synaptic circuit. As shown in Fig. 2.9, the region where the post-synaptic spike probability is between zero and one is very

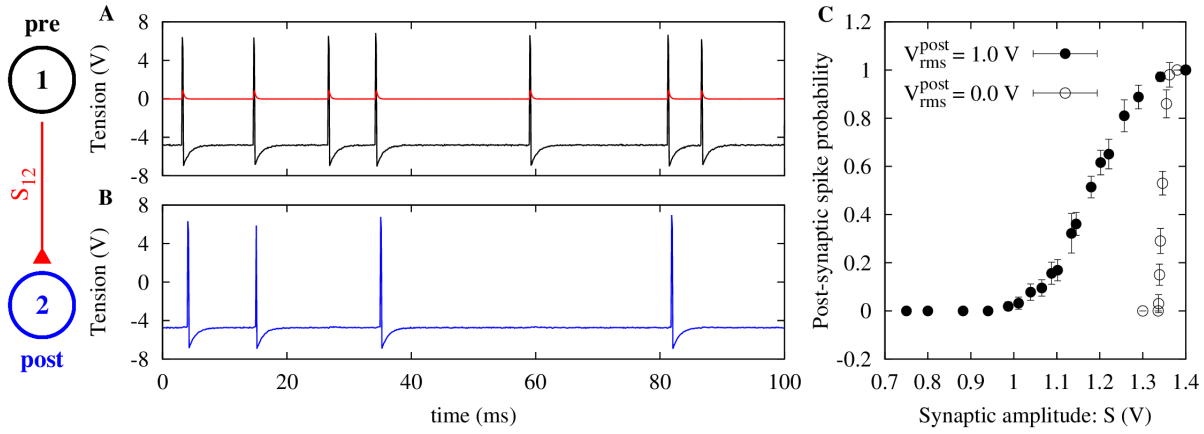


**Figure 2.10** (A) Spike train of a pre-synaptic neuron (black line) excited by noise ($V_{rms}^{pre} \simeq 1.2$ V) and the resulting $V_S$ with $S_{12} \simeq 1.3$ V (red line). (B) Spike train of a post-synaptic neuron (blue line) excited by $V_S$ and a lower noise intensity input ($V_{rms}^{post} \simeq 1.0$ V). (C) Post-synaptic spike probability as a function of $S$ for two values of $V_{rms}^{post}$. In both cases, the pre-synaptic neuron is subjected to $V_{rms}^{pre} \simeq 1.2$ V.

small (only of order 50 mV, while $S$ can easily reach 2 V). The qualitative response of the post-synaptic circuit does not change with different values of noise amplitude, here expressed as its root mean square value:

$$V_{rms} \equiv \sqrt{\langle V_{noise}^2 \rangle}. \tag{2.16}$$

Increasing the DC voltage, i.e. making it less negative, therefore causing the electronic neurons to be more "excitable", reduces the synaptic amplitude necessary to induce post-synaptic spikes, but otherwise has little influence on the general form of the post-synaptic spike probability.

Now, if noise is introduced in the post-synaptic circuit as well as in the pre-synaptic one the post-synaptic spike probability change its behavior greatly. The noisy input for each excitable circuit is generated independently by two different noise generator circuits (Fig. 1.22a), therefore the noisy inputs are expected to have no correlation with each other. Figure 2.10 shows a time series of a pre-synaptic electronic neuron (labeled 1) with noise intensity $V_{rms}^{pre} \simeq 1.2$ V and the corresponding EPSPs it generates whenever it spikes. A post-synaptic electronic neuron (labeled 2), also in its excitable regime, receives those EPSPs as well as noise from another noise generator circuit, but with lower intensity $V_{rms}^{post} \simeq 1.0$ V. Driven by this lower-intensity noise alone, the post-synaptic neuron is extremely unlikely to fire, which it eventually does upon receiving an EPSP with peak voltage $S_{12} = 1.3$ V (Figs. 2.10A and B). In Fig. 2.10C the region where the post-synaptic spike probability is different from zero or one is increased significantly. The probability increases monotonically with the synaptic amplitude $S$, with a sensitivity threshold that decreases with increasing noise intensity $V_{rms}^{post}$. Although chemical synapses sometimes show great efficiency in generating post-synaptic action potentials (for example in nerve-muscle synapses every spike in the motor neuron causes a spike in the muscle fiber [2]), in the central nervous system neurons usually require the arrival of multiple EPSPs for a post-synaptic spike to be generated, giving the process a more probabilistic character. The

noise also helps our model of electronic synapse to simulate the random diffusion of neurotransmitters through the synaptic cleft, as not every neurotransmitter actually reaches a receptor in the post-synaptic neuron.

CHAPTER 3

# Symmetry and coherence effects in two-neuron systems with excitatory coupling

As discussed in the introductory chapter, neurons are highly nonlinear dynamical systems which are typically connected to tens of thousands of other neurons, the whole system being subjected to fluctuations whose stochasticity cannot be dismissed. This interplay between nonlinearity, high dimensionality and noise is what renders the brain a difficult and interesting system to study [1, 37]. More generally, the last decades witnessed a surge in theoretical studies of collective phenomena of interacting nonlinear units. Since the seminal work of Kuramoto [47], for example, several aspects of synchronization have been addressed [48]. With the emergence of complex networks becoming a research topic in itself [49], the effects of topology on synchronization have been thoroughly investigated (see e.g. [50, 51, 52] for recent examples, or [53] for a review). Recently, even the notion of networks of networks have emerged in the context of climate studies [54].

Even single neurons, however, can reveal surprises. As mentioned before, in 1997, Pikovsky and Kurths unveiled the phenomenon of coherence resonance (CR), whereby an excitable system driven by white noise produces a spike train whose regularity (or coherence) attains a maximum at some finite value of the noise intensity [27]. In the low-noise regime, the spike train approaches a Poissonian incoherent behavior with small firing rate, whereas in the high-noise regime incoherence coexists with a large firing rate. At the resonance, the spike train looks almost periodic, despite the fact that the system is in an excitable regime, not tonic.

The collective effects of coupling on CR were subsequently investigated. It was shown that global coupling, either by square pulses [55] or via electrical synapses (gap junctions) [56], can lead to network synchronization with strong coherence. It was also shown that a network of excitable elements can exhibit system size CR, where increasing the number of elements in system leads, at first, to an increase in global coherence, while very large networks have reduced global coherence [56, 57]. In addition, chemical synapses were shown to be better at increasing global coherence than gap junctions, even when the analyzed network contained only two neurons [57]. This highlights the importance of the characteristic times introduced by the chemical coupling in the post-synaptic response.

Our aim in this chapter is twofold. First and foremost, we depart from previous studies on CR in networks of model neurons in that all of them have focussed on the effects of some coupling among the units which was *uniform* across the network: Wang et al. have employed the same uniform coupling intensity among all pairs of Hodgkin-Huxley neurons [55]; Toral and Mirasso had a single variable to parameterize the gap junction conductance among their FitzHugh-Nagumo elements [56]; and Balenzuela and García-Ojalvo simulated Morris-Lecar

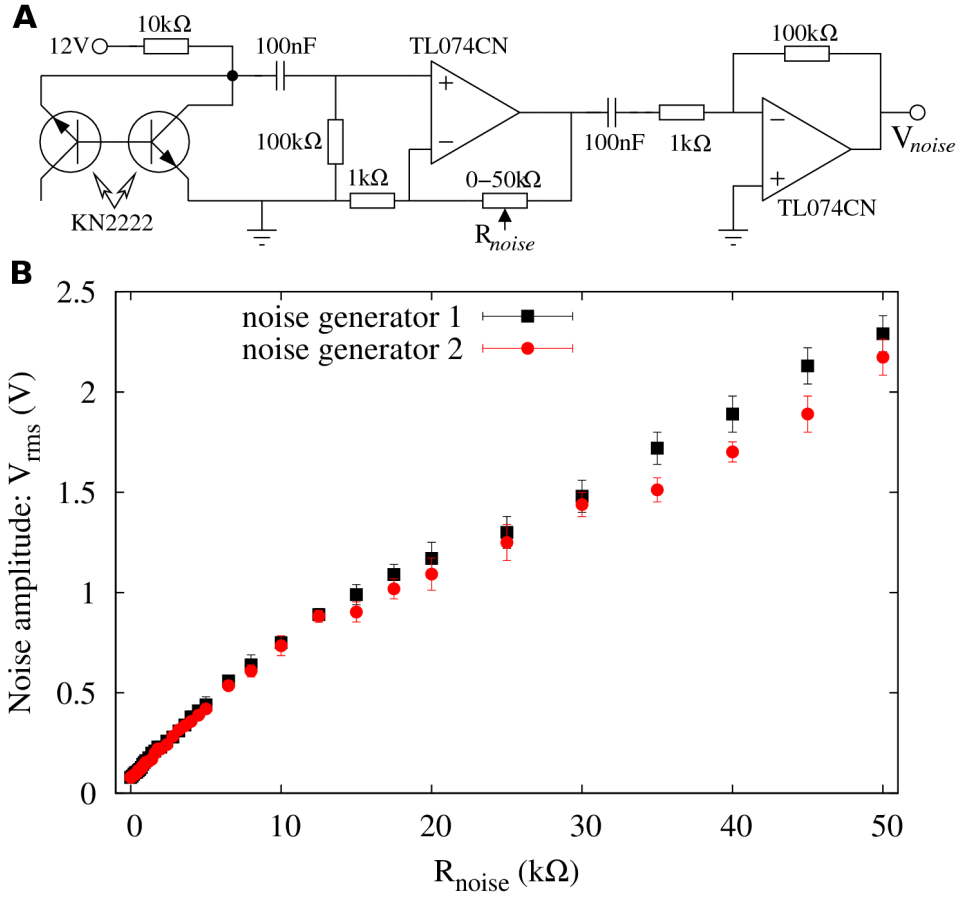


**Figure 3.1** (A) Noise generator circuit presented in Fig. 1.22a, here with all electronic component values specified. The resistance $R_{noise}$ controls the amplitude of the voltage $V_{noise}$. (B) $V_{rms}$ as a function of $R_{noise}$ showing an approximately linear dependence for both noise generator circuits used.

systems with chemical and electrical synapses: in either case, the same coupling intensity that connected neuron $i$ to neuron $j$ was also applied from $j$ to $i$. In other words, previous analyses of collective effects have dramatically reduced the dimensionality of coupling space by focusing on the single-axis projection of uniform coupling. This is a convenient choice to render parameter space scanning feasible, but not very realistic. In nature, mutually connected neurons most probably are not symmetrically coupled.

Here we set forth to investigate what happens to the coherence of spike trains when the coupling among the units is not necessarily uniform. Specifically, we fully explore the space of coupling intensities by focusing on the analysis of the simplest network, namely, a pair of neurons. We will show that: 1) synaptic asymmetry can deteriorate the coherence of a pair of neurons that were previously uncoupled; 2) synaptic symmetry leads the system to a more coherent state, compared with the uncoupled case; 3) the effects of synaptic symmetry on the system coherence is strongly dependent on the characterstic time scale of the synapses.

Second, we go beyond the numerical simulations of previous models by employing our type-II-excitable [13] electronic circuits which are connected via our model of electronic synapse

that mimics the behavior of fast chemical synapses. These electronic neurons are set at the edge of their Hopf bifurcation, as previously described in Section 1.8 (see also [23, 58]). The use of such electronic circuits gives our results an additional degree of robustness due to the variability of the electronic components and influence of external effects (such as thermal noise), all of which contribute to a more biologic-like scenario of noise and heterogeneities.

In what follows, experimental results were obtained with electronic neurons whose parameters were chosen to be as similar as possible (within the $\sim 5\%$ tolerance of the electronic components). The value of the capacitance in Fig. 1.16 is chosen to be 1 nF to keep the time scale of the electronic neurons in the millisecond range and DC voltage is set at $V_{DC} = -7.30$ V. For the synapses (Fig. 2.6), the capacitance has value $C = 10$ nF. The noise intensity will be denoted by the resistance $R_{noise}$ controlling the gain of the noise amplifier, shown in detail in the circuit of Fig. 3.1A, since the voltage $V_{rms}$ in Eq. 2.16 increases approximately linearly with $R_{noise}$ as shown in Fig. 3.1B. Experimentally, the peak value (amplitude) $S$ of the EPSP $V_S$ (see Fig. 2.7C) is easier to measure than the gain parameter $g$, and will therefore be used as a measure of the synaptic strength, with $S_{ij}$ denoting the coupling from neuron $i$ to neuron $j$ (with $(i, j) \in \{(1,2),(2,1)\}$, in the present case). To measure the coherence (or incoherence) of spike trains we use the parameter $R_p$ introduced earlier in Eq. (1.53), the normalized standard deviation of the interspike intervals.

## 3.1 Coherence deteriorates with an incoming synapse, but is restored with an outgoing synapse

To investigate the effects of symmetry in the synaptic coupling on the coherence of spike trains, we started by the asymmetrical extreme of connecting two neurons unidirectionally. As shown in Fig. 3.2A, the incoherence $R_p^1$ of the pre-synaptic neuron 1 exhibits a minimum as a function of the noise intensity, as is typical of CR. Due to the synapse from neuron 1 to neuron 2 (with synaptic amplitude $S_{12} = 1.0$ V), the spike trains of neuron 2 are less coherent than those of neuron 1 (Fig. 3.2A). This could be expected, since neuron 2 is receiving noise-induced spikes from neuron 1 in addition to its own (independent) noise source. In this simple scenario, the behavior of the pre-synaptic neuron is, as expected, unaffected by its outgoing synapse.

Keeping the synapse from neuron 1 to neuron 2, we added another synapse in the opposite direction, with the same synaptic amplitude ($S_{21} = 1.0$ V). This reverted the effect of the single synapse, causing neuron 2 to reattain a minimum in the $R_p^2$ vs $R_{noise}$ curve, as shown in Fig. 3.2B. This is perhaps counterintuitive, since one might expect that, by synaptically coupling the less coherent neuron 2 spike train with neuron 1, $R_p^1$ should increase. What happens, however, is that not only the coherence of neuron 1 is weakly affected, but also neuron 2 recovers its coherence. More importantly, it does so by means of an outgoing synapse.

We explored how the above phenomenon unfolds as we gradually change the synaptic strengths. We started with initially uncoupled electronic neurons ($S_{12} = S_{21} = 0$ V) and noise intensity near its resonance value ($R_{noise} = 10$ k$\Omega$). This choice of noise intensity was made in order to maximize the variation of the incoherence parameter $R_p$ as the coupling is varied (see Fig. 3.2A and Fig. 3.2B). Increasing only the synaptic strength $S_{12}$, the incoherence $R_p^2$ in

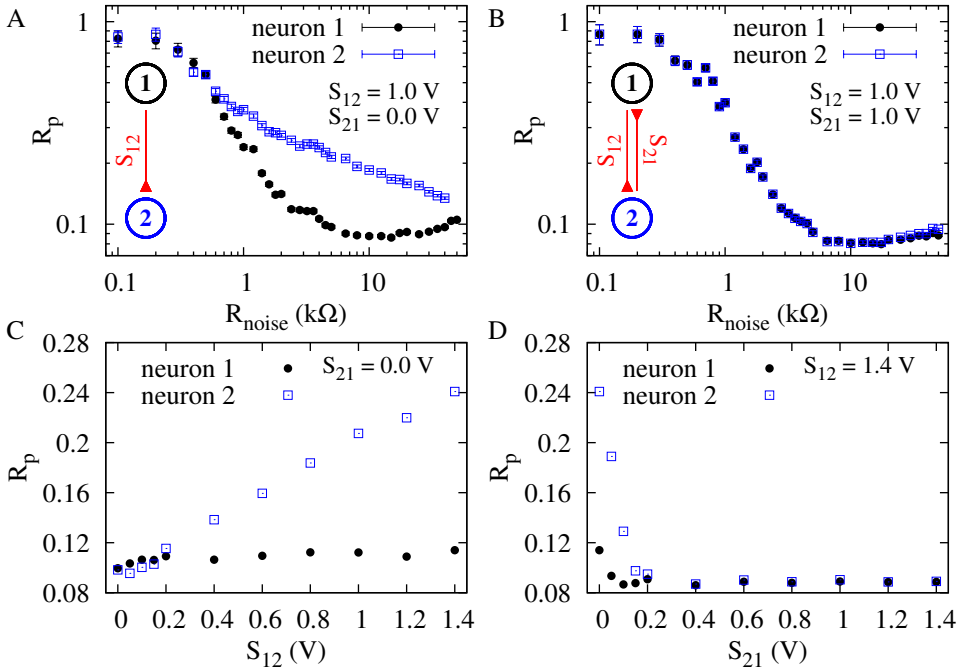


**Figure 3.2** Incoherence parameter $R_p$ as a function of the noise intensity and synaptic amplitudes. (A) Neuron 1 (pre-synaptic) is connected to neuron 2 (post-synaptic) through a synaptic circuit with parameters $R_\alpha = 5$ kΩ, $R_\beta = 20$ kΩ and synaptic amplitude $S_{12} = 1$ V. $R_p^1$ presents a minimum, as expected, but neuron 2 has increased incoherence $R_p^2$. (B) Addition of an identical reciprocal connection leads to a coherence recovery in neuron 2. (C) $R_p^1$ and $R_p^2$ as functions of the synaptic amplitude $S_{12}$ when $S_{21} = 0$ V (unidirectional connection). (D) $R_p^1$ and $R_p^2$ as functions of the synaptic amplitude $S_{21}$ with $S_{12} = 1.4$ V. In (C) and (D), noise is set at the coherence resonance value for a single neuron ($R_{noise} = 10$ kΩ).

the post-synaptic neuron is increased monotonically, while $R_p^1$ remained essentially unchanged (Fig. 3.2C). With $S_{12} = 1.4$ V fixed, we then increased $S_{21}$, which led to a rapid increase in the coherence of neuron 2. Neuron 1, on its turn, showed a small decrease of incoherence (Fig. 3.2D), in a phenomenon similar to what has been reported in numerical simulations of symmetrically coupled neurons [57].

## 3.2 Coherence depends weakly on synaptic symmetry for fast synapses

The above results suggest that symmetry between the synaptic strengths $S_{12}$ and $S_{21}$ plays an important role in the spike train coherence of both neurons. To perform a thorough investigation of this phenomenon, we looked into the dependency of both $R_p^1$ and $R_p^2$ on $S_{12}$ and $S_{21}$ in a large region of the parameter space. In Fig. 3.3A we show the EPSP for both synapses with different synaptic strengths and the corresponding spike times on both neurons when the synaptic time scale are $\tau_{up} = 0.04$ ms and $\tau_{down} = 0.2$ ms (in what follows, $R_\alpha = 5$ kΩ is kept fixed and $\tau$ is controlled only by the resistance $R_\beta$). The dependency of the incoherence parameter $R_p^2$ on the

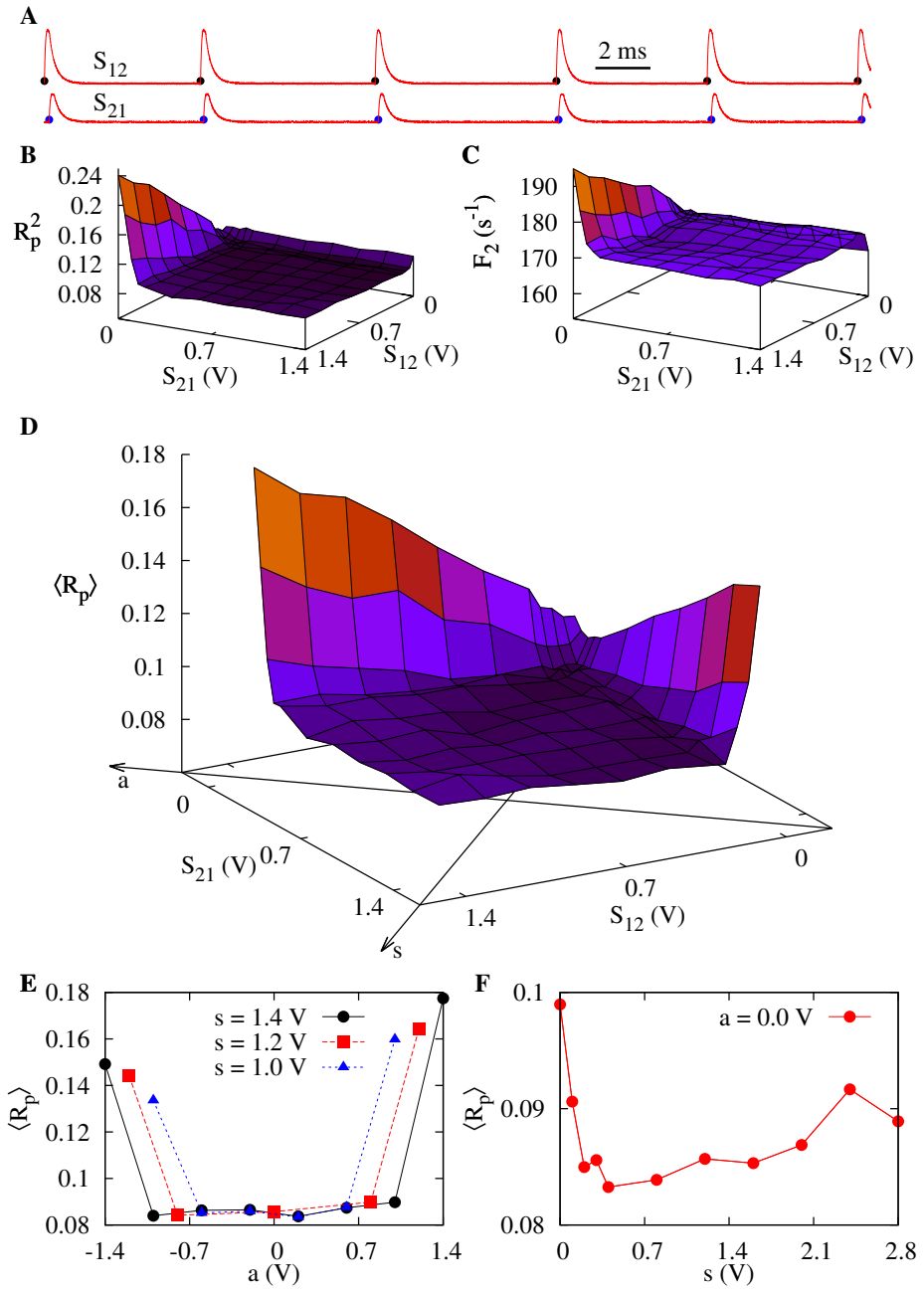


**Figure 3.3** Influence of symmetry on CR for fast synapses. Noise intensities are set at the coherence resonance value ($R_{noise} = 10$ kΩ) for each neuron. Synaptic parameters are $R_\beta = 20$ kΩ and $\tau_{up} = 0.04$ ms and $\tau_{down} = 0.2$ ms. (A) Time series showing spike times for neuron 1 (black dots) and neuron 2 (blue dots) as well as the EPSP of the synapse connecting neuron 1 to neuron 2 with $S_{12} = 0.4$ V and the reverse synapse with $S_{21} = 0.2$ V. (B) Incoherence $R_p^2$ of neuron 2 as a function of both synaptic strengths. (C) Firing rate of neuron 2 as a function of the synaptic strengths. In (B) and (C) $R_p^1$ and $F_1$ behave similarly if the indexes 1 and 2 are reversed. (D) Mean network incoherence $\langle R_p \rangle$ vs $S_{12}$ and $S_{21}$. The symmetry and asymmetry axes are drawn on the horizontal plane. (E) $\langle R_p \rangle$ vs the asymmetry parameter $a$. (F) $\langle R_p \rangle$ vs the symmetry parameter $s$.

synaptic strengths is shown in Fig. 3.3B (of which Figs. 3.2C and 3.2D are cross-sections). The firing rate of neuron 2 was also measured as a function of the synaptic strengths and is shown on Fig. 3.3C. Note that in this case an increase in the excitatory synapse (with strength $S_{21}$) from neuron 2 induces a decrease in its own firing rate, which leads to an increase in the spike train coherence. The parameters $R_p^1$ and $F_1$ for neuron 1 behave in the same way if the indexes 1 and 2 are exchanged.

The total effect of the synaptic coupling on the system can be measured if we define the mean incoherence parameter:

$$\langle R_p \rangle = (R_p^1 + R_p^2)/2. \tag{3.1}$$

We show its dependence on $S_{12}$ and $S_{21}$ in Fig. 3.3D. This graph suggests that the incoherence parameter can be described as a function of symmetry and asymmetry parameters, $s$ and $a$ respectively, defined as:

$$s = S_{12} + S_{21}, \tag{3.2a}$$
$$a = S_{12} - S_{21}. \tag{3.2b}$$

The $s$ and $a$ axes are also shown in Fig. 3.3D. Although for large values of $|a|$ an increase in $\langle R_p \rangle$ is observed, there is a large flat region in which no significant change in coherence is observed. The larger the symmetry $s$, the larger the flat region along the $a$ axis (Fig. 3.3E). For fixed asymmetry $a$, increasing $s$ causes an increase in the system coherence, as shown Figure 3.3F.

## 3.3 Coherence depends strongly on synaptic symmetry for slow synapses

The flat region in Fig. 3.3D might suggest that synaptic symmetry is not so relevant for coherence, after all. This scenario changes significantly, however, when the synaptic time scale increases. Figure 3.4 shows similar results to those of Fig. 3.3, but with $\tau_{up} \simeq 0.048$ ms and $\tau_{down} = 1.0$ ms ($R_\beta = 100$ k$\Omega$). This increase in the value of the synaptic characteristic time, as compared with the previous value, leads to a significant qualitative change in the EPSPs, as shown in Fig. 3.4A.

For these slower synapses, $R_p^2$ now displays a narrow valley of local minima as a function of $S_{12}$ and $S_{21}$ (Fig. 3.4B). If one revisits the situation in which $S_{12} \neq 0$ V and $S_{21}$ is increased from zero, once more an increase in coherence is observed in neuron 2 owing to an outgoing synapse (Fig. 3.4B). Differently from the scenario of the fast synapses (Figs. 3.3B and 3.3C), however, now the increase in the coherence of neuron 2 occurs with an *increase* in its firing rate, as shown in Fig. 3.4C.

The effect of synaptic symmetry on the overall coherence is much more pronounced for slower synapses, as shown in Fig. 3.4D. A much sharper minimum of $\langle R_p \rangle$ emerges near $a = 0$, regardless of the value of $s$ (Fig. 3.4E). Furthermore, for fixed $a = 0$, an increase in symmetry $s$ (which amounts to an increase in overall synaptic strength) leads to an increase in coherence, which attains values above those seen for uncoupled neurons (Fig. 3.4F).

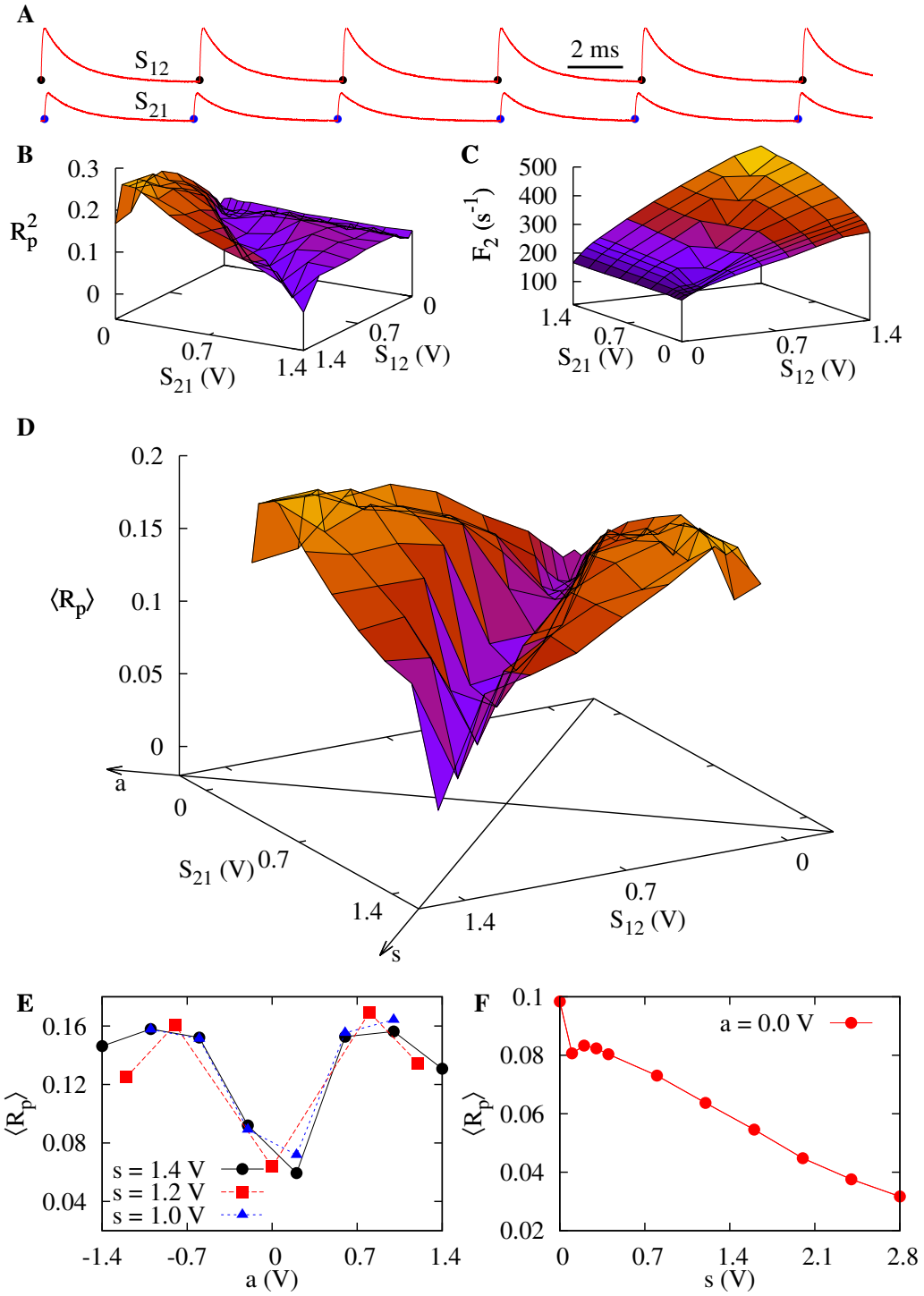


**Figure 3.4** Influence of symmetry on CR for slow synapses. Same as Fig. 3.3, except that synaptic parameters are $R_\beta = 100$ kΩ and $\tau_{up} \simeq 0.048$ ms and $\tau_{down} = 1.0$ ms.

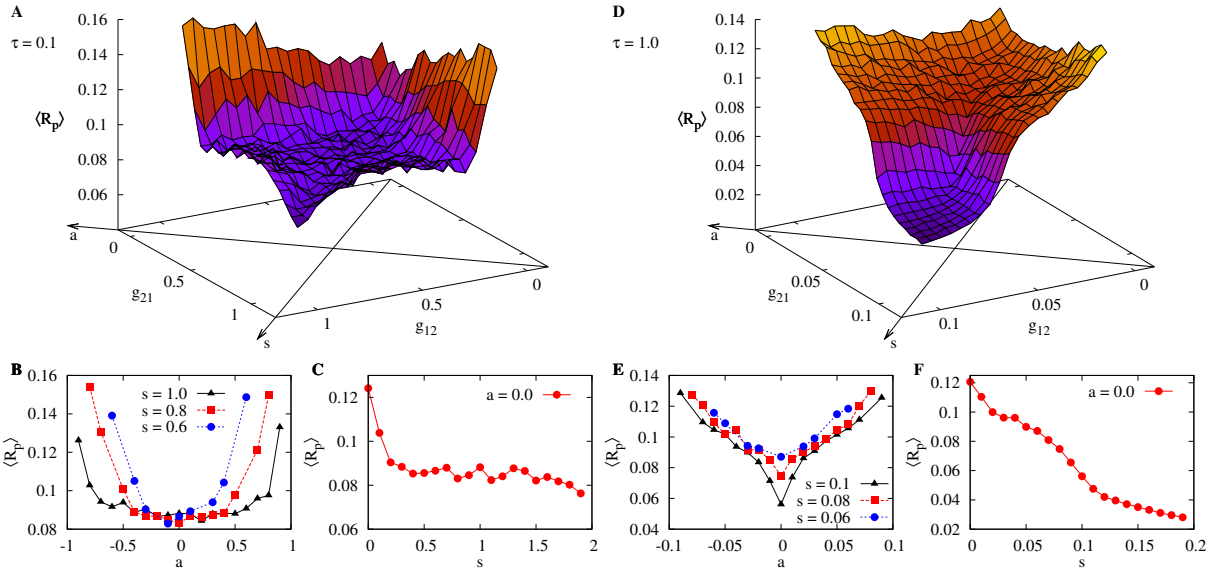


**Figure 3.5** Influence of symmetry on CR for numerical simulations of synaptically coupled FitzHugh-Nagumo models. We have employed $\phi = 0.001$, $\zeta = -1.05$ and $D = 0.03$ in all simulations. For $\tau = 0.1$ (fast synapses): (A) Mean network incoherence $\langle R_p \rangle$ vs $g_{12}$ and $g_{21}$. The symmetry and asymmetry axes are drawn on the horizontal plane. (B) $\langle R_p \rangle$ vs the asymmetry parameter $a$. (C) $\langle R_p \rangle$ vs the symmetry parameter $s$. (D), (E) and (F) are the same as (A), (B) and (C), except that synapses are slower: $\tau = 1.0$.

## 3.4 Comparison with computer simulations

We attempted to reproduce the above results in numerical simulations using the version of the known FitzHugh-Nagumo model we employed before, as described in Eqs. (1.58). This model was chosen due to its simplicity and close similarity with our model for the electronic neuron dynamics. This time, however, to include the coupling between the two model neurons we add to the second equation the effect of the excitatory synapse:

$$\phi \frac{dv}{dt} = v - \frac{v^3}{3} - w \,, \tag{3.3a}$$

$$\frac{dw}{dt} = v - \zeta + D\xi(t) + g v_c, \tag{3.3b}$$

where $\phi = 0.001$ is set to reproduce the ratio of the time scales governing the dynamic variables of the excitable electronic circuits and $\xi$ is an assumed delta-correlated Gaussian noise with zero mean whose intensity is controlled by the parameter $D$. It is important to emphasize that the noisy input $\xi$ is generated independently for each model neuron so that $\xi_1$ for neuron 1 can be assumed uncorrelated with $\xi_2$ for neuron 2. Similarly to Eq. (2.15), the strength of the synaptic coupling between the two model neurons is controlled by the gain constant $g$. The parameter $\zeta = -1.05$ ensures that each FitzHugh-Nagumo model is in a excitable regime but very close to its Hopf bifurcation, which happens at $\zeta = -1.0$, so that the system can fire under the influence of the Gaussian noise input. Coupling between the two FitzHugh-Nagumo systems is achieved using a synaptic model similar to that of the electronic synapse,

as previously described in Eq. 2.14, but instead of two different time scales $\tau_{up}$ and $\tau_{down}$, only one relevant time scale $\tau$ governs the dynamics of the synapse:

$$\frac{dv_c}{dt} = \frac{1}{\tau}\left[0.1\ \Theta(v_{pre}(t))\ v_{pre}(t) - v_c\right] , \tag{3.4}$$

where again $v_c$ integrates pre-synaptic activity $v_{pre}$ only when it is positive. We will employ the gain $g_{ij}$ as a measure of the coupling strength from model neuron $i$ to model neuron $j$.

As in the experiments made with the electronic circuits, the resulting EPSP $gv_C$ generated by a pre-synaptic spike is then added (alongside with the noise) to the variable $\zeta$ of the post-synaptic model neuron. We find the noise intensity that yields the minimum of the incoherence parameter $R_p$ for the uncoupled case ($D = 0.03$) and then vary the synaptic strengths $g_{12}$ (from the model neuron 1 to model neuron 2) and $g_{21}$ (from 2 to 1) measuring the mean incoherence parameter $\langle R_P \rangle$ for each value of the pair $(g_{12}, g_{21})$ as we did with the electronic circuits. Note that the approach here is to measure the synaptic strength directly from the amplification factors $g_{12}$ and $g_{21}$ instead of measuring the amplitude of the EPSPs. The simulations were performed for two different values of the synaptic time scale $\tau$, first for $\tau = 0.1$ (fast synapse) and then for $\tau = 1.0$ (slow synapse). To provide a comparison between these time scales and the time scale that governs the dynamics of both model neurons, the spikes produced have an average duration of 0.5 time units.

The results of the numerical simulations are shown in Fig. 3.5. Comparing first Fig. 3.5A with Fig. 3.3D, we observe that the numerical model corroborates the results of the electronic circuits: with fast synapses, the dependence of the incoherence on the synaptic symmetry is weak. The mean incoherence parameter as a function of the symmetry parameter $s$ and asymmetry parameter $a$ is shown in Fig. 3.5B and Fig. 3.5C and there is good agreement with Fig.3.3E and Fig. 3.3F. Note that in the case of the computer simulations, we employ $a = g_{12} - g_{21}$ and $s = g_{12} + g_{21}$.

Next we increase the synaptic time scale of the model (Fig. 3.5D) and compare the results with those of Fig. 3.4D. Although the shape of the surface obtained through the simulations does not exactly reproduce the one obtained experimentally with the electronic circuits, the dependence of the mean incoherence parameter on $a$ and $s$ keeps its main features for the case of slow synapses: the $\langle R_P \rangle$ dependency on $a$ is sharper than in the case of fast synapses (Fig. 3.5E). It also reaches smaller values when $s$ increases, as compared to faster synapses (Fig. 3.5F).

CHAPTER 4

# Symmetry and coherence effects in two-neuron systems with inhibitory coupling

In the last chapter we have shown that the symmetry in the synaptic strengths in a pair of mutually connected neurons plays an important role on the system coherence. Asymmetric excitatory connections leads to a decrease in the pair coherence while symmetric excitatory connections leads to an increase in coherence, even beyond the point achieved by the uncoupled neurons. Alongside with other mechanisms such as low spacial noise correlations and inhomogeneity across the parameters of the individual network elements [59], excitatory connections have been shown to strengthen system coherence in a number of cases [55, 56, 57, 58, 60].

In the realm of single excitable elements, it was also shown that noise can maximize the spike train incoherence depending on relevant system time scales such as the main activation time and refractory period [61]. In particular, the spike trains in this regime of maximum incoherence can present a intermittent behavior, alternating between a firing and non-firing regime.

Although the subject of coherence resonance had been extensively discussed, the role of inhibitory synapses in network coherence has not, to the best of our knowledge, been addressed. Here we set forth to investigate that role in the simplest case of a pair of mutually connected FitzHugh-Nagumo neuron models. Our main contribution is to show how the interplay between synaptic strength and synaptic characteristic time may lead a system from a state of coherence resonance to another of *incoherence resonance*. More over, we show that symmetry between the synaptic strengths can reinforce either coherence or incoherence of the coupled neurons depending on the synaptic characteristic time.

We follow the same approach of the last chapter, running computer simulations of a pair of FitzHugh-Nagumo model neurons with dynamics described in Eqs. (3.3) with $\phi = 0.001$ and with independent noisy inputs. These model neurons are coupled in the same way employed in the computer simulations of last chapter, using the output $gv_c$ as the post-synaptic potential induced by spikes in the pre-synaptic model neuron. The dynamics of $v_c$ follows from Eq. (3.4). The difference from the previous case is the coupling parameter g, here chosen to assume only negative values. Despite that fact, we will refer to $|g|$ as synaptic strength. Again, the gain $g_{ij}$ will denote the strength of the coupling strength from model neuron $i$ to model neuron $j$. The use of inhibitory synapses induces very interesting firing patterns in the mutually coupled model neurons, as will be discussed below.

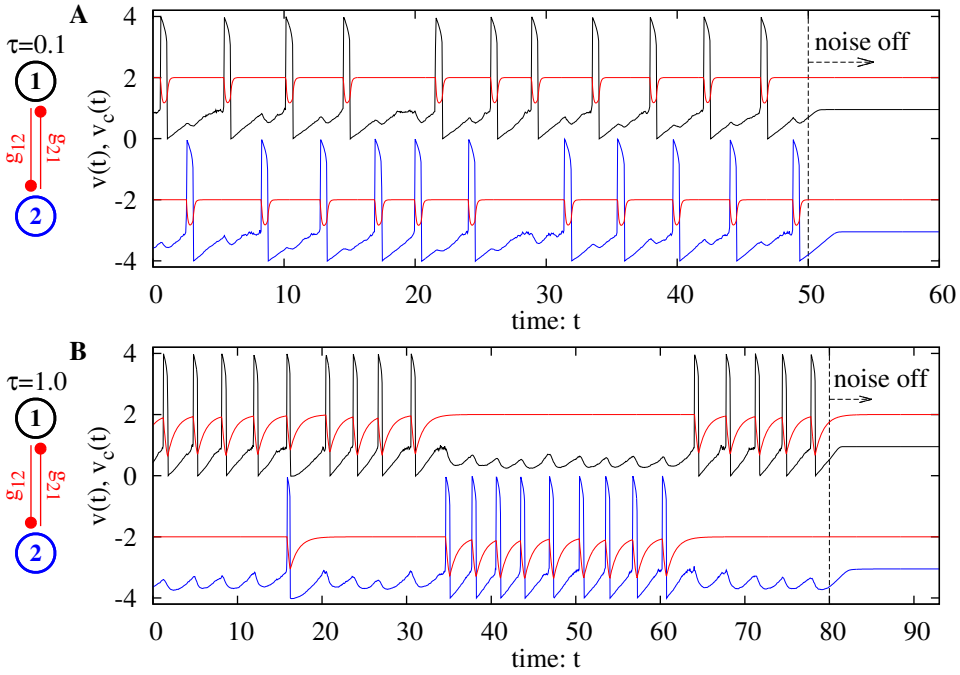


**Figure 4.1** Spike trains of a pair of FN model neurons coupled together with equal strength inhibitory synapses (as described in Eq. 3.4). The noise intensity is $D = 0.03$. (A) Spike train for neuron 1 (black line) and neuron two (blue line) and the inhibitory post-synaptic potentials (IPSP) they impinge on the other neuron, respectively (red lines). The synapses have equal strengths $g_{12} = g_{21} = -0.2$ and characteristic time $\tau = 0.1$. (B) Same as (A), but with $g_{12} = g_{21} = -0.1$ and characteristic time $\tau = 1.0$. For the sake of better visibility of the data, in both graphs the time series of each model neuron and its corresponding IPSP has been shifted vertically 2 units up, for neuron 1, or 2 units down, for neuron 2. Switching off the noisy input (independently for each neuron) leads the system to a rest state regardless of the synaptic coupling strength between the neurons or the synaptic characteristic time.

## 4.1 Inhibitory synapses causes anti-phase or intermittency patterns in the spike trains

The two model neurons are again set near the edge of their Hopf bifurcations with the parameter $\zeta = -1.05$ causing them to have high excitability, i.e. small perturbations around the rest state can easily induce spikes.

In Fig. 4.1A we show the time series of the variable $v(t)$ of two FN model neurons in an excitable regime under the influence of independent noise inputs, both with the same intensity $D = 0.03$. As shown in Fig. 4.2A and C this noise intensity corresponds to the coherence resonance value for an uncoupled FN model neuron, which then would fire in a quasi-periodic fashion with moderate firing rate. The neurons are mutually connected with equal strength synapses ($g_{12} = g_{21} = -0.2$) with same time scale $\tau = 0.1$. The respective inhibitory post-synaptic potentials (IPSPs) produced by each neuron are also shown in Fig. 4.1A. As discussed in Section 3.4, for this value of $\tau$ the synaptic response to the neuronal input is fast: $v_c$ approaches quickly its asymptotic value making the duration of the IPSP comparable to the spike

duration (approximately 0.5 time units). With this setup we observe that the two neurons tends to fire in an approximately alternating way, one after the other. As neuron 1 fires, it inhibits neuron 2. Since neuron 2 would fire at approximately regular rates, his next spike gets delayed for a short time while the IPSP is active. When it finally manages to fire again, it then delays the next spike of neuron 1. The process then repeats itself. This regime is similar to the well known anti-phase synchronization behavior found in the swimming control mechanism of Clione mollusks where a pair of neurons mutually connected with inhibitory synapses generate ongoing periodic oscillations in response to a brief stimulus [44, 62]. Differently from our 2-neuron system, these oscillations are caused by post-inhibitory rebounds, where a hyperpolarization caused by an IPSP induces a spike in the post-synaptic neuron, whereas in our system all spikes are ultimately driven by noise.

If, however, the time scale of the synapses is increased, the two mutually coupled neurons behave in a different way. In Fig. 4.1B, the synaptic time scale of both synapses is now $\tau = 1.0$ (slow synapse) and their strength is $g_{12} = g_{21} = -0.1$. In this case the synapses approach their equilibrium values in a slower fashion, remaining active for periods longer than the spike duration, effectively creating a stronger inhibition even though the value of the coupling strengths is lower than it was in the previous case. This creates an intermittency of the spike trains, where the firing activity in one of the neurons almost inhibits the other completely. This kind of behavior was reported in single excitable elements driven by noise [63, 64]. The transitions from the firing state to the non-firing state within each neuron are due to large noise fluctuations capable of overcoming the influence of the arriving IPSPs.

For both values or $\tau$, i.e. for fast and slow synapses, switching off the noise input in both neurons ceases the system activity regardless of the synaptic coupling strength, since each FN neuron now rests at their respective stable fixed point. This is demonstrated near the end of the time series pictured in Figs. 4.1A and B, and it shows that the two-neuron system is not in a self-sustained activity state.

## 4.2 Inhibitory synapses can improve or deteriorate coherence

To understand how the transition from anti-phase synchronization-like to intermittent behavior occurs we go one step back to the simpler case of a two-neuron system where there is only one inhibitory synapse. Figure 4.2A shows the incoherence parameter $R_p$, as defined by Eq. (1.53), as a function of the noise intensity $D$ for each of the two FN neuron models, labeled 1 and 2. Since neuron 1 acts as the pre-synaptic neuron and is effectively isolated from neuron 2 ($g_{21} = 0$, meaning no incoming connections), $R_p^1$ presents a minimum as a function of the noise intensity, in a way that is characteristic of CR. The fast inhibitory synapse from neuron 1 to neuron 2 ($g_{12} = -0.5$, $\tau = 0.1$) causes the spike trains of neuron 2 to be, for a given value of $D$, less coherent than those of neuron 1 ($R_p^2$ is in general greater than $R_p^1$). That is to be expected since the noise-induced IPSPs from neuron 1 prevent some of the also noise-induced spikes of neuron 2 from happening, contributing to a more irregular spike train on neuron 2.

If the inhibitory loop is then closed with a synapse of same strength and time scale ($g_{21} = -0.5$, $\tau = 0.1$) as shown in Fig. 4.2B, the loss of coherence in neuron 2 is partially reverted, rendering the spike trains of neuron 2 almost as coherent as it would be if it was uncoupled. We

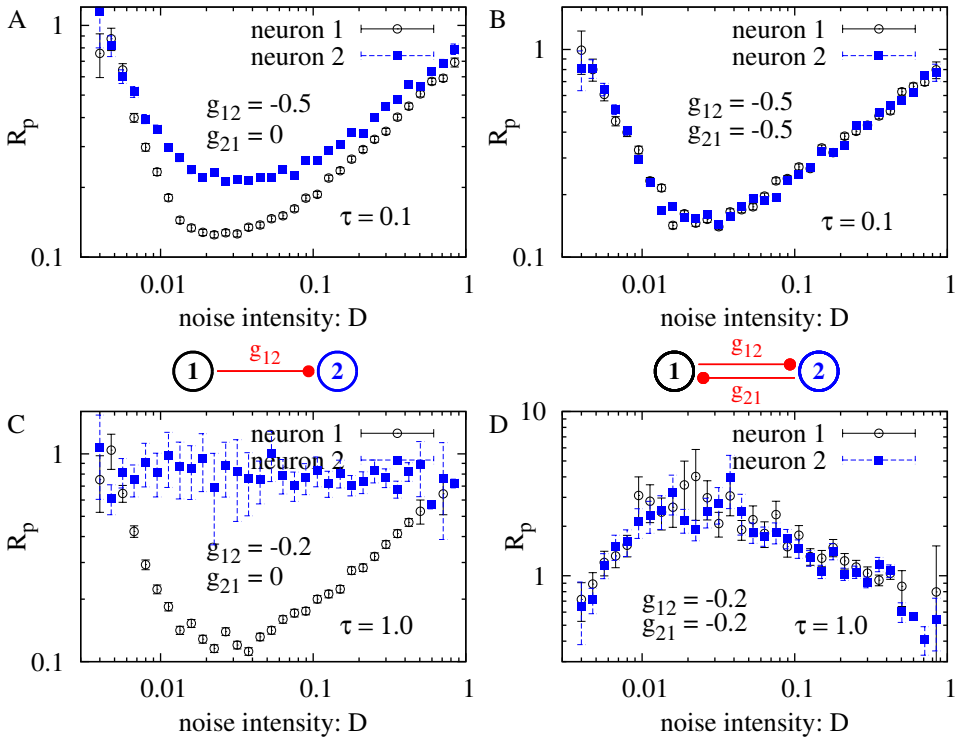


**Figure 4.2** Incoherence parameter $R_P$ for a pair of FN model as a function of noise intensity and synaptic strengths. (A) Neuron 1 is connected unidirectionally to neuron 1 with a fast inhibitory synapse ($\tau = 0.1$) with coupling strength $g12 = -0.5$. Neuron 1 is unaffected by neuron 2 and displays a coherence resonance curve as expected. Neuron 2 spike trains, however, for any given noise intensity $D$, become less coherent. (B) Adding inhibitory synapse of same strength and characteristic time in the reverse direction (from neuron 2 to neuron 1) while keeping the previous connection partially reverts the decrease in coherence suffered by neuron 2, but also induces a decrease in coherence in neuron 1. (C) Same as (A) but neuron 1 is connected to neuron 2 with a slow synapse ($\tau = 1.0$) with synaptic strength $g_{12} = -0.2$. The incoherence increase in the spike trains of neuron 2 is more pronounced with a slow synapse. (D) Same as (B). Adding a slow synapse in the reverse direction with same strength leads to very incoherent spike trains for both neurons, and effectively to an incoherence resonance behavior.

also note that there is a slight overall increase in the incoherence parameter for neuron 1 (around 10%). In this set up, the neurons tend to fire in a regime that approaches that of Fig. 4.1A as the noise intensity becomes closer to the coherence resonance value ($D \simeq 0.03$) for uncoupled neurons. For smaller noise intensities the spike trains of both neurons have small firing rates and Poisson-like interspike distribution, therefore the inhibitory synapses do not affect greatly the firing patterns of both neurons. For noise intensities larger than the resonance value the anti-phase synchronization-like behavior tends to break due to the increasingly frequent noise induced spikes. This result is similar to what we presented in the last chapter for fast excitatory synapses, although the coherence recovery achieved in that case was strong enough to leave the spike trains of both neurons more coherent than they would be if they were uncoupled.

The coherence of the two-neuron system changes dramatically if the time scale $\tau$ of the synapses is increased. In Fig. 4.2C we show the $R_p$ vs $D$ curve for both neurons, each receiving

independent noise inputs of same intensity while only neuron 1 connects to neuron 2 via a slow inhibitory synapse ($g_{12} = -0.2$, $\tau = 1.0$). With the increased IPSP duration, neuron 2 is inhibited most of the time, firing only when the noise input is large enough to overcome such inhibition. This causes the spike trains of neuron 2 to have approximately poissonian interspike distributions, regardless of the intensity of the noise stimulus. The coherence curve of neuron 1 is, again, unaffected since it is effectively isolated from neuron 2 ($g_{21} = 0$). Adding an equal inhibitory synapse in the reverse direction while keeping the first one causes the spike trains of both neurons to become highly incoherent (Fig. 4.2D). They both present a *maximum* in the incoherence parameter $R_P$ as function of the noise intensity $D$ at the same value of $D$ that produces coherence resonance in uncoupled neurons. In this regime, the neurons tend to fire in the way presented in Fig. 4.1B when the $D$ approaches the resonance value. While one of the neurons is firing the other is almost completely inhibited due to the long period of action of the arriving IPSP, allowing the firing neuron to act as if it was uncoupled. This happens until a large noise fluctuation causes the inhibited neuron to fire once, which then proceeds to cause a long standing inhibition in the previously firing neuron, sending it to a non-firing state until another large noise induced spike happens, repeating the process. For small noise intensities both neurons have small firing rates, therefore causing their spike trains to approach a poissonian behavior since they are less affected by the lengthy inhibition periods. For larger values of $D$ the transitions between the firing and non-firing states are more frequent, so that the non-firing states in each neuron do not last long, reducing the effect that the intermittent behavior has on the incoherence parameter $R_p$. From Figure 4.2D we see that high values of the incoherence parameter $R_p$ might be considered as a signature of neuronal intermittent firing behavior.

It is clear from the last figures that there are two important parameters to be considered when trying to understand how the two model neurons undergo a transition from coherence to incoherence resonance. One of them is the synaptic strengths $g_{12}$ and $g_{21}$ and the other is the characteristic time $\tau$ of the synapses. In what follows we study the interplay between these two parameters, starting with the synaptic strengths. Unless otherwise stated along the text, from hereon the input noise intensity for both neurons is fixed at the coherence resonance value found for an uncoupled FN model neuron ($D = 0.03$). This choice was made to better illustrate the changes in the two-neuron system behavior, as they are more pronounced at this value of noise intensity.

## 4.3 Coherence dependence on synaptic symmetry for fast synapses

In Fig. 4.3A we show the spike timings for a pair of FN neurons coupled with inhibitory synapses alongside with the corresponding IPSPs produced by fast synapses ($\tau = 0.1$). Here we deviate from the case where the inhibitory synapses had equal strengths causing a weakening in the tendency the neurons have to fire in succession, one after the other, as shown in Fig 4.1A. In Fig. 4.3B, the full effect of the synaptic symmetry (i.e. how similar the strengths of both synapses are) on the coherence of neuron 1 can be observed. Here we plot the incoherence parameter $R_p^1$ of neuron 1 as a function of $g_{12}$ and $g_{21}$. The decrease in coherence induced by the incoming connection from neuron 2 (with strength $|g_{21}|$) and then the coherence recovery

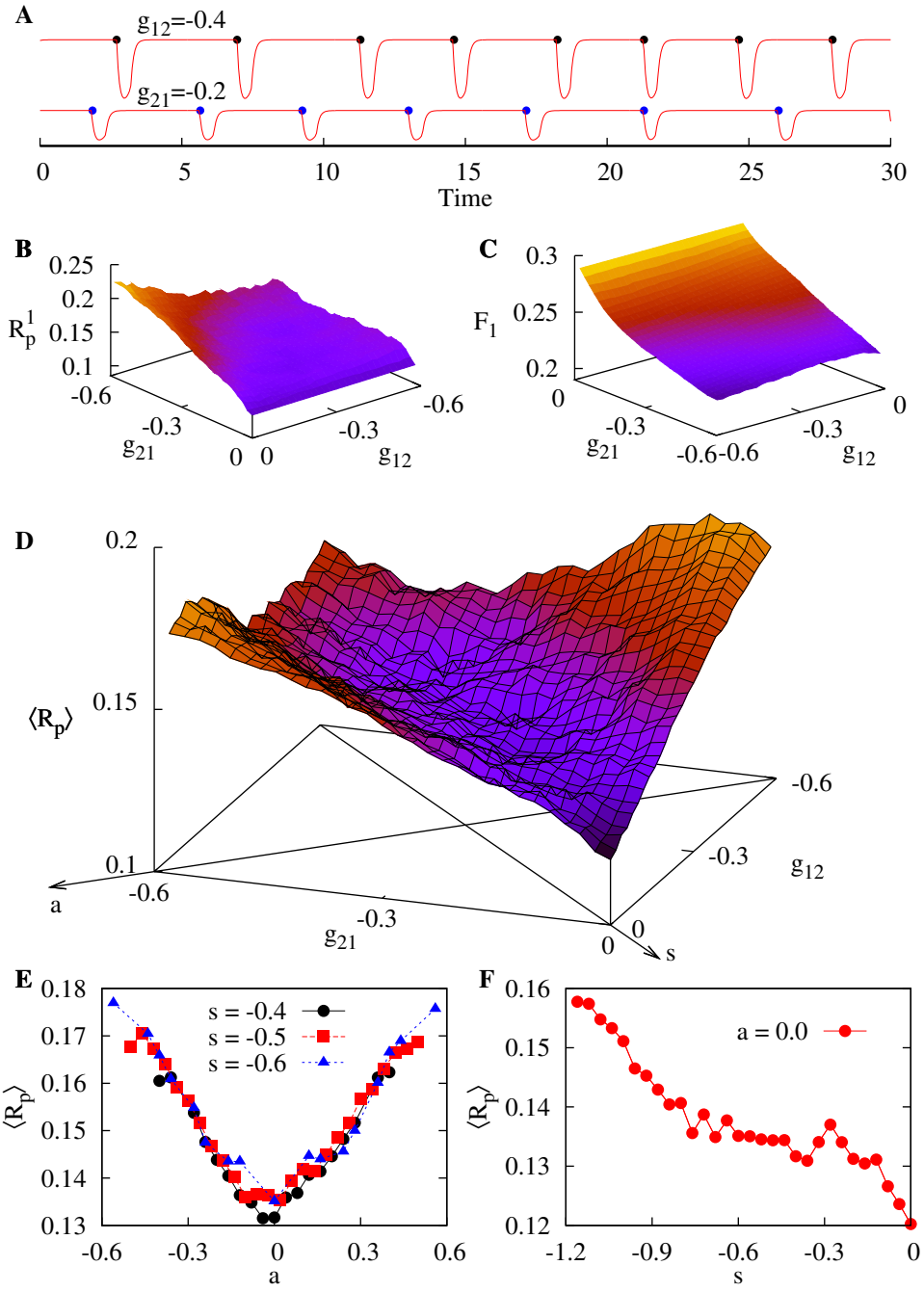


**Figure 4.3** Incoherence parameter as a function of the synaptic strengths for fast synapses ($\tau = 0.1$). Noise intensities for each neuron are set at the coherence resonance value for an uncoupled FN model neuron ($D = 0.03$). (A) Time series showing spike times for neuron 1 (black dots) and neuron 2 (blue dots) as well as the IPSPs of the synapses connecting neuron 1 to neuron 2 with $g = -0.4$ and the reverse synapse connecting neuron 2 to neuron 1 with $g = -0.2$ (red lines). (B) Incoherence parameter $R_P$ and (C) Firing rate $F_1$ of neuron 1 as a function of the synaptic strengths. (D) Mean network incoherence $\langle R_P \rangle$ vs $g_{12}$ and $g_{21}$ with symmetry and asymmetry axes drawn on the horizontal plane. (E) $\langle R_P \rangle$ as function of the asymmetry parameter $a$. (F) $\langle R_P \rangle$ vs the symmetry parameter $s$.

due to the outgoing synapse from neuron 1 to neuron 2 (with strength $|g_{12}|$) that was displayed in Figs. 4.2A and B is also depicted here as cross-sections of the surface shown. In Fig. 4.3C the effect of the inhibitory connections on the firing rate $F_1$ of neuron 1 is shown. Firing rates measures are done by simply counting the number of spikes in a time series and dividing by its length. As expected, increasing the synaptic strength $|g_{12}|$ (from neuron 1 to neuron 2) while keeping $|g_{21}|$ constant does not affect the how neuron 1 fires. On the other hand, increasing $|g_{21}|$ induces a decrease in $F_1$, as expected from a neuron receiving increasing inhibition.

An evaluation of the total effect of the synaptic coupling on the system can be made in terms of the mean incoherence parameter defined in Eq. (3.1). In Fig 4.3D we show how this parameter depends on both synaptic strengths. The symmetrical nature of the surface with respect to changes between the indices 1 and 2 of the synaptic strengths $g_{12}$ and $g_{21}$ is better highlighted as a function of the symmetry and asymmetry parameters, $s$ and $a$ (axes also shown in Fig 4.3D), defined in Eqs. (3.2). We observe that for small values of $a$ (synapses with similar strengths) the system is more coherent state than it would be if the synapses had strengths that lacked symmetry (Fig. 4.3E). This is similar to the result previously reported in Sections 3.2 and 3.4 for excitatory synapses with small characteristic time scales. On the other hand, for a fixed asymmetry value $a$, decreasing $s$, which amounts to an increase in the overall synaptic strength, slightly increases the system incoherence (Fig. 4.3F) in contrast with what is expected from excitatory synapses.

## 4.4 Coherence dependence on synaptic symmetry for slow synapses

The same analysis can be performed for slower synapses, and, as hinted by Figs. 4.2C and D, the behavior of the system is drastically different. In Fig. 4.4A we show the spike timings for two neurons coupled with inhibitory synapses that have a long characteristic time ($\tau = 1.0$) alongside with the IPSPs each synapse generates. The behavior of the spike trains is similar to that shown in Fig. 4.1B where there is an intermittent regime, alternating between a firing and non-firing states with transitions between such states being induced by the (independent) noise inputs each neuron receive.

In Fig. 4.4B the incoherence parameter $R_P^1$ for neuron 1 is shown as a function of both synaptic strengths. The increase in the incoherence parameter due to an incoming inhibitory synapse with strength $|g_{21}|$ and the further increase in $R_P^1$ caused by the outgoing synapse with strength $|g_{12}|$ shown in Fig. 4.2C and D is again shown here are as cross-sections of the surface in Fig. 4.4B. In Fig. 4.4C we show the firing rate $F_1$ of neuron 1. Due to the long synaptic duration, in contrast to what happens in the previous case with $\tau = 0.1$, $F_1$ increases significantly if the outgoing synaptic strength $|g_{12}|$ is increased. The inhibition caused by neuron 1 on neuron 2 reduces the firing rate $F_2$ of neuron 2 effectively reducing the number of IPSPs neuron 1 receives from neuron 2, therefore increasing $F_1$.

Again, using the mean incoherence as defined in Eq. (3.1), we show in Fig. 4.4D that the system is invariant if the subscripts 1 and 2 of each neuron or synapse strength are interchanged. Instead of a valley along the symmetry axis $s$ as in the previous case, Figs. 4.4D and F shows that the system is more incoherent for smaller values of the symmetry parameter $s$ (stronger synaptic strength). According to Fig. 4.4E, the mean system incoherence also shows

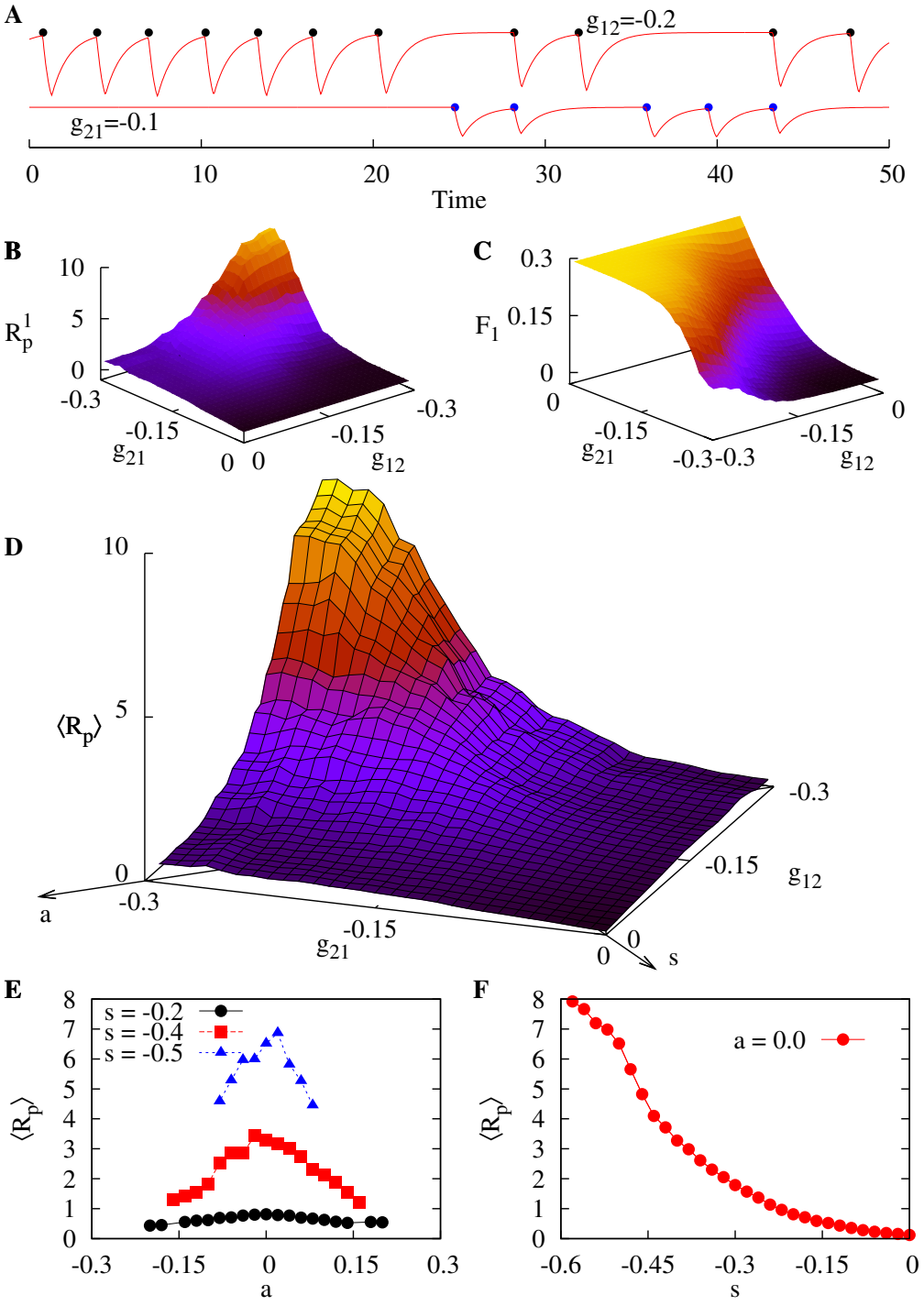


**Figure 4.4** Incoherence parameter as a function of the synaptic strengths for slow synapses. Same as Fig.4.3 except that the synaptic characteristic time is $\tau = 1.0$.

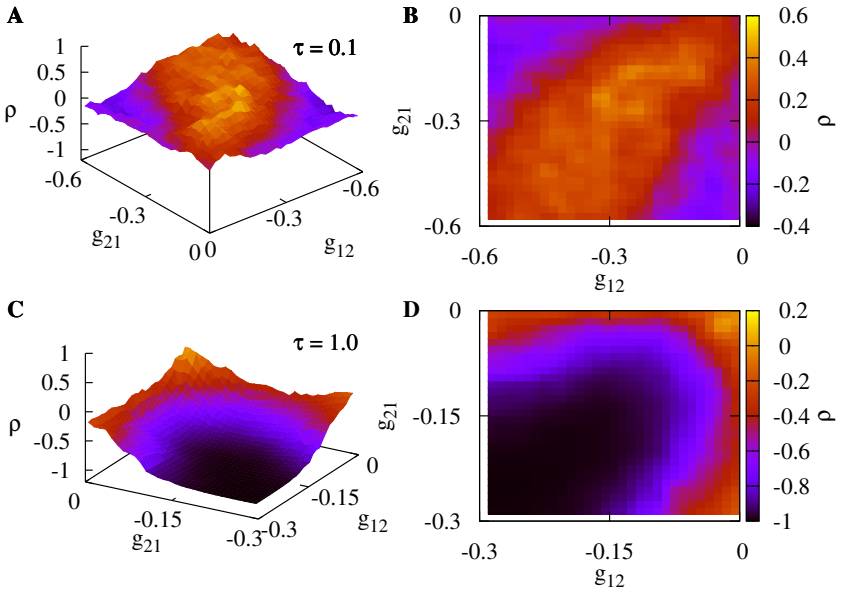


**Figure 4.5** Firing rate Pearson correlation function as a function of the synaptic strengths. The firing rates of each neuron are measured inside 40 time units windows in a 1200 time units long time series. (A) Correlation between the firing rates of neuron 1 and 2 for fast synapses ($\tau = 0.1$). (B) Heat map of the surface shown in (A). (C) and (D) Same as (A) and (B) but for slow synapses ($\tau = 1.0$).

a maximum as function of the asymmetry parameter $a$ at the value $a = 0$ (synapses with equal strengths) where in the previous case a minimum was observed (Fig. 4.3E). It is clear that the system undergoes a transition controlled by the characteristic time $\tau$ of the synapses, moving from a coherent state near $a = 0$ to a very incoherent state.

## 4.5 Firing rate correlation and transition from coherence resonance to incoherence resonance

To obtain more information about the influence of the characteristic times on the spike train coherence we turn our attention to the correlation between the firing rates of both neurons, measured as a function of the synaptic strengths. We employ the Pearson correlation coefficient as defined below:

$$\rho = \frac{\sum_{i=1}^{N}(F_{1i} - \bar{F}_1)(F_{2i} - \bar{F}_2)}{\sqrt{\sum_{i=1}^{N}(F_{1i} - \bar{F}_1)^2}\sqrt{\sum_{i=1}^{N}(F_{2i} - \bar{F}_2)^2}}, \tag{4.1}$$

which is simply the covariance of the two firing rates divided by the their standard deviations. The Pearson coefficient can assume values between (and including) $-1$ to 1. To calculate $\rho$ we divided a long time series of spike trains (12000 time units for each neuron) in $N = 300$ sub-intervals (40 time units each) and then evaluated the firing rates $F_{1i}$ and $F_{2i}$ for neuron 1 and 2, respectively, in each of these sub-intervals. $\bar{F}_1$ and $\bar{F}_2$ corresponds to the mean firing rate of neuron 1 and 2 over those sub-interval. In Figs. 4.5A and B we show $\rho$ as function of both

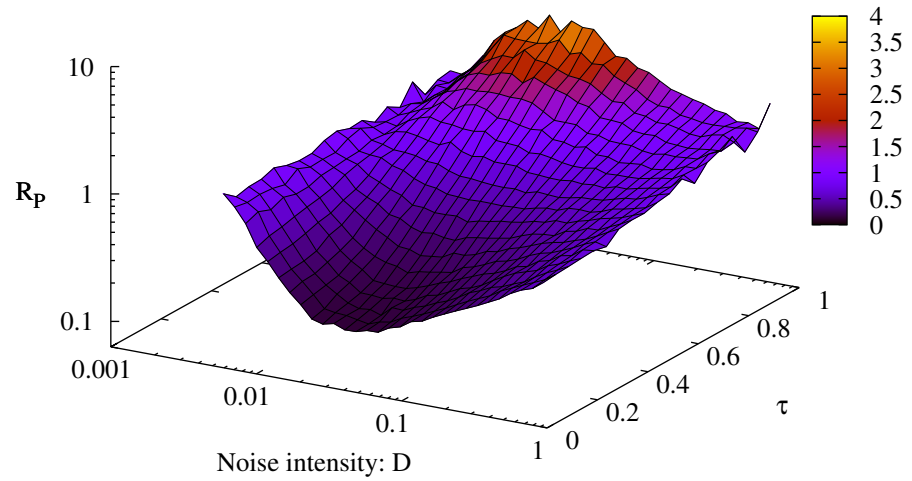


**Figure 4.6** Incoherence parameter of neuron 1 as function of noise intensity and the synaptic time scale. The synaptic strengths were kept constant at the value $g_{12} = g_{21} = -0.2$. The neuron undergoes a transition from coherence resonance to incoherence resonance as $\tau$ is increased.

synaptic strengths for fast synapses ($\tau = 0.1$). In this regime the firing rates of both neurons tend to follow each other when the synapses have similar strengths ($a \simeq 0$), corresponding to the region of small positive correlation. As shown before, this leads to the anti-phase synchronization like state. If the synapses, however, are highly non-symmetric, the firing rates become negatively correlated, meaning that higher firing rates in one of the neurons forces the other neuron to face more inhibition from the incoming IPSPs, which then reduces its firing rate.

For slow synapses, the firing rates of both neurons have a very strong tendency be negatively correlated, as shown in Figs. 4.5C and D. Again, the interesting region is the one where the synapses have similar strengths ($a \simeq 0$), which presents stronger negative correlations with values close to $-1$. This corresponds to strong mutual inhibition, leading to the intermittent spiking behavior presented in Fig. 4.1B and Fig. 4.4A. Highly asymmetric synapses produce small negative correlations between the firing rates, which corresponds to one of the model neurons inducing very small firing rates on the other due to its strong and lasting inhibition. For both characteristic times the correlation coefficient is close to zero when $g_{12} \simeq g_{21} \simeq 0$.

So far we have kept the input noise intensities constant at the value of the of coherence resonance of an uncoupled FN model neuron ($D = 0.03$). To give a complete picture of the effect of the change in the characteristic time $\tau$ of the synapses, in Fig. 4.6 we allow the input noise intensity in each neuron to vary in the same way presented in Fig. 4.2 while the synaptic strengths are kept constant at the value $g_{12} = g_{21} = -0.2$. This choice of symmetric synaptic strengths highlights the transition from a state of high (maximum) to a state or low (minimum) coherence as shown in Figs 4.3E and 4.4E. For small values of $\tau$ (fast synapses) the system presents coherence resonance, while for large enough values of $\tau$ the system to gradually loses coherence, resulting in incoherence resonance.

CHAPTER 5

# Dynamic range of networks of electronic neurons

In this chapter we focus our attention on the problem of the dynamic range of networks constructed with the electronic circuits discussed in the previous chapters: the excitable electronic circuit and the electronic synapse. Our motivation lies in the phenomenon where a large dynamic arises from coupled excitable elements, each of them with small dynamic range. Furthermore, this effect is maximized at a critical point, which is determined by the coupling strength between the elements. The dynamic range increase has been discussed in a number of works with the use of the simple $n$-state Greenberg-Hastings cellular automaton model [20, 33, 35], although only more recently the mechanism governing the dynamic range maximization at a critical point was explained [29]. Here we present a short description of this model, which provided a guideline for the measurement methods used to obtain the dynamic range of our electronic networks.

The $n$ states of each cellular automaton of reference [29] were chosen in order to mimic the behavior of excitable elements: the state $n = 0$ represents the rest state, $n = 1$ the excited state (spike) and the following $n-2$ states corresponding to the refractory period. A total of $N$ cellular automata were connected together in a Erdős-Rényi undirected random graph with mean connectivity $K$ and connection distribution given by an binomial distribution. The network was subjected to an external excitatory stimulus with intensity given by the rate $r$ of a Poisson process. Also each element can receive an excitatory input from its neighbors.

An automaton $i$ makes a transition from the rest state $n = 0$ to the excitable state $n = 1$ when either an external stimulus or an input from an neighbor in the excited state arrives, the former with probability $\lambda = 1 - e^{(-r\Delta t)}$ per time step $\Delta t = 1$ ms, and the later with probability $p_{ij}$ randomly drawn from a uniform distribution in the interval $[0, p_{max}]$. The coupling strength is effectively given by the probability $p_{ij}$, which is symmetrical, i.e. $p_{ij} = p_{ji}$, therefore making the connections similar to electrical synapses. Gap junctions have been shown to play an important role in dynamic range enhancement of biologically detailed models of vertebrate retina [65].

In the cellular automaton model the relevant control parameter of the network response is the average branching ratio $\sigma = \langle \sigma_i \rangle$, where $\sigma_i = \Sigma_j^{K_i} p_{ji}$, the local branching ratio, measures the mean number of excitations induced by the element $i$ in its neighborhood $K_i$. Since each local branching ratio $\sigma_i$ has an average value $K_i p_{max}/2$ and the $K_i$s follow a binomial distribution with mean equal to $K$, then $\sigma = K p_{max}/2$. Therefore the mean branching ratio sets the maximum value $p_{max}$ for the coupling strengths, which increases or decreases the overall network excitability to excitatory stimuli generated by elements inside the network. Theoretical works on this subject have shown that the average branching ratio is not the main control parameter for networks of different topologies, which is then defined as the largest eigenvalue of the

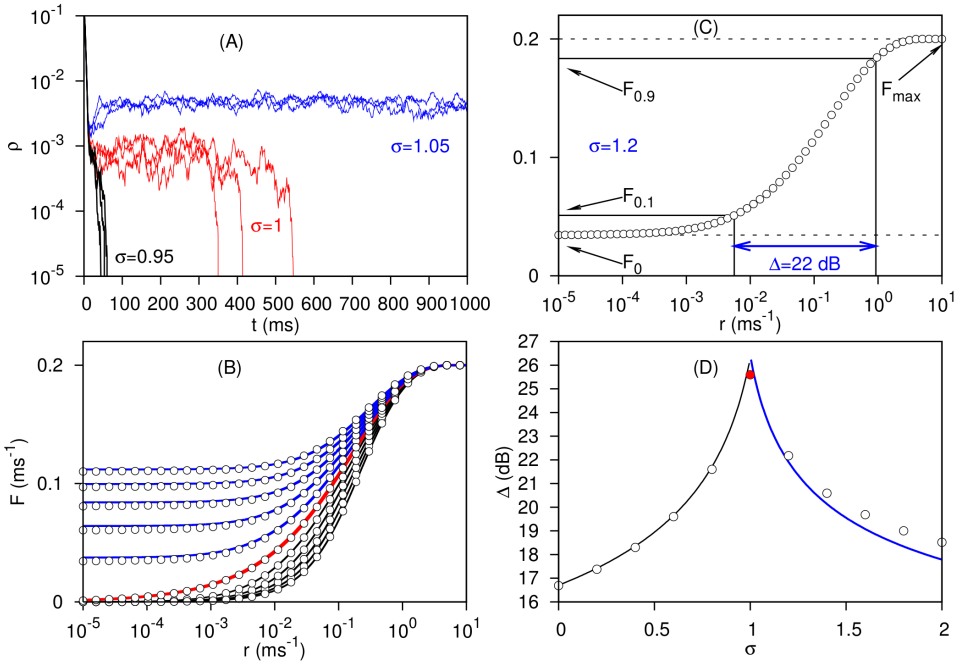


**Figure 5.1** Dynamic range measurements of a cellular automaton Erdős-Rényi network with $N = 10^5$ elements. (A) Instantaneous density of active network elements in the subcritical (black), critical (red) and supercritical (blue) regimes when the network initially has 10% of its sites active. For each regime, three "runs" of the system are shown. (B) Response curves showing $F$ as a function of the external stimulus intensity $r$ for different values of the mean branching ratio, with increments of 0.2. (C) Relevant parameters for the calculation of $\Delta$ from a response curve. Note that in the supercritical regime, the system has a non-zero baseline activity $F_0$. (D) Dynamic range $\Delta$ as function of the mean branching ratio $\sigma$. $\Delta$ is maximized at the critical value $\sigma_c = 1$. (Adapted from Kinouchi and Copelli (2006) [29]).

"weighted adjacency matrix" $P_{ij}$ of the network, with $\sigma$ being just a particular case for random Erdős-Rényi networks [66]. Regardless, this control parameter is still related to how strong the network connections are.

The network activity $F$ was measured by the mean density of active cellular automata, i.e an average over time of the number of elements at the state $n = 1$ divided by the total number of elements, which is equivalent to a mean network firing rate. The network response to external stimuli depends on the coupling strength, with short-lived activity for small mean branching ratio and self-sustained activity, even in the absence of external stimuli, for large $\sigma$. A transition between these two scenarios happens at the critical value $\sigma = \sigma_c = 1$, that is, when one spike generates, on average, only one spike in its entire neighborhood. The activity duration at the critical point has a large variance, with the number of elements participating in each activity burst, or avalanche, following a power law distribution. These three regimes are shown in Fig. 5.1A when the network is set to have 10% of its elements starting at the excited state ($n = 1$).

The dynamic range $\Delta$ of the network is measured from its response curves, i.e. from the mean activity $F$ as a function of the external stimulus intensity $r$, shown in Fig. 5.1B for in-

creasing values of the mean branching parameter, varying from the subcritical regime ($\sigma < \sigma_c$) to the supercritical regime ($\sigma > \sigma_c$). The dynamic range is defined in a similar way to what we previously defined in Eq. (1.56) for the response curve of a single excitable electronic neuron:

$$\Delta = 10\log_{10}\left(\frac{r_{0.9}}{r_{0.1}}\right), \tag{5.1}$$

where the range $[r_{0.1}, r_{0.9}]$ is chosen from the corresponding response interval $[F_{0.1}, F_{0.9}]$ defined by Eq. (5.2). Differently from Eq. (1.57), where $F_0$ was always zero, here the supercritical regime allows for self-sustained activity, therefore causing $F_0$ to assume a non-zero value. The response interval is given by:

$$F_x = F_0 + x(F_{max} - F_0) \qquad (0 \leq x \leq 1)\,. \tag{5.2}$$

These parameters are shown in Fig. 5.1C for a supercritical response curve ($\sigma = 1.2$). The system displays its critical behavior when the mean network connectivity is varied by changing the control parameter $\sigma$. As shown in Fig. 5.1D, the maximum dynamic range is attained exactly at the point $\sigma_c = 1$ where the network response changes from short-lived oscillations to a self-sustained regime. The increased connectivity of networks close, but below, the critical point allows for better perception of low intensity stimuli, while the onset of self-sustained activity in the supercritical regime masks this kind of stimuli, therefore reducing the network dynamic range. This result, which have been confirmed recently in a biological system, for instance in rat cortex slice cultures [67], as pointed before could have a direct application in the construction of biologically-inspired sensors with high sensibility and large dynamic range. For the remainder of this chapter we put this hypothesis to test employing our electronic circuits in the architecture of networks, aiming for a proof of concept version of such sensor.

## 5.1 Experimental setup and its differences from the cellular automaton model

To measure dynamic ranges in networks of many excitable elements, we first took advantage of the simplicity of our electronic circuits and designed a single small printed circuit module board containing all the elements from which the dynamics of an excitable element is derived. For instance, the excitable electronic circuit shown in Fig. 1.16, a dedicated noise generator circuit shown in Fig 3.1 and the synaptic circuit shown in Fig. 2.6. The module board is shown in Fig. 5.2A with a pen for size comparison. Figure 5.2B shows the reverse side of the board with all the welded electronic components. The region each individual board submodule, i.e. the excitable circuit, its noise generator and the electronic synapse, occupies on the board is also shown. The use of surface-mounted devices (SMD) instead of standard electronic components allows all three circuits to be compactly set on smaller dimensions. The module board has built in an analog circuit for subtracting the dynamic variables of the excitable circuit, resulting in an output voltage $V_{pre}$, and an analog circuit for adding up all the inputs coming to the excitable circuit, e.g. the DC input $V_{DC}$, the noisy input $V_{noise}$ and any number of synaptic inputs $V_S$ coming from other modules. It also allows setting the noise intensity (measured as

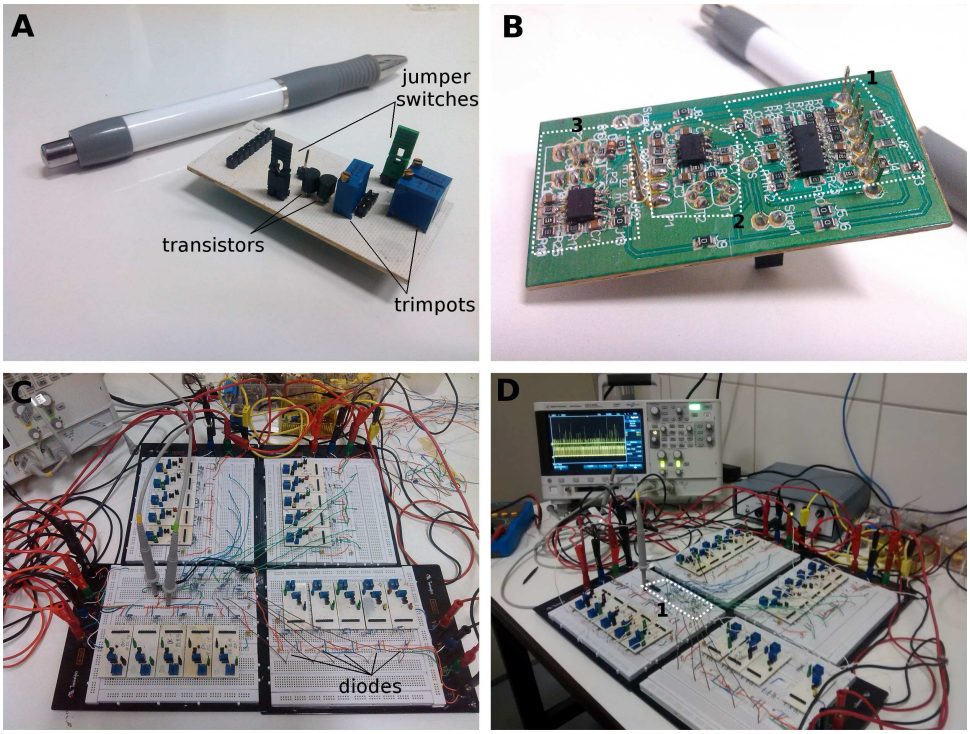


**Figure 5.2** Experimental setup for measurements of dynamic range of electronic neuron networks. (A) Printed circuit module board used as a building block in the construction of networks of electronic neurons (pen for size comparison). Jumper switches, transistors and trimpots are indicated. (B) Reverse side of the module board, showing the individual sub-modules: 1) excitable electronic circuit, 2) noise generator circuit and 3) electronic synapse. (C) Setup with all twenty module boards mounted on four protoboards. The diodes at the output of the excitable circuits in one of the protoboards are shown. (D) Running setup, showing the voltage source and the oscilloscope used in the measurements. 1) The analog summator circuit used for the measurement of the mean network activity $F$ is mounted on one of the protoboards.

$V_{rms}$), the outgoing synaptic strength $S$ and the synaptic decay time scale $\tau_{down}$ with the use of trimpots, i.e. variable resistors. In particular, the electronic synapse sub-module produces two different outputs for the same input voltage $V_{pre}$: one act as an EPSP and the other as an IPSP. The sub-modules within the board can easily be connected or disconnected from one another with the use of standard jumper switches, for example making possible to turn off the noisy input $V_{noise}$ at the excitable circuit while sending its output voltage $V_{pre}$ to the electronic synapse. The trimpots and the jumper switches are shown in Fig. 5.2A. Altogether we have produced twenty of these boards with the purpose of using them as building blocks in the construction of networks.

We connect up to five of theses boards on a single protoboard, which distributes to all modules the same supply voltages ($+12$ V and $-12$ V) for the operational amplifiers used in the various circuits, the same DC input $V_{DC}$ controlling the position of the fixed point of each excitable circuit as well a common ground potential. The setup showing four protoboards with all twenty of our module boards is shown in Fig. 5.2C, while the whole setup is shown in action

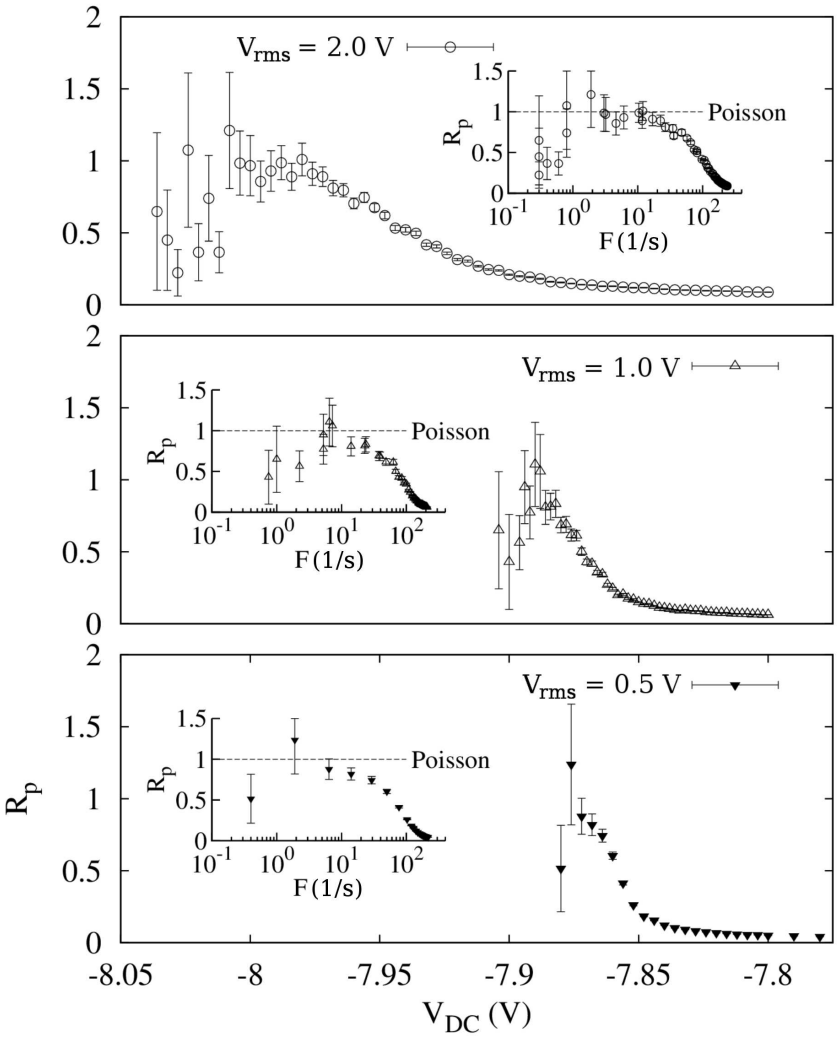


**Figure 5.3** Incoherence parameter $R_p$ as a function of the stimulus intensity $V_{DC}$ for three noise intensities $V_{noise}$, measured for a single excitable electronic circuit. For small $V_{DC}$ the interspike interval distribution is approximately poissonian. However, as the value of the Hopf bifurcation ($V_{DC} \simeq -7.82$ V) is approached, the spike trains become more regular (coherent), therefore deviating from the Poisson distribution. The insets show the incoherence parameter as a function of the mean firing rate $F$ of the electronic neuron.

in Fig. 5.2D along with its power supply and the oscilloscope used in the measurements.

With only two oscilloscope measurement probes, we are unable to track the state of each electronic neuron individually, therefore making it impossible to measure the density of active sites as in the cellular automaton model. Instead, to measure network activity, we add together the rectified outputs of all electronic excitable circuits. For that we employ an summator circuit mounted in one of the protoboards (region inside the dashed line in Fig. 5.2D). To rectify the outputs, i.e. to take into account only the positive part of incoming potentials, we include one standard diode, also mounted on the protoboards, at the output of each electronic circuit (as shown in Fig. 5.2C). This is done in the same fashion as what is done at the input of the

synaptic circuit, therefore the summator circuit only adds the positive part of the incoming spikes. The mean network firing rate $F$ is obtained simply by counting the number of spikes in a time series provided by the summator circuit and dividing it by the duration of the time series and the total number of electronic neurons $N$ in the network. Finally, due to the usually high number of spikes being added, the summator circuit attenuates the spikes by a factor of about 30, thus making each spike correspond to peak of order 250 mV (see Fig. 5.4B).

The modular structure of our circuit boards allows the creation of networks of different topologies. The connection between the modules is made in the following way: the electronic excitable circuit receives at its input the noise voltage $V_{noise}$ generated within the same module board, the DC input $V_{DC}$ distributed by the protoboard and the synaptic input $V_S$ from its neighbors, resulting in a voltage $V_{pre}$ that is sent to the synaptic circuit within the module board, which then is sent to the input of other excitable circuits with the use of small diameter copper wires. By changing the position of these wires, different topologies are obtained.

For all chosen networks, $F$ is measured as a function of the DC input $V_{DC}$ (equal for all modules), which operates as the network external stimuli. According to Fig. 1.25, fixing $V_{DC}$ while keeping a small noise amplitude $V_{rms}$ makes an isolated excitable circuit produce spike trains that have interspike interval distributions similar to the Poisson distribution. In Figure 5.3 we show that keeping $V_{rms}$ fixed while decreasing the external stimulus intensity $V_{DC}$ in isolated electronic neurons also induce Poissonian distributions as indicated by the unity value of the incoherence parameter $R_p$. In this regime, the noise input acts as a DC-Poisson converter, turning a constant stimulus into a Poisson rate. However, as $V_{DC}$ approaches the Hopf bifurcation value of the excitable circuit, this approximation does not hold: the spike trains become more and more coherent with increasing interspike interval regularity, therefore preventing the mapping of a Poisson rate $r$ into the external stimulus intensity $V_{DC}$. This is one of the main differences between our experimental setup and the cellular automaton model.

Another important feature of our setup is that a saturation value for the network activity $F$ is not observed as it is in the cellular automaton model. As explained before in Chapter 1, if $V_{DC}$ is increased beyond the Hopf bifurcation value, the electronic neuron enters the tonic regime, firing repeatedly even without the noisy input. Consequently, we arbitrarily chose the mean network value for the Hopf bifurcation voltage $\langle V_{Hopf} \rangle = -7.25$ V as the superior limit of the external stimulus. Despite the fact that each module is made with electronic components of equal values, the factory tolerance of the components allied with the great number of components used produce noticeable differences in the $V_{Hopf}$ across the modules (see Table 5.1 for details).

In order to verify the dependency of the dynamic range of the electronic networks with the mean network connectivity, we chose as control parameter the mean value of the synaptic strengths of each module. Instead of drawing values of $S$ from a uniform distribution, as done for the cellular automaton model, for simplicity sake all the synaptic strengths are set with equal values for any given measurement. Therefore our control parameter is simply $S$, the value of the synaptic strength of any of the synaptic circuits in the network. It is important to state that $S$ relates to the probability that a post-synaptic spike happens given the occurrence of a pre-synaptic spike, as shown in Fig. 2.10C. Therefore both $\sigma$ (in the model) and $S$ (in the circuit) control the network connectivity increasing or decreasing the post-synaptic spike probability.

| Module number | 1 | 2 | 3 | 4 | 5 |
|---|---|---|---|---|---|
| $V_{Hopf}$ (V) | -7.26 | -7.30 | -7.36 | -7.10 | -7.24 |
| Module number | 6 | 7 | 8 | 9 | 10 |
| $V_{Hopf}$ (V) | -7.13 | -7.19 | -7.22 | -7.11 | -7.27 |
| Module number | 11 | 12 | 13 | 14 | 15 |
| $V_{Hopf}$ (V) | -7.42 | -7.24 | -7.30 | -7.19 | -7.30 |
| Module number | 16 | 17 | 18 | 19 | 20 |
| $V_{Hopf}$ (V) | -7.34 | -7.46 | -7.27 | -7.33 | -7.24 |

**Table 5.1** Hopf bifurcation voltage values for all twenty module boards. The mean value $\langle V_{Hopf} \rangle \simeq -7.25$ V is used as the upper limit for measuring dynamic ranges. The variation is due to the electronic components factory tolerance of 5% and the large amount of components used.

Our choice of control parameter is similar to the one employed in the measurement of the dynamic range of hypercubic deterministic lattices of coupled Morris-Lecar model neurons or Greenberg-Hastings cellular automata [68].

The main parameter values used in the following dynamic range measurements, equal for all modules, were the excitable circuit capacitance, fixed at 1 nF, therefore setting the spiking time scale in the millisecond range, similar to biological neurons, the synaptic circuit capacitance, set at 10 nF and the noise amplitude produced by each noise generator, set at $V_{rms} = 3.0$ V. The other electronic components with fixed values can be found in Appendix B. The synaptic decay time $\tau_{down}$ was varied in some of the measurements. The time series captured by the oscilloscope at our disposal were limited, by the oscilloscope capabilities, to a maximum sampling of $10^5$ points. All the spike trains were recorded over a duration of 10 s with a sampling rate of $10^4$ points per second. This 10 s duration was chosen to maximize the length of the spike trains recorded while keeping the sampling able to capture individual spikes.

With this setup we have the freedom of choosing different topologies for the measurement of the dynamic ranges. Here we focus on linear lattices, a random network with neighborhood size (or network degree) $K = 2$ and a Cayley tree with three "branching generations".

## 5.2 Results

First of all, we measured the dynamic range $\Delta$ of a single excitable circuit to use it as a comparison with the results obtained from the networks. The module number 5 was chosen for that measure due to its Hopf bifurcation voltage value, which is very close to mean value $\langle V_{Hopf} \rangle = -7.25$ V (see Table 5.1). The dynamic range is determined as in Eq. (1.56):

$$\Delta \equiv 10 \log_{10} \left( \frac{V^*_{0.9}}{V^*_{0.1}} \right), \tag{5.3}$$

where $V^*_x \equiv V_x - V_0$ is measured relative to the voltage $V_0$ at which the response becomes different from the base-line activity $F_0$, which is either zero for subcritical networks or nonzero for supercritical ones. This time, to account for the possibility of a supercritical regime, a

modification in way the voltages $V_{0.9}$ and $V_{0.1}$ are calculated has to be made. Equation (1.57) has to be modified to assume a form similar to Eq. (5.2):

$$F(V_x) = F_0 + x(F_{max} - F_0) \qquad (0 \leq x \leq 1) \; . \tag{5.4}$$

In this case, for a single electronic neuron, $F_0 = 0$ and the result obtained was $\Delta = 8.92$ dB.

In our measurement, $V_o$ was determined using the same arbitrary approximation we used when measuring $\Delta$ for one electronic neuron in Chapter 1, i.e. $V_0$ corresponds to the voltage at which $F = 0.01F_{max}$. This, however, is only valid for subcritical networks, where the baseline activity is zero. If a network is in a supercritical regime, $V_0$ then corresponds to the voltage at which $F = 1.01F_0$, where $F_0$ is the network baseline activity.

### 5.2.1 Linear regular lattices

Dynamic range measurements in networks of cellular automaton models (as described in this Chapter) have shown that the increase in $\Delta$ for regular lattices of any dimension has a logarithmic dependence on the number $N$ of network elements, although for very large values of $N$ the dynamic range begins to saturate due to the refractory period of each cellular automaton [33, 35]. Following this lead, we start our measurements in linear regular lattices for a few values of $N$.

The first network used was a linear lattice with unidirectional connections and total number of modules $N = 5$. The synaptic decay time scale in each connection is $\tau_{down} = 0.2$ ms (fast synapses as in Chapter 3). The network diagram is shown if Fig. 5.4A. Two typical time series from the output of the summator circuit, measuring the network activity, are shown in Fig. 5.4B, one for uncoupled electronic neurons and the other for large synaptic strength, and both with moderate external stimulus intensity. The spike counting in time series like the ones shown in Fig. 5.4B and Fig. 5.5C is made by measuring the height of each maximum that reaches a small threshold and divide them by the mean height of a single spike. The threshold is slightly less than the height of a single spike, and big enough to avoid baseline fluctuations. The result is rounded down and added to the current number of spikes. To obtain the network activity $F$, we divide the total number of spikes by the time series duration (10 s) and $N$. Therefore $F$ measures the mean firing rate of the whole network. In Fig. 5.4C we show the response curves. This procedure was made for every networked measured. In Fig. 5.4D we show the dependency of the dynamic range with the mean network connectivity $S$, showing that for such small network with few connections there is no perceivable increase in dynamic range. Also there is no onset of self-sustained activity in the network.

Expecting a larger increase in the dynamic range, we increased the network connectivity by considering linear lattices with bidirectional connections, with sizes $N$ equal to 5, 10 and 20 elements. The network diagrams are shown in Fig. 5.5A and B, for $N = 5$ and $N = 10$ respectively (we omit the network diagram for $N = 20$ since it is structurally equal to the previous two). The network activity for the network with size $N = 20$ is shown in Fig. 5.5C for weak and strong coupling and the same external stimulus intensity. For larger sizes networks, the total number of spikes increases when compared to networks with smaller sizes. Furthermore, with stronger coupling, more electronic neurons tend to fire together as the result of a chain

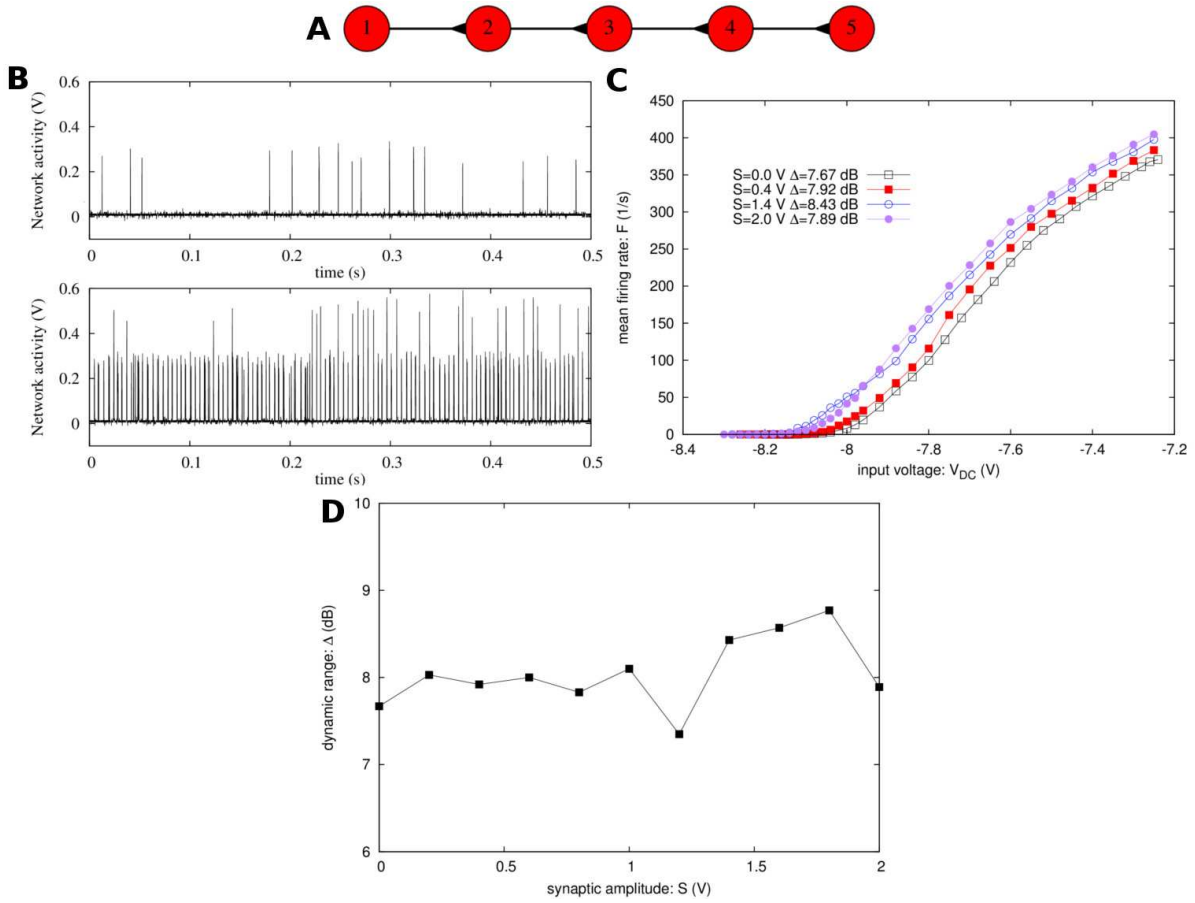


**Figure 5.4** Linear lattice network with $N = 5$ and unidirectional connections. (A) Diagram of the network. Each red circle corresponds to a module board. The triangle at the end of each line connecting two modules represents an unidirectional incoming excitatory synapse. (B) Time series measured at the output of the summator circuit. Every spike coming from the network produces a peak in voltage of about 250 mV due to the attenuation employed during the addition. Top graph: uncoupled network ($S = 0$ V). Bottom graph: network coupled with synaptic strength $S = 1.6$ V. Note that when two or more electronic neurons fire together, the result is a peak of value approximately equal to number of spikes that fired together times 250 mV. In both cases the external stimulus is $V_{DC} = -7.80$ V. (C) Response curves (mean firing rate $F$ as function of the external stimulus $V_{DC}$) for various network connectivity $S$. (D) Dynamic range $\Delta$ as a function of $S$.

of EPSP's propagating in the network, therefore larger peaks in the output of the summator circuit are observed. Figures 5.5D, E and F shows the response curves ($F$ as a function of $V_{DC}$) obtained for different synaptic strengths $S$ in networks with size $N = 5$, $N = 10$ and $N = 20$ respectively. Note that as $N$ increases the response curves for different couplings become more distinguished from one another. Also, the largest increase of $\Delta$ happens for $N = 20$ with the strongest synaptic coupling measured $S = 2.0$ V.

Figure 5.5G shows the dynamic range as function of our control parameter $S$. Although not very pronounced, $\Delta$ presents a tendency of increasing with the network connectivity, particu-

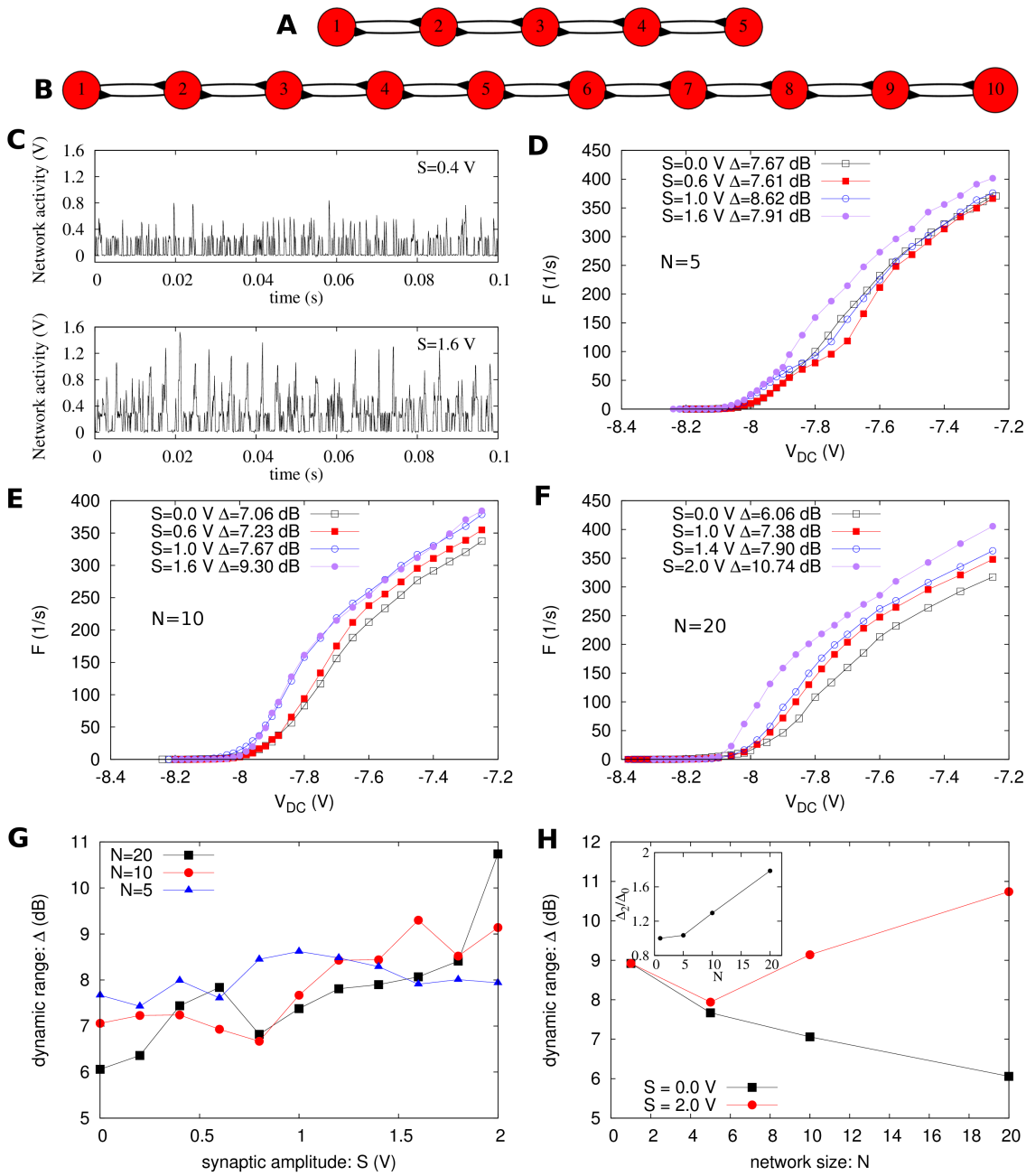


**Figure 5.5** Dynamic range for linear lattice networks with bidirectional connections. Diagram of the networks with size $N = 5$ (A) and $N = 10$ (B). The diagram for $N = 20$ was omitted due to its similarity to the previous two. Synaptic decay time is $\tau_{down} = 0.2$ ms. (C) Time series for the $N = 20$ network with weak ($S = 0.4$ V) and strong synaptic strength ($S = 1.6$ V) both with $V_{DC} = -7.80$ V. Note that with more elements and stronger coupling, more electronic neurons tend to fire together (see Fig. 5.4B for comparison). Response curves for the networks with $N = 5$ (D), $N = 10$ (E) and $N = 20$ (F) elements for various synaptic strengths. (G) Dynamic range $\Delta$ as a function of the network synaptic strength $S$ for all three network sizes. (H) $\Delta$ as a function of the network size $N$ for uncoupled ($S = 0$ V) and strongly coupled ($S = 2$ V) networks. Inset: Relative dynamic range gain as a function of $N$. $\Delta_0$ and $\Delta_2$ are the dynamic ranges calculated with $S = 0$ V and $S = 2$ V.

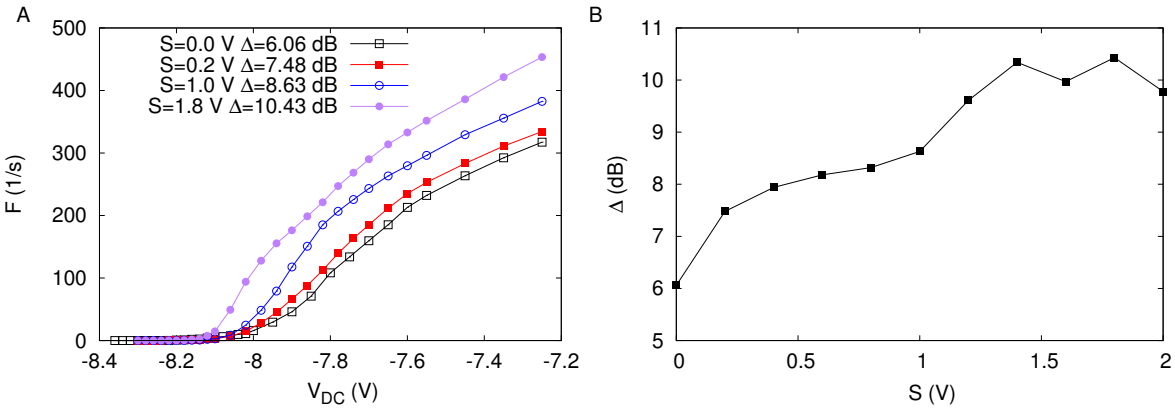


**Figure 5.6** Response curves and dynamic range for a linear lattice network with bidirectional connections, $N = 20$ elements and slow synapses. The synaptic characteristic decay time is $\tau_{down} = 1.0$ ms. (A) $F$ as a function of $V_{DC}$ for a few values of the synaptic strength $S$. (B) Dynamic range $\Delta$ as a function of the of the synaptic strength $S$. Compared to the black curve in Fig. 5.5G, the dynamic range increase is more pronounced for almost all values of $S$.

larly for larger $N$. We attribute the lack of "smoothness" of the measured curves to the overall low number of elements present in the networks specially when compared to the number of elements used in the cellular automaton model ($10^5$). The dependency of the dynamic range with the network size is shown in Fig. 5.5H for uncoupled networks ($S = 0$ V) and networks with the strongest coupling ($S = 2$ V). As expected, for coupled networks $\Delta$ increases when $N$ increased, but the dynamic range actually decreases when $N$ increases in the uncoupled case. This can be explained based on the definition used for the calculation of dynamic ranges (Eq. (5.3)). Adding more elements to an uncoupled network increases its sensibility, making it more likely to spike in response to low intensity stimuli during the measurement time of 10 s. This reduces the value of $V_0$, the point at which the mean network firing rate is 1% of the maximum value $F_{max}$, which increases the separation between $V_0$ and $V_{0.1}$, therefore increasing the denominator in Eq. (5.3). Since the mean network firing rate $F$ is normalized by $N$, the increase in the difference between $V_{0.9}$ and $V_0$ in the numerator of Eq. (5.3) is not as large, particularly because 10 s is more than enough to measure large firing rates. This has an overall result of reducing $\Delta$ as we increase $N$. This measurement artifact can be removed by measuring the spike trains for a longer duration in smaller networks, causing a reduction of their dynamic range in low external stimuli regime, but this could not be done due to the limitations of our oscilloscope. The inset of Fig. 5.5H shows the effective dynamic range increase as a function of $N$. We define $\Delta_2/\Delta_0$ as the ratio of the dynamic ranges measured when the network has synaptic strength $S = 2$ V and $S = 0$ V. The increase is greater for larger values of $N$ as expected, although we could not verify the logarithmic dependence with such few points.

So far all measurements in this Chapter were made with synapses whose characteristic decay time was $\tau_{down} = 0.2$ ms, i.e. fast synapses that produce EPSPs with duration similar to the duration of a spike. Here we proceed to investigate if increasing the characteristic decay time further increases the dynamic range. This is expected since EPSPs with longer duration

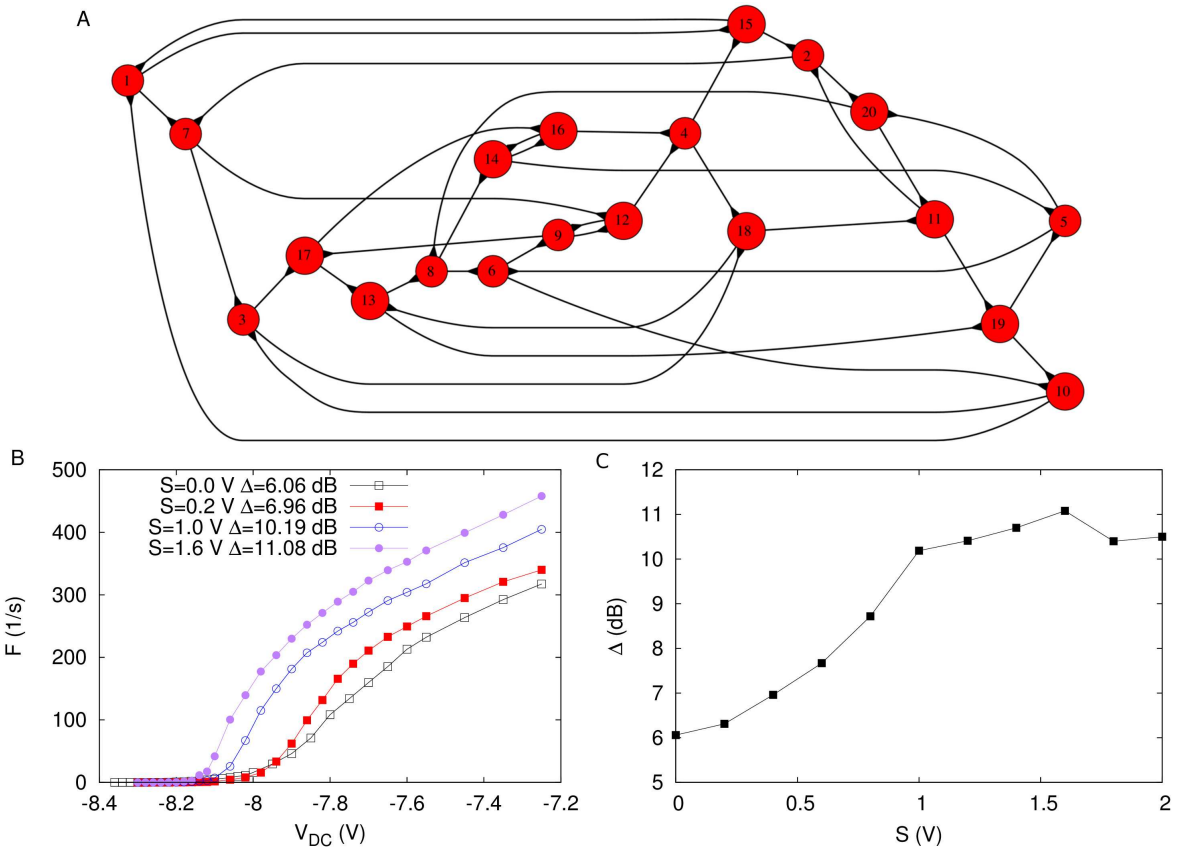


**Figure 5.7** Dynamic range in a random network of degree 2 with $N = 20$ and synaptic decay time $\tau_{down} = 1$ ms. (A) Network diagram. (B) Response curves ($F$ vs $V_{DC}$) for a few values of synaptic strength $S$. (C) Dynamic range as a function of the synaptic strength.

are more likely to induce a spike in the neighborhood of the pre-synaptic electronic neuron than a short one. Therefore, increasing $\tau_{down}$ should effectively increase the network coupling strength.

Figure 5.6A shows the response curves of a linear lattice network with bidirectional connections and synaptic decay time $\tau_{down} = 1$ ms (slow synapse as in Chapter 3). Although these results look similar to response curves of the same network but with fast synapses (Fig. 5.5F), the dynamic range, shown in Fig. 5.6B as a function of the synaptic strength $S$, for most values of $S$ presents a larger increase than in the case where fast synapses are used. Considering this result, from now on only slow synapses will be employed in the measurements. Despite that, again, no self-sustained activity was observed regardless of the network size or synaptic characteristic decay time.

### 5.2.2 Random network with degree 2

Moving away from linear lattices, we now investigate how the dynamic range depends on the synaptic strength on a random network of electronic excitable elements. In our network,

each element makes connections with two randomly chosen elements, avoiding the case where two connections are made with same element and also avoiding self-connections. Another restriction is that no element can receive more than two connections. This assures that each element have two incoming synapses and two outgoing ones. Using the common jargon of complex networks, we say that each element has both in-degree and out-degree equal to two. The diagram for a network with $N = 20$ constructed in such way is shown in Fig. 5.7A. Since our electronic synapses are chemical inspired, the connections are directed, differently from the cellular automaton model discussed previously, where the Erdős-Rényi random network had undirected connections. Therefore a connection from module $i$ to module $j$ does not imply a connection from module $j$ to module $i$.

Figure 5.7B shows the response curves for the random network in Fig. 5.7A. Despite having the same number of excitable circuits as the last linear lattice ($N = 20$), this network structure allows the spikes to better propagate through the network, therefore the maximum mean network firing rate $F_{max}$ for each response curve is greater this time than in the previous case, but even with the increased mean firing rates, there is no self-sustained regime in this case either. Figure 5.7C shows the dynamic range as a function of the network synaptic strength $S$. The maximum value of dynamic range attained in this network is the greatest so far, $\Delta = 11.08$ dB with a 1.83 increase factor compared to the uncoupled case, suggesting the increase in $\Delta$ is more pronounced for random networks than for linear lattices.

### 5.2.3 Cayley tree network

The last network measured was a Cayley tree with size $N = 15$. Recently Cayley trees (also known as Bethe lattices) were used to model the excitability of active neuronal dendritic trees. Cellular automata were used again to model the excitability dynamics of the tree branches and results show that large dynamic ranges arise in such networks as a consequence of large amount of afferent connections, i.e. convergent connections that "point" to the neuron soma [69]. Similar results were obtained for morphologically and biophysically detailed models of retina ganglion cells, showing that large and active dendritic trees enhance the dynamic range of the cell [70]. It was also shown that an increasing number of tree bifurcations as well as introducing inhomogeneity in the connections between branchlets in cellular automaton models leads to critical behavior with maximization of the dynamic range [71].

The network used is shown in Fig. 5.8A. The number of layers $G$ is set to 3 and the network "grows" from the initial layer $g = 0$, bifurcating at every new layer. The connections between the layers are bidirectional, therefore allowing spikes to propagate to inner layers as well as to outer layers. Back propagating spikes, i.e. spikes that propagate to the outer layers of the tree, are supposed to play an important role in the determination of the dynamic range, since they are able to block spikes coming in the forward direction due to the refractoriness wave they leave behind [69].

Dynamic range measurements in cellular automaton models are made from the response curve of the brachlet with a single element (labeled "1" in Fig. 5.8A) at the initial layer $g = 0$. Here, we chose to repeat the procedure used in the previous networks and measure the activity of the whole network. The mean firing rate $F$ as a function of the external stimulus $V_{DC}$ is shown in Fig. 5.8B. Despite the overall smaller dynamic range presented by this network, the effective

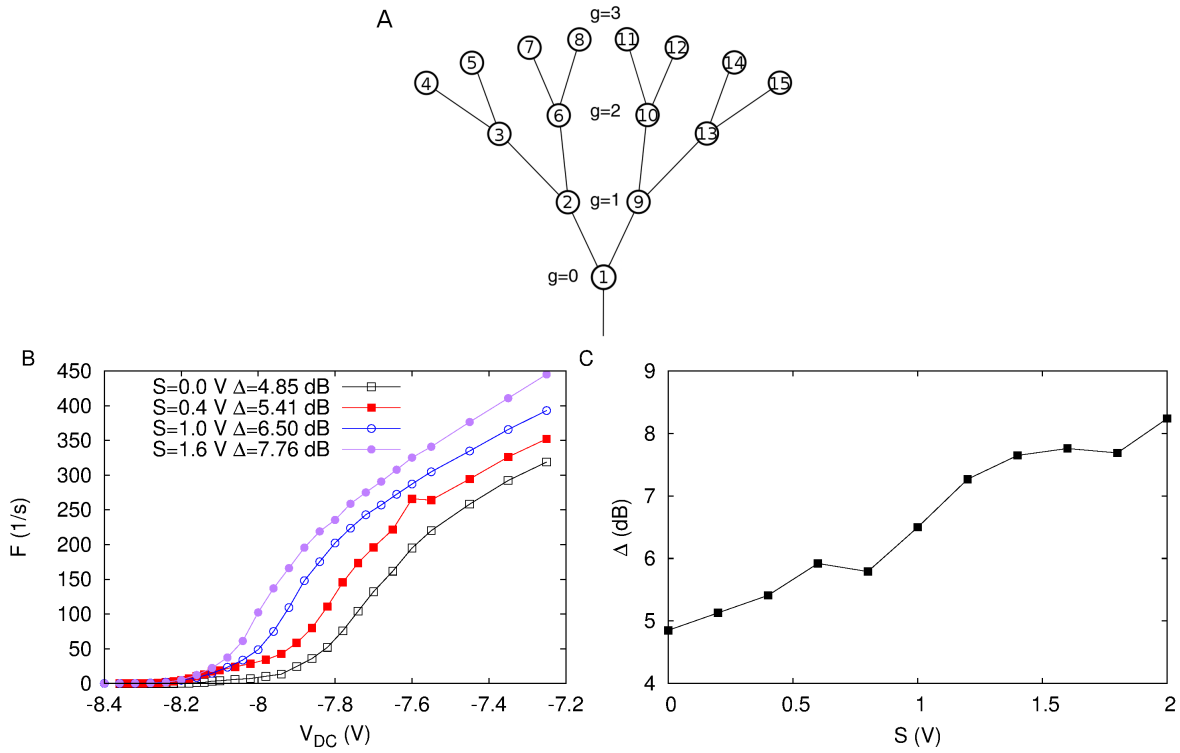


**Figure 5.8** Dynamic range in a Cayley tree network with $N = 15$ and synaptic decay time $\tau_{down} = 1$ ms. (A) Network diagram. The connections are all bidirectional. (Adapted from Gollo *et al.* (2013) [71]). (B) Response curves ($F$ vs $V_{DC}$) for a few values of synaptic strength $S$. (C) Dynamic range as a function of the synaptic strength.

increase in $\Delta$ ($\Delta_2/\Delta_0 = 1.70$) is of the same order of networks with size $N = 20$ while having only 15 elements. Furthermore, $\Delta$ as a function of the synaptic strength $S$ (Fig. 5.8C) shows a very similar behavior, an approximately linear growth, to Cayley trees of cellular automata with 4 layers ($g = 4$) when the probability that controls the network connectivity is increased [71]. Again, no self-sustained regime was found for this network.

The lack of a critical regime in our electronic networks, and consequently the absence of self-sustained network activity, is mainly due to the small number of network elements. Small networks with few connections have, in general small connectivity. The solution to this problem might lie in increasing even more the synaptic decay time, so that, in average, one spike becomes able to produce more than one spike in its neighborhood, or by just adding more network connections. Nevertheless, we were able to demonstrate the dynamic range increase in a biologically-inspired physical system.

CHAPTER 6

# Conclusion

In this work we have proposed two electronic circuit models, one with similar dynamics to the FitzHugh-Nagumo model for neuronal excitability [23] and another that reproduces the first-order kinetics that is characteristic of fast synapses such as AMPA and $GABA_A$ [58]. These circuits were designed to be as simple as possible, therefore allowing easy mathematical description and scalability, while admitting freedom in the choice of relevant parameters for the system dynamics, e.g. time scales either from the excitable circuit or the synapse and synaptic conductances. This approach allows for the investigation of collective phenomena where excitable elements are the main agents. Complementary circuits like noise generators and circuits that implement analog addition and subtraction, for example, were also used to help achieve this goal. In light of the many possible lines of investigation regarding excitable elements, we focused our efforts on the study of synaptic symmetry effects that lead to coherence or incoherence resonance and on the phenomena of dynamic range increase.

We have studied the effects of excitatory synaptic coupling between excitable electronic neurons on the coherence of their spike trains [58]. We have shown that the coherence resonance observed in uncoupled neurons deteriorates in the post-synaptic neuron when the synaptic connection is unidirectional. Furthermore, coherence resonance is restored and strengthened when the synaptic loop is closed in a bidirectional coupling.

It is important to emphasize that, although this phenomenon may look similar to the synchronization between excitatory bidirectionally coupled spiking neurons [48, 44], here neurons are excitable and the only attractor of the system is a fixed point with both neurons quiescent. In this sense, it is interesting that the interplay between noise and synaptic coupling leads a post-synaptic neuron to regain its coherence by means of an outgoing synapse.

Furthermore, the mechanism by which this increase in coherence is attained depends on the synaptic time scale. With faster synapses, moving from a unidirectional coupling to bidirectional coupling by strengthening one of the synapses leads to an increase in coherence while firing rates decrease (despite the fact that all synapses are excitatory). For slower synapses, the same coherence increase is achieved with an increase in firing rates.

Overall, our results show that, for fast synapses, the average coherence of the spike trains can be maintained in a broad region of synaptic-strength parameter space. However, as synapses become slower, maximal coherence is achieved only in a much more restricted region, around the symmetry axis $S_{12} = S_{21}$. Along this axis, strengthening synaptic connections lead to an increase in coherence beyond the values attained by isolated neurons.

All the results above for electronic neurons were qualitatively reproduced with computer simulations of synaptically coupled excitatory FitzHugh-Nagumo models, suggesting the phenomenon is robust. It would be worth exploring whether it remains valid when neurons have

a different excitability class, such as those near a saddle-node bifurcation [72]. Such type-I-excitable neurons can often be further reduced to simpler descriptions [73] which then might allow an analytical understanding of the results presented here.

Naturally, the ultimate test of our results would come from electrophysiological recordings of real neurons in which the symmetry of the synaptic coupling could be controlled. Although we are unaware of experiments in that direction, our results could also be useful to (or validated in) other systems not directly related to neuroscience, but where CR has been experimentally observed. The experimental setups range from semiconductor lasers [74] to the famous Belousov-Zabotinsky chemical reaction [75], recently also reaching nanoscopic scales in the ionic transport through single-walled carbon nanotubes [76]. If, for instance, applications on these setups depend on highly coherent states, then symmetry in the coupling may prove useful to overcome coherence degradation due to external factors.

Taken together, our results point to the importance of allowing for inhomogeneity in CR studies of coupled excitable elements. Our study of a coupled pair, where inhomogeneity is reduced to the asymmetry of the synaptic connections, can be regarded as a first step towards larger networks.

Still on the subject of synaptic symmetry, we have studied the effect of inhibitory chemical coupling in the spike trains of a pair of excitable FitzHugh-Nagumo model neurons driven by independent noise sources of equal intensities. We have shown that inhibitory synapses with a fast synaptic time scale causes coherence deterioration in the post-synaptic neuron when the coupling is unidirectional in a similar way to what we have shown for excitatory synapses. The post-synaptic neuron, however, has its coherence partially restored (it does not reach the coherence level exhibited by an uncoupled neuron) when it is coupled with another inhibitory synapse to the pre-synaptic neuron in the reverse direction. This is slightly different than a closed loop with excitatory synapses for in that case both become more coherent than they would be if they were uncoupled. The mutually inhibitory coupled neurons tend to fire one after the other, in a way similar to the anti-phase synchronization presented by coupled tonic inhibitory neurons in the absence of noise [44].

We also studied the same system when the inhibitory coupling had a slow synaptic time scale. Coupling two model neurons unidirectionally, as in the previous case, also causes the post-synaptic neuron to have its coherence deteriorated, although in this case the effect is much more pronounced. Closing the loop with another slow inhibitory synapse, however, makes both model neurons transition to a very incoherent state, where, in general, only one of the neurons fire while the other is suppressed by the long lasting IPSPs arriving from the first neuron which, in turn, can become suppressed itself if a large enough noisy input causes the inhibited neuron to fire.

Addressing the role of synaptic symmetry in the coherence of the spike trains, we have shown that symmetric inhibitory synapses, cause the system to reach a state of maximum coherence, for fast synapses, or maximum incoherence, for slow synapses. Increasing the strength of the synapses while keeping symmetry causes the spike trains to become more incoherent, which shows that while inhibitory synapses can contribute to increase system coherence (in the case of fast synapses), their general effect is to lead the system to more incoherent states.

We have shown that, for fast inhibitory synapses, the firing rates of both neurons have a

weak positive correlation when the synapses are symmetric, meaning that as the firing rate of one of the neurons increase, the other tends to follow, corresponding to the case of anti-phase synchronization-like behaviour mentioned before. The contrary happens if the synapses are asymmetric (weak negative correlations). For slow synapses, however, the firing rates tend to be strongly negatively correlated in a large region around the symmetry axis, meaning that as one of the firing rates increases, the other decreases approaching near-zero values.

Finally, we have shown that the model neurons undergo a continuous transition from coherence resonance to incoherence resonance which is controlled by the time scale of the synapses. From fast to slow synapses, the incoherence of the spike trains have either a minimum (fast synapses) or maximum (slow synapses) at roughly the same noise input value.

Our work shows the importance of inhibitory synapses to the coherence of the system. In larger networks, highly symmetric inhibitory connection between neurons can induce either coherent or incoherent states depending on the synaptic time scale. Transition between such states could also be achieved by changing the time scale of such connections.

Moving to the problem of dynamic range enhancement in networks with excitatory connections, we have shown that networks whose basic composing elements were the excitable electronic circuit and synaptic circuit described in this work, reach increased values of dynamic range $\Delta$ for larger values of network coupling strength. Differently from purely computational models where the coupling strength is determined by setting post-synaptic spike probabilities, therefore making use of the average branching ratio $\sigma$ as the control parameter, we use the synaptic amplitude, equal for all connections in the network, as our control parameter for evaluating the dynamic range increase. In linear lattice networks, the increase is more noticeable in networks that have bidirectional connections between the elements. Increasing the network size, i.e. the number of elements present in the network, or the duration of the EPSP's, mainly controlled by the synaptic decay time, also directly increases the dynamic range. In random network with connectivity degree two, the increase in dynamic range is also present when the synaptic amplitudes are increased, and in general, due to better spike propagation through the network, the increase is more pronounced when compared to linear lattices. Finally, we have shown that for a Cayley tree of 15 elements the dynamic range increase is comparable to the increase observed in random networks of size 20 and also that the dependence of $\Delta$ with the synaptic amplitude is similar to that of models of cellular automaton networks for dendritic excitability with a smaller number of elements.

The onset of self-sustained activity in cellular automaton network models as a result of increasing network coupling strength happens at a phase transition, where the system is critical and dynamic range is maximized [29]. Although this supercritical regime of self-sustained activity has not been found in any of the networks of electronic elements we studied, which is mostly due to small number of network elements, preliminary results suggest that increasing the synaptic time constants beyond the values used throughout this work can throw a pair of mutually connected excitable circuits in an self-sustained attractor, despite the fact that both electronic neurons are individually in a excitable state. Similar effects have been observed in a pair of electrically-coupled $\theta$-neurons [73] and are likely to be important in an implementation of a neuro-inspired artificial sensor with maximal dynamic range and sensitivity. Nevertheless, our experiments provide a prototype, proof-of-concept version of such sensor.

# References


[1] P. Dayan and L. F. Abbott. *Theoretical Neuroscience: Computational and Mathematical Modeling of Neural Systems*. The MIT Press, 2001.

[2] E. R. Kandel, J. H. Schwartz, and T. M. Jessel. *Principles of Neural Science*. The McGraw-Hill Companies, 2000.

[3] B. Linder, J. García-Ojalvo, A. Neiman, and L. Schimansky-Geier. Effects of noise in excitable systems. *Physics Reports*, 392:321–424, 2004.

[4] S. H. Strogatz. *Nonlinear Dynamics and Chaos: with Applications to Physics, Biology, Chemistry and Engineering*. Addison-Wesley, Reading, MA, 1997.

[5] A. L. Hodgkin and A. F. Huxley. Currents carried by sodium and potassium ions through the membrane of the giant axon of Loligo. *J. Physiol.*, 116:449–472, 1952.

[6] A. L. Hodgkin and A. F. Huxley. The components of membrane condutance in the giant axon of Loligo. *J. Physiol.*, 116:473–496, 1952.

[7] A. L. Hodgkin and A. F. Huxley. The dual effect of membrane potential on sodium conductance in the giant axon of Loligo. *J. Physiol.*, 116:497–506, 1952.

[8] A. L. Hodgkin and A. F. Huxley. A quantitave description of membrane current ands its application to conduction an excitation in nerve. *J. Physiol.*, 117:500–544, 1952.

[9] R. FitzHugh. Mathematical models for excitation an propagation in nerve. *Biological Engineering*, 1969.

[10] J. S. Nagumo, S. Arimoto, and S. Yoshizawa. An active pulse transmission line simulating nerve axon. *Proc. IRE*, 5:2061–2070, 1962.

[11] C. Koch. *Biophysics of Computation*. Oxford University Press, New York, 1999.

[12] E. M. Izhikevich. *Dynamical Systems in Neuroscience: The Geometry of Excitability and Bursting*. The MIT Press, London, 2007.

[13] J. Rinzel and B. Ermentrout. Analysis of neural excitability and oscillations. In C. Koch and I. Segev, editors, *Methods in Neuronal Modeling: From Ions to Networks*, pages 251–292. MIT Press, 2nd edition, 1998.

[14] J. L. Lancaster and E. H. Hellen. Modeling excitable systems: Reentrant tachycardia. *Am. J. Phys.*, 78:56–63, 2010.

[15] J. J. Ebers and J. L. Moll. Large-signal behavior of junction transistors. *Proc. IRE*, 42(12):1761–1772, 1954.

[16] M. Mahowald and R. Douglas. A silicon neuron. *Nature*, 354:515–518, 1991.

[17] A. Szucs, P. Varona, A. R. Volkovskii, H. D. I. Abarbanel, M. I. Rabinovich, and A. I. Selverston. Interacting biological and electronic neurons generate realistic oscillatory rhythms. *Neuroreport*, 11(3):563–569, 2000.

[18] J. Aliaga, N. Busca, V. Minces, G. B. Mindlin, B. Pando, A. Salles, and L. Sczcupak. Electronic neuron within a ganglion of a leech (Hirudo medicinalis). *Phys. Rev. E*, 67:061915, 2003.

[19] J. D. Sitt and J. Aliaga. Versatile biologically inspired electronic neuron. *Phys. Rev. E*, 76(5):051919, 2007.

[20] M. Copelli, A. C. Roque, R. F. Oliveira, and O. Kinouchi. Physics of Psychophysics: Stevens and Weber-Fechner laws are transfer functions of excitable media. *Phys. Rev. E*, 65:060901, 2002.

[21] Z. Mainen and T. Sejnowski. Reliability of spike timing in neocortical neurons. *Science*, 268:1503–1506, 1995.

[22] D. Petracchi, M. Barbi, S. Chillemi, E. Pantazelou, D. Pierson, C. Dames, L. Wilkens, and F. Moss. A test for a biological signal encoded by noise. *Int. J. Bifurcat. Chaos*, 5(1):89–100, 1995.

[23] B. N. S. Medeiros, V. Minces, G. B. Mindlin, M. Copelli, and J. R. Rios Leite. An excitable electronic circuit as a sensory neuron model. *Int. J. Bifurcat. Chaos*, 22(10), 2012.

[24] S. D. Senturia and B. D. Wedlock. *Electronic Circuits and Applications*. John Wiley, 1981.

[25] J.-P. Rospars, P. Lánský, P. Duchamp-Viret, and A. Duchamp. Spiking frequency versus odorant concentration in olfactory receptor neurons. *BioSystems*, 58:133–141, 2000.

[26] P. E. Kloeden, E. Platen, and H. Schurz. *Numerical solution of SDE through computer experiments*. Universitext. Springer-Verlag, Berlin, 1994.

[27] A. S. Pikovsky and J. Kurths. Coherence resonance in a noise-driven excitable system. *Phys. Rev. Lett.*, 78(5):775–778, 1997.

[28] S. S. Stevens. *Psychophysics: Introduction to its Perceptual, Neural and Social Prospects*. Wiley, New York, 1975.

[29] O. Kinouchi and M. Copelli. Optimal dynamical range of excitable networks at criticality. *Nat. Phys.*, 2:348–351, 2006.

[30] J. E. G. de Souza, B. B. Neto, F. L. dos Santos, C. P. de Melo, M. S. Santos, and T. B. Ludermir. Polypyrrole based aroma sensor. *Synth. Met.*, 102(1-3):1296–1299, 1999.

[31] E. D. Adrian. The impulses produced by sensory nerve endings: Part I. *J. Physiol. (London)*, 61:49–72, 1926.

[32] M. A. Arbib. *The handbook of brain theory and neural networks*. The MIT Press, 2002.

[33] M. Copelli and O. Kinouchi. Intensity coding in two-dimensional excitable neural networks. *Physica A*, 349(3-4):431–442, 2005.

[34] M. R. Deans, B. Volgyi, D. A. Goodenough, S. A. Bloomfield, and D. L. Paul. Connexin36 is essential for transmission of rod-mediated visual signals in the mammalian retina. *Neuron*, 36:703–712, 2002.

[35] L. S. Furtado and M. Copelli. Response of electrically coupled spiking neurons: a cellular automaton approach. *Phys. Rev. E*, 73:011907, 2006.

[36] V. R. V. Assis and M. Copelli. Dynamic range of hypercubic stochastic excitable media. *Phys. Rev. E*, 77:011923, 2008.

[37] C. Koch and I. Segev, editors. *Methods in Neuronal Modeling: From Ions to Networks*. MIT Press, 2nd edition, 1998.

[38] C. Neveu. Image file: Temporal summation. Original JPG file avaible at `http://commons.wikimedia.org/wiki/File:Temporal_summation.JPG`.

[39] A. Destexhe, Z. F. Mainen, and T. J. Sejnowski. Synthesis of models for excitable membranes, synaptic transmission and neuromodulation using a common kinetic formalism. *J. Comput. Neurosci.*, 1(3):195–230, 1994.

[40] A. Destexhe, Z. F. Mainen, and T. J. Sejnowski. Analysis of neural excitability and oscillations. In C. Koch and I. Segev, editors, *Methods in Neuronal Modeling: From Synapses to Networks*, pages 251–292. MIT Press, 2nd edition, 1998.

[41] S. A. Campbell. Cellular mathematical biology part ii - neurons. Lecture notes available at `http://http://www.math.uwaterloo.ca/~sacampbe/mathbio/`.

[42] M. Ciszak, O. Calvo, C. Masoller, C. R. Mirasso, and R. Toral. Anticipating the response of excitable systems driven by random forcing. *Phys. Rev. Lett.*, 90:204102, 2003.

[43] R. D. Pinto, R. C. Elson, A. Szücs, M. I. Rabinovich, A. I. Selverston, and H. D. I. Abarbanel. Extended dynamic clamp: controlling up to four neurons using a single desktop computer and interface. *J. Neurosci. Meth.*, 108(1):39 – 48, 2001.

[44] H. R. Wilson. *Spikes, decisions, and actions: The dynamical foundations of neuroscience*. Oxford University Press, 1999.

[45] F. S. Matias, P. V. Carelli, C. R. Mirasso, and M. Copelli. Anticipated synchronization in a biologically plausible model of neuronal motifs. *Phys. Rev. E*, 84:021922, 2011.

[46] L. F. Abbott and S. B. Nelson. Synaptic plasticity: taming the beast. *Nat. Neurosci.*, 3:1178–1183, 2000.

[47] Y. Kuramoto, editor. *Chemical Oscillations, Waves and Turbulence*. Dover, Berlin, 1984.

[48] A. Pikovsky, M. Rosenblum, and J. Kurths. *Synchronization: A Universal Concept in Nonlinear Sciences*. Cambridge University Press, Cambridge, UK, 2001.

[49] M. Newman. The structure and function of complex networks. *SIAM Rev.*, 45(2):167–256, 2003.

[50] E. Oh, D.-S. Lee, B. Kahng, and D. Kim. Synchronization transition of heterogeneously coupled oscillators on scale-free networks. *Phys. Rev. E*, 75:011104, 2007.

[51] A. Nordenfelt, J. Used, and M. A. F. Sanjuán. Bursting frequency versus phase synchronization in time-delayed neuron networks. *Phys. Rev. E*, 87:052903, 2013.

[52] T. Pereira, D. Eroglu, G. B. Bagci, U. Tirnakli, and H. J. Jensen. Connectivity-Driven Coherence in Complex Networks. *Phys. Rev. Lett.*, 110(23):234103, 2013.

[53] A. Arenas, A. Díaz-Guilera, J. Kurths, Y. Moreno, and C. Zhou. Synchronization in complex networks. *Physics Reports*, 469(3):93 – 153, 2008.

[54] J. F. Donges, H. C. H. Schultz, N. Marwan, Y. Zou, and J. Kurths. Investigating the topology of interacting networks. *Eur. Phys. J. B*, 84(4):635–651, 2011.

[55] Y. Q. Wang, D. T. Chik, and Z. D. Wang. Coherence resonance and noise-induced synchronization in globally coupled Hodgkin-Huxley neurons. *Phys. Rev. E*, 61(1):740–746, 2000.

[56] R. Toral, C. R. Mirasso, and J. D. Gunton. System size coherence resonance in coupled FitzHugh-Nagumo models. *Europhys. Lett.)*, 61(2):162, 2003.

[57] P. Balenzuela and J. García-Ojalvo. Role of chemical synapses in coupled neurons with noise. *Phys. Rev. E*, 72(2, Part 1), 2005.

[58] B. N. S. Medeiros and M. Copelli. Synaptic symmetry increases coherence in a pair of excitable electronic neurons. *PloS One*, 8(12):e82051, 2013.

[59] C. Zhou, J. Kurths, and B. Hu. Array-enhanced coherence resonance: Nontrivial effects of heterogeneity and spatial independence of noise. *Phys. Rev. Lett.*, 87:098101, 2001.

[60] O. Kwon and H.-T. Moon. Coherence resonance in small-world networks of excitable cells. *Phys. Lett. A*, 298(5–6):319 – 324, 2002.

[61] B. Lindner, L. Schimansky-Geier, and A. Longtin. Maximizing spike train coherence or incoherence in the leaky integrate-and-fire model. *Phys. Rev. E*, 66:031916, 2002.

[62] Richard A Satterlie. Reciprocal inhibition and postinhibitory rebound produce reverberation in a locomotor pattern generator. *Science*, 229(4711):402–404, 1985.

[63] A. M. Lacasta, F. Sagués, and J. M. Sancho. Coherence and anticoherence resonance tuned by noise. *Phys. Rev. E*, 66:045105, 2002.

[64] B. Lindner, L. Schimansky-Geier, and A. Longtin. Maximizing spike train coherence or incoherence in the leaky integrate-and-fire model. *Phys. Rev. E*, 66:031916, 2002.

[65] R. Publio, R. F. Oliveira, and A. C. Roque. A computational study on the role of gap junctions and rod $I_h$ conductance in the enhancement of the dynamic range of the retina. *PLoS One*, 4(9):e6970, 2009.

[66] D. B. Larremore, W. L. Shew, and J. G. Restrepo. Predicting criticality and dynamic range in complex networks: effects of topology. *Phys. Rev. Lett.*, 106(5):058101, 2011.

[67] W. L. Shew, H. Yang, T. Petermann, R. Roy, and D. Plenz. Neuronal avalanches imply maximum dynamic range in cortical networks at criticality. *J. Neurosci.*, 29(49):15595–15600, 2009.

[68] T. L. Ribeiro and M. Copelli. Deterministic excitable media under Poisson drive: Power law responses, spiral waves and dynamic range. *Phys. Rev. E*, 77:051911, 2008.

[69] L. L. Gollo, O. Kinouchi, and M. Copelli. Active dendrites enhance neuronal dynamic range. *PLoS Comput. Biol.*, 5(6):e1000402, 2009.

[70] R. Publio, C. C. Ceballos, and A. C. Roque. Dynamic range of vertebrate retina ganglion cells: Importance of active dendrites and coupling by electrical synapses. *PLoS ONE*, 7(10):e48517, 2012.

[71] L. L. Gollo, O. Kinouchi, and M. Copelli. Single-neuron criticality optimizes analog dendritic computation. *Scientific Reports*, 3, 2013.

[72] J. Bing, G. Hua-Guang, and L. Yu-Ye. Coherence-resonance-induced neuronal firing near a saddle-node and homoclinic bifurcation corresponding to type-i excitability. *Chinese Phys. Lett.*, 28(9):090507, 2011.

[73] B. S. Gutkin, J. Jost, and H. C. Tuckwell. Transient termination of spiking by noise in coupled neurons. *Europhys. Lett.*, 81(2):20005, 2008.

[74] G. Giacomelli, M. Giudici, S. Balle, and J. R. Tredicce. Experimental evidence of coherence resonance in an optical system. *Phys. Rev. Lett.*, 84:3298–3301, 2000.

[75] K. Miyakawa and H. Isikawa. Experimental observation of coherence resonance in an excitable chemical reaction system. *Phys. Rev. E*, 66:046204, 2002.

[76] C. Y. Lee, W. Choi, J.-H. Han, and M. S. Strano. Coherence resonance in a single-walled carbon nanotube ion channel. *Science*, 329(5997):1320–1324, 2010.

APPENDIX A

# Simple electronic circuits

Throughout this work, we mentioned circuits that employ operational amplifiers as their main component. Unlike passive electronic components, such as resistors and capacitors, operational amplifiers are active components, which require a supply voltage for proper function. A more detailed review of the circuits presented in this Appendix can be found in the textbook by S. D. Senturia and B. D. Wedlock [24].

## A.1 Comparator circuit

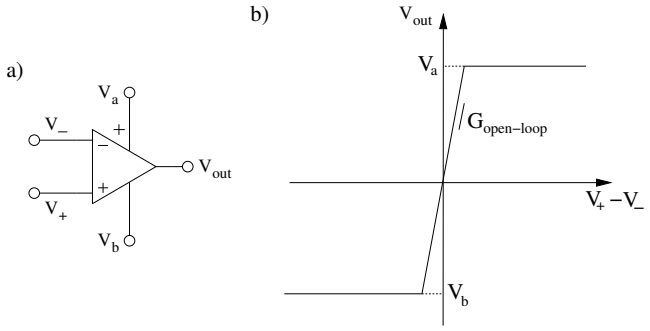


**Figure A.1** a) Comparator circuit (operational amplifier). b) Output voltage $V_{out}$ as a function of $V_+ - V_-$.

The most simple use for an operational amplifier is a comparator circuit, with the only component being the operational amplifier itself. Figure A.1a shows the operational amplifier, with its inverting ($-$) and non-inverting ($+$) terminals, the input voltages ($V_+$ and $V_-$), the output voltage ($V_{out}$) and the supply voltages ($V_a$ and $V_b$). In this configuration, the output voltage is a function the difference between the input voltages:

$$V_{out} = G_{\text{open}-\text{loop}}(V_+ - V_-), \tag{A.1}$$

where $G_{\text{open}-\text{loop}}$ is a constant with values near $10^6$. Despite the big values reached by this constant, $V_{out}$ saturates at values equal to the supply voltages (Fig. A.1b), therefore making the region where the output is not saturated very small. For most practical problems, the comparator circuit output can be approximately given by:

$$\begin{cases} V_{out} = V_a, \text{ if } V_+ > V_- \\ V_{out} = V_b, \text{ if } V_+ < V_- \ . \end{cases} \tag{A.2}$$

## A.2 Inverter amplifier

A more interesting usage of operational amplifiers happens when the inverting terminal receives a feedback connection from the output $V_{out}$. With this negative feedback, the input voltages $V_+$ and $V_-$ are kept close in value and $V_{out}$ becomes dependent only on the way the circuit connections are made: the constant $G_{\text{open}-\text{loop}}$ becomes unimportant.

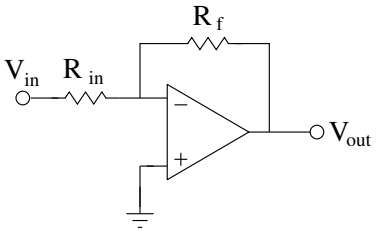


**Figure A.2** Inverter amplifier circuit. $V_{out} = -\frac{R_f}{R_{in}} V_{in}$.

Two rules determine how operational amplifiers work under negative feedback conditions: (1) the voltages at the inverting and non-inverting terminals are equal; (2) there is no current flowing to these terminals. Rule (2) implies that both inverting and non-inverting terminals have infinite impedance. Rules (1) and (2) are only valid if the output does not reach saturation.

The inverter amplifier circuit, shown in Fig. A.2, is an example of operational amplifiers under negative-feedback conditions. The output voltage $V_{out}$ can be easily calculated from the two rules. The non-inverting terminal has zero electric potential since it is grounded, therefore from rule (1) we have:

$$V_+ = 0 = V_-. \tag{A.3}$$

Since there is no current flowing to the inverting terminal, the current $I$ flowing through the resistance $R_{in}$ is the same that flows through the resistance, $R_f$, thus:

$$V_{out} = V_{in} - (R_{in} + R_f) I. \tag{A.4}$$

With Eq. (A.3), we then find that $I = V_{in}/R_{in}$. Using the value of $I$ in Eq. (A.4) gives us the final result:

$$V_{out} = -\frac{R_f}{R_{in}} V_{in}. \tag{A.5}$$

The circuit in Fig. A.2 is called inverter amplifier because the output voltage does not have the same sign as the input voltage. The amplification factor can be controlled by the resistances $R_{in}$ and $R_f$.

## A.3 Non-inverter amplifier

The circuit shown in Figure A.3 is a non-inverter amplifier. It has the same purpose of the inverter amplifier, but its output has the same sign of the input. From rule (1) we have:

$$V_{in} = V_-. \tag{A.6}$$

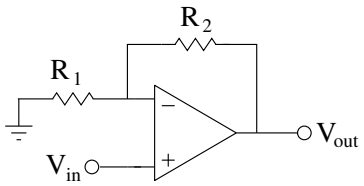


**Figure A.3** Non-inverter amplifier circuit. $V_{out} = V_{in}\left(1+\frac{R_2}{R_1}\right)$.

Since, from rule (2), there is no current flowing to the inverting terminal, the current $I$ flowing through the resistance $R_1$ must be the same flowing through the resistance $R_2$, therefore:

$$I = \frac{V_{in}}{R_1} \implies V_{out} = (R_1 + R_2)I = V_{in}\left(1+\frac{R_2}{R_1}\right). \tag{A.7}$$

## A.4 Buffer

The circuit shown in Figure A.4 is called buffer or voltage follower since its output voltage repeats the input. A buffer provides high input impedance, which prevents circuit elements that are connected to the buffer output from drawing current from elements connected to the buffer input. It can be used, for example, to connect a low impedance resistor to a real voltage source without change the voltage provided by it. The relation $V_{out} = V_{in}$ follows directly from the rules (1) and (2).

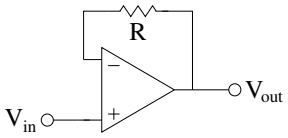


**Figure A.4** Buffer. $V_{out} = V_{in}$.

## A.5 Subtractor circuit

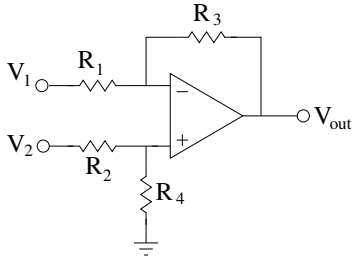


**Figure A.5** Subtractor circuit. $V_{out} = \frac{(R_1+R_3)}{R_1}\frac{R_4}{(R_2+R_4)}V_2 - \frac{R_3}{R_1}V_1$.

The circuit shown in Fig. A.5 was used to obtain spikes as the output of the excitable electronic circuit. The relation between the voltages $V_1$, $V_2$ and $V_{out}$ is obtained from rules (1) and (2). Since there is no current flowing to the inverting and non-inverting terminals of the operational amplifier, the current $I_2$ through the resistances $R_2$ and $R_4$ is given by:

$$I_2 = V_2/(R_2+R_4). \tag{A.8}$$

The non-inverter electric potential is given by:

$$V_+ = V_2 - R_2 I_2 = R_4 I_2 = \frac{R_4}{R_2+R_4} V_2 = V_-. \tag{A.9}$$

where we used rule (1) to obtain the last equality. The current $I_1$ through the resistances $R_1$ and $R_3$ is obtained from the result of Eq. (A.9):

$$I_1 = \frac{V_1}{R_1} - \frac{R_4}{R_2+R_4}\frac{V_2}{R_1}. \tag{A.10}$$

Since $V_{out} = V_1 - (R_1+R_3)I_1$, replacing the value of $I_1$ in Eq. (A.10) finally leads to:

$$V_{out} = \frac{(R_1+R_3)}{R_1}\frac{R_4}{(R_2+R_4)} V_2 - \frac{R_3}{R_1} V_1. \tag{A.11}$$

Therefore, the output voltage of the subtractor circuit is a weighted subtraction of the input voltages $V_2$ and $V_1$. The weights can be controlled by adjusting the resistance values. In particular, if $R_1 = R_2 = R_3 = R_4$ the result is a simple subtraction: $V_{out} = V_2 - V_1$.

## A.6 Summator circuit

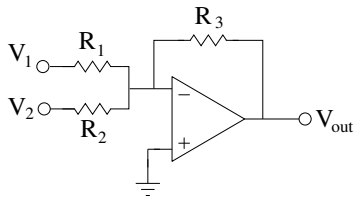


**Figure A.6** Summator circuit. $V_{out} = -\left(\frac{R_3}{R_1}V_1 + \frac{R_3}{R_2}V_2\right)$.

The circuit shown in Fig. A.6 was used to obtain input stimulus for the excitable electronic circuit, adding the noisy input, the DC voltage and synaptic inputs and to add together their outputs when measuring network activity. The relation between the voltages $V_{out}$, $V_1$ and $V_2$ follows from the observation that $I_1 = V_1/R_1$, $I_2 = V_2/R_2$, and $V_{out} = -(I_1+I_2)R_3$:

$$V_{out} = -\left(\frac{R_3}{R_1}V_1 + \frac{R_3}{R_2}V_2\right). \tag{A.12}$$

The output voltage of the summator circuit is a weighted sum of the voltages $V_2$ e $V_1$ with reverse sign. If $R_1 = R_2 = R_3$, then $V_{out} = -(V_1+V_2)$.

APPENDIX B

# Electronic components and equipment used

We used a symmetrical voltage source made at our Physics Department to power all the circuits used in this work. Table B.1 shows the values of the electronic components used in the excitable electronic circuit (Fig. 1.16).

| Component | Value | Additional information |
|---|---|---|
| $R_1$ | 1 kΩ | precision 5%; SMD |
| $R_2$ | 10 kΩ | precision 5%; SMD |
| $R_3$ | 1 MΩ | precision 5%; SMD |
| $R_4$ | 10 kΩ | precision 5%; SMD |
| $R_5$ | 10 kΩ | precision 5%; SMD |
| $C$ | 1 nF or 50 pF | ceramic; precision 5%; SMD |
| $V_a$ | 12 V | – |
| $V_b$ | −12 V | – |

**Table B.1** Values of the electronic components used in the excitable electronic circuit.

Note that the approximation $I_3 \simeq 0$ assumed in page 38 is reasonable since:

$$\frac{R_4}{R_3} = \frac{R_5}{R_3} = 0.01. \tag{B.1}$$

| Block | Component | Value | Additional information |
|---|---|---|---|
| Summator | $R_1$ | 10 kΩ | precision 5%; SMD |
| | $R_2$ | 10 kΩ | precision 5%; SMD |
| | $R_3$ | 10 kΩ | precision 5%; SMD |
| Subtractor | $R_1$ | 1.5 kΩ | precision 5%; SMD |
| | $R_2$ | 100 Ω | precision 5%; SMD |
| | $R_3$ | 1 kΩ | precision 5%; SMD |
| | $R_4$ | 1 kΩ | precision 5%; SMD |
| Buffer | $R$ | 1 kΩ | precision 5%; SMD |
| Supply votages | $V_a$ | 12 V | – |
| | $V_b$ | −12 V | – |

**Table B.2** Values of the electronic components used in the auxiliary circuits. The resistances indices are the same used in the Appendix A.

The symmetrical voltage source also provided the DC voltage $V_{DC}$ applied to the excitable electronic circuits. The data was measured with an Agilent Technologies oscilloscope model DSO-X 2002A.

In the block diagram of Fig. 1.22b we employed circuits that require operational amplifiers (the excitable electronic circuit, the subtractor circuit, a buffer and the summator circuit. The operational amplifiers are part of integrated SMD circuits TL072 or TL074 with two or four of them in each, respectively. The supply voltages are shared by operational amplifiers in the same integrated circuit. The electronic components used in each of these circuits are shown in Table B.2.

The diode used in the electronic synapses to rectify the input $V_{pre}$ of the electronic excitable circuits was SMD diode model 1N4148.

The summator circuit used to measure network activity (as described in Chapter 5) used the same components except that all of them are regular component (not SMD, including the operational amplifier) and the resistance $R_3 = 0.5$ k$\Omega$. The diodes mounted at the output of each excitable electronic circuit on the protoboards were 1N4148 standard diodes.

This volume has been typeset in LaTeX with the UFPEThesis class (www.cin.ufpe.br/~paguso/ufpethesis).